Multifunctional Nanoparticles for Radiotherapy Enhancement and Targeted Phototherapies

by

Mine Demir

A Dissertation Submitted to the
Graduate School of Sciences and Engineering
in Partial Fulfillment of the Requirements for
the Degree of

Doctor of Philosophy

in

Chemistry

March 3, 2025

Multifunctional Nanoparticles for Radiotherapy Enhancement and Targeted Phototherapies

Koç University

Graduate School of Sciences and Engineering

This is to certify that I have examined this copy of a Ph.D. thesis by

Mine Demir

and have found that it is complete and satisfactory in all respects,
and that any and all revisions required by the final
examining committee has been made.

Committee Members:

Prof. Havva Yağcı Acar

Assoc. Prof. Uğur Ünal

Prof. Mehmet Burçin Ünlü

Prof. Uğur Selek

Assist. Prof. Kübra Onbaşlı

March 3, 2025

This thesis is dedicated to my wonderful family.

ABSTRACT

Multifunctional Nanoparticles for Radiotherapy Enhancement and Targeted Phototherapies

Mine Demir
Doctor of Philosophy in Chemistry
March 3, 2025

In 2024, the National Institutes of Health reported 2 million new cancer cases and 600,000 cancer-related deaths in the United States. Cancer remains a complex disease and a significant public health challenge. Conventional cancer treatments such as surgery, chemotherapy, and radiotherapy are successful. However, localization of the treatment, tumor specificity, adverse side effects of the treatments, and cancer metastases are still challenging issues. Novel treatment strategies that overcome these limitations are the focus of researchers, which is to increase the survival rate and improve patients' comfort.

Radiotherapy (RT), a commonly used cancer treatment, uses ionizing radiation to kill or prevent the growth of malignant cells. It is a relatively local treatment compared to chemotherapy but is usually combined with other treatment methods for more efficient results. Some concerns associated with this treatment are dose heterogeneity, side effects on healthy tissues, and the radio-resistance of specific cancer cells. Radiosensitizers allowing local radiation enhancement at low doses of ionizing radiation and more homogeneous dose distribution within the tumor are highly popular and the subject of continuous research.

Light-based therapies, such as photothermal and photodynamic therapies, may be combined with RT to enhance the treatment efficacy. These techniques provide a local, turn-on mechanism for cancer treatment. Photothermal therapy (PTT) is based on local hyperthermia caused by light irradiation of a photosensitizer (PS). Photodynamic therapy (PDT) relies on activating a photosensitizer by light and generating reactive oxygen species. Limitations in these therapies include solubility and bioavailability of the photosensitizer, day-light sensitivity of the patient, and activation of PSs mostly in blue, exerting a significant limitation in penetration depth. Protoporphyrin IX (PpIX), a common PDT photosensitizer typically irradiated with blue or red light, has been recently

reported to be activated with X-ray, and this process is called radio dynamic therapy (RDT).

This thesis explores the theranostic applications of gold-gold sulfide nanoparticles (GGS) with strong absorbance in the near-infrared, contrast ability in photoacoustic imaging (PAI), and potential for radiosensitization for low-dose RT, and combination of low-dose RT with phototherapies to improve therapeutic outcomes.

In this thesis work, a combination of RDT with low-dose RT, bypassing high radiation dose requirements and light penetration limitations, was investigated via 5-aminolevulinic acid (ALA) loaded branched polyethyleneimine-coated GGS (bPEI-GGS) nanoparticles. ALA is a pro-drug converted to PpIX in living cells, more so in cancer cells. In vitro activity assessments were performed on PC3 prostate cancer and MDA-MB-231 breast cancer cell lines at low X-ray doses between 0.5, 1, 2, and 4 Gy. Cell viability dropped below 20% after 0.5 Gy RDT treatment with a low dose of GGS (Au concentration (μg/ml)/ALA concentration (mM): 25/0.22) for both cell lines. ALA-bPEI-GGS nanoparticles represent a promising approach to enhancing RDT effectiveness, especially for deep-seated and radioresistant tumors, with a level of selectivity towards cells overexpressing PEPT1/PEPT2.

In the second part of the thesis, tumor-specific delivery of multifunctional nanoparticles providing a combination of photothermal therapy (PTT) and low-dose RT for improved therapeutic outcomes under mild conditions has been demonstrated using theranostic GGS nanoparticles with no further therapeutic agents. Multifunctional 3-mercaptopropionic acid-coated GGS (3MPA-GGS) were tagged with folic acid (FA-3MPA-GGS) to selectively target folate receptor-positive (FR+) cancer cells, enhancing therapeutic specificity and efficacy. FA-3MPA-GGS demonstrated strong NIR absorption, high-temperature increase, photothermal stability, and efficient light-to-heat conversion in the solution when irradiated with 808 nm, 215 mW laser. In vitro experiments performed with FR+ (HeLa and MDA-MB-231) and FR- (A549) cells indicated enhanced uptake, increased ROS generation, and more significant cytotoxicity in FR+ cells. Combining mild PTT with low-dose RT via FA-3MPA-GGS led to synergistic effects, lowering the treatment dose and enabling image-guided precision. Near-complete death of HeLa and MDA-MB-231 were obtained with PTT/RT at 200 μg Au/mL concentration, with 10 min 795 nm (1 W) laser irradiation followed w 0.5 Gy X-ray irradiation.

This thesis's third part focuses on phototherapies without the use of ionizing radiation: the combination of nanoparticle-driven PTT and ALA-PDT. A novel dual-mode phototherapy approach for the treatment of prostate cancer using ALA-loaded superparamagnetic iron oxide nanoparticles (ALA-PAA-SPIONs) was demonstrated. Utilizing the upregulation of PEPT1/PEPT2, effective in selective transport of ALA, in prostate cancer cells presents a valuable target for enhancing delivery and specificity in treatment. In vitro experiments on LNCaP, PC3, and DU145 cell lines demonstrated selective cellular uptake of NPs in PEPT1/PEPT2 overexpressed LNCaP and PC3 cells. Formation of reactive oxygen species (ROS) and induction of apoptosis upon laser irradiation (640 nm, 700 mW, 10 minutes) lead to significant loss of cell viability (<10%), specifically in these two cell lines. The results showed the potential of ALA-PAA-SPION as a promising phototherapy agent for prostate cancer treatment, offering improved specificity and minimized systemic effects.

ÖZETÇE

Radyoterapi Güçlendirilmesi ve Hedeflenmiş Fototerapiler için Multifonksiyonel Nanopartiküller

Mine Demir
Kimya, Doktora
3 Mart 2025

2024 yılında, Ulusal Sağlık Enstitüleri (NIH) Amerika Birleşik Devletleri'nde 2 milyon yeni kanser vakası ve 600.000 kanserle ilişkili ölüm bildirdi. Kanser, karmaşık bir hastalık olmaya devam etmekte ve önemli bir halk sağlığı sorunu oluşturmaktadır. Cerrahi, kemoterapi ve radyoterapi gibi geleneksel kanser tedavileri başarılıdır. Ancak, tedavinin lokalizasyonu, tümör spesifikliği, tedavilerin yan etkileri ve kanser metastazları hâlâ önemli zorluklar arasında yer almaktadır. Yeni tedavi stratejileri, bu zorlukların üstesinden gelerek sağkalım oranını artırmayı ve hastaların konforunu sağlamayı amaçlamaktadır.

Radyoterapi (RT), yaygın olarak kullanılan bir kanser tedavisi olup, iyonize radyasyon kullanarak malign hücreleri öldürmeyi veya büyümelerini durdurmayı hedefler. Kemoterapiye kıyasla daha lokal bir tedavi yöntemi olup, tek başına uygulanabileceği gibi diğer yöntemlerle kombine edilerek daha etkili sonuçlar elde edilebilir. Ancak, bu tedaviyle ilişkili bazı endişeler arasında doz heterojenliği, sağlıklı dokular üzerindeki yan etkiler ve belirli kanser hücrelerinin radyorezistansı yer almaktadır. Radyosensitizörler, lokal olarak radyasyon etkinliğini artırmaları ve dozun tümöre daha homojen bir şekilde dağıtılmasını sağlamaları nedeniyle dikkat çekmektedir.

Işık bazlı terapiler, örneğin fototermal ve fotodinamik tedaviler, radyoterapi ile kombine edilerek tedavi etkinliği artırılabilir. Bu teknikler, kanser tedavisi için lokal ve açılabilir (turn-on) bir mekanizma sunar. Fototermal terapi (PTT), bir fotosensitizörün ışıkla uyarılması sonucu oluşan lokal hipertermiye dayanır. Fotodinamik terapi (PDT) ise, fotosensitizörün ışıkla uyarılması ve moleküler oksijen ile etkileşimi sonucunda reaktif oksijen türlerinin (ROS) üretilmesine dayanır. Penetrasyon derinliğini artırmak amacıyla, etkinleştirilebilir fotosensitizörlerle birlikte yakın kızılötesi (NIR) ışık tercih edilir.

Altın nanoparçacıklar (GNP'ler), inert yapıları, yüksek X-ışını absorpsiyon katsayıları, yüzey fonksiyonelleştirme kolaylığı, ayarlanabilir optik özellikleri ve yüksek ışık-ısı dönüşüm verimlilikleri nedeniyle kanser tanı ve tedavisinde önemli avantajlar

sunar. Altın-altın sülfür nanoparçacıkları (GGS), karakteristik yüzey plazmon rezonansına ek olarak NIR absorbansına sahip yeni nesil GNP'lerdir. Son yıllarda, GGS'nin fotoakustik görüntüleme (PAI) için etkili bir kontrast ajanı olduğu gösterilmiş ve görüntü rehberliğinde tedavi için potansiyeli ortaya konmuştur.

Bu tez, GGS'nin tanı ve tedavi amaçlı uygulamalarını incelemekte olup, özellikle radyoterapiyi geliştirmek için kombine yaklaşımlara odaklanmaktadır. Tezin ilk bölümünde, GGS'nin radyosensitizör olarak kullanımı ve 5-aminolevulinik asit (ALA) ön ilacının taşıyıcısı olarak rolü vurgulanmaktadır. ALA, yaygın olarak fotodinamik tedavide kullanılan protoporfirin IX'in (PpIX) öncüsüdür. Yüksek suda çözünürlüğü nedeniyle vücuttan hızlıca atılır. PpIX genellikle mavi ve kırmızı ışıkla uyarılmakta olup, bu durum penetrasyon derinliği açısından zorluk yaratmaktadır. Son çalışmalar, PpIX'in X-ışınları ile de aktive edilebileceğini göstermiş ve bu süreç "radyodinamik terapi (RDT)" olarak adlandırılmıştır. Bu çalışmada, dallanmış polietilenimin (bPEI) kapladığı GGS'ler (bPEI-GGS) ALA ile elektrostatik olarak yüklenmiş (ALA-bPEI-GGS) ve bu sayede radyosensitizasyon sağlanarak X-ışını dozunun azaltılması, ALA'nın tümörlere daha iyi taşınması ve PpIX'in mavi-kırmızı ışık penetrasyon sınırını aşarak X-ışınlarıyla aktive edilmesi hedeflenmiştir. İn vitro deneyler, PC3 prostat kanseri ve MDA-MB-231 meme kanseri hücre hatlarında gerçekleştirilmiştir. bPEI-GGS ve ALA-bPEI-GGS, 24 saat inkübasyon sonrası 0.5, 1, 2 ve 4 Gy düşük X-ışını dozlarında test edilmiştir. 0.5 Gy RDT tedavisinden sonra, düşük doz GGS (Au konsantrasyonu (μg/ml)/ALA konsantrasyonu (mM): 25/0.22) ile her iki hücre hattında da hücre canlılığı %20'nin altına düşmüştür. Tedavi, PC3 hücrelerinde apoptoz belirteçlerini, DNA hasarını ve otofajiyi önemli ölçüde artırırken, MDA-MB-231 hücrelerinde minimal değişiklikler gözlenmiştir. ALA-bPEI-GGS nanoparçacıkları, özellikle derin yerleşimli ve radyorezistan tümörler için RDT etkinliğini artırmak adına umut vadeden bir yaklaşım olarak öne çıkmaktadır.

Tezin ikinci bölümünde, radyoterapinin etkisini artırmaya yönelik başka bir yaklaşım sunulmaktadır. 3-merkapto propiyonik asit ile kaplanmış GGS (3MPA-GGS) nanoparçacıkları, PAI, PTT ve RT için tanı ve tedavi amaçlı bir araç olarak kullanılmıştır. Multifonksiyonel 3MPA-GGS'ler, folik asit (FA) ile fonksiyonelleştirilerek (FA-3MPA-GGS), folat reseptörü pozitif (FR+) kanser hücrelerini seçici olarak hedef almış ve tedavi spesifikliği ile etkinliğini artırmıştır. FA-3MPA-GGS, güçlü NIR absorbansı, yüksek sıcaklık artışı, fototermal stabilite ve 808 nm, 215 mW lazer ışını altında yüksek ışık-ısı dönüşüm verimliliği sergilemiştir. İn vitro deneyler, FR+ (HeLa ve MDA-MB-231) ve FR- (A549) hücreleri üzerinde gerçekleştirilmiştir. Sonuçlar, FR+ hücrelerde daha

yüksek nanoparçacık alımı, artan ROS üretimi ve daha belirgin sitotoksisite göstermiştir. FA-3MPA-GGS ile kombine edilen PTT ve RT, sinerjik etkiler göstererek tedavi dozunu azaltmış ve görüntü rehberliğinde hassasiyeti artırmıştır. HeLa ve MDA-MB-231 hücrelerinin canlılığı, 200 μg Au/mL konsantrasyonunda 6 saat inkübasyon sonrası, 795 nm (1 W) lazer ışını ile 10 dakika ışınlanarak ve ardından 0.5 Gy X-ışını uygulanarak %10'un altına düşmüştür.

Tezin üçüncü bölümü, yalnızca fototerapilere odaklanmaktadır. Bu çalışmada, fototermal ve fotodinamik terapileri birleştiren yeni bir çift modlu fototerapi yaklaşımı ile prostat kanseri tedavisi sunulmaktadır. 5-ALA yüklü süperparamanyetik demir oksit nanoparçacıkları (ALA-PAA-SPIONs) kullanılarak PTT ve PDT entegrasyonu sağlanmıştır. PEPT1 ve PEPT2, ALA'yı taşıyabilmekte ve bu sayede seçicilik sağlayabilmektedir. Prostat kanseri hücrelerinde PEPT1/PEPT2'nin aşırı eksprese edilmesi, hedefleme ve tedavi spesifikliğini artırabilecek değerli bir strateji sunmaktadır. Karakterizasyon, ALA'nın SPION'lara elektrostatik olarak başarılı bir şekilde yüklendiğini doğrulamıştır. LNCaP, PC3 ve DU145 hücre hatlarında yapılan in vitro deneyler, PEPT1/PEPT2 aşırı eksprese eden LNCaP ve PC3 hücrelerinde seçici alımı göstermiştir. 640 nm, 700 mW, 10 dakika lazer ışını uygulandıktan sonra ROS üretimi ve apoptoz indüksiyonu, LNCaP ve PC3 hücrelerinde hücre canlılığını %10'un altına düşürmüştür. Sonuçlar, ALA-PAA-SPIONs'un prostat kanseri tedavisi için umut vadeden bir fototerapi ajanı olduğunu ve spesifikliği artırarak sistemik etkileri minimize edebileceğini göstermektedir.

ACKNOWLEDGEMENTS

First, I would like to express my gratitude to my dear supervisor, Prof. Havva Funda Yağcı Acar, for her endless support during my Ph.D. journey. I feel so lucky and proud to be her student. She guided me with her endless knowledge and put her complete trust in me at every step of my Ph.D. She trained me academically and prepared me for life and all the problems I would encounter. She will always have a special place in my heart.

I want to thank my thesis committee members and collaborators, Prof. Burçin Ünlü, Prof. Uğur Selek, Assoc. Prof. Uğur Ünal and Asst. Prof. Kübra Onbaşlı. Their knowledge of different scientific fields had a significant contribution to our projects. I would like to emphasize my gratitude for their time and consideration of this Ph.D. thesis.

I would like to thank all our collaborators individually for their valuable contributions to this thesis work and my professional development. Prof. Burçin Ünlü and Dr. Natali Çizmeciyan from Özyeğin University provided the funding throughout my PhD and experimentally performed all the photoacoustic imaging part of the thesis work. Prof. Uğur Selek and Dr. Duygu Sezen from Koç University Hospital contributed to the radiotherapy part of this thesis with their valuable discussions, know-how, and expertise. Prof. Devrim Gözüaçık and Dr. Yunus Akkoç contributed with their expert opinion and extensive experience in cell death mechanisms. Assoc. Prof. Uğur Ünal had full support for me and was always helpful with the TEM imaging of the nanoparticles. Asst. Prof. Kübra Onbaşlı had endless guidance throughout my Ph.D., and we completed many projects together. Prof. Alphan Sennaroğlu and Asst. Prof. Yağız Morova helped with all the laser experiments and guided me with the experimental designs.

I would like to thank my Funtech family: Dr. Eda Çelikbaş, Ahmet Ferid Fırat, Ece Çakır, İrem Acar, Ali Ekber Avşar, Tuana Aksu, Tuana Karaarslan, Ahmed Seyitoğlu, Shiva Soori, Ali Arı, Selin Alptekin, Dilara Sipahioğlu. We built a beautiful lab environment filled with love, scientific knowledge, and friendship. A special thanks go to my gold subgroup: I would not have completed my Ph.D. work without my lovely friend, little brother, and student Ali Ekber Avşar. He did great work, contributed to all projects, and motivated me in every step. İrem Acar, my 7/24 joy, had full support for me academically and emotionally, and she will be carrying out our projects further.

I would like to acknowledge the team at Koç University Surface Science and Technology Center (KUYTAM), especially Dr. Barış Yağcı and Assoc. Prof. Gülsu Şimşek Franci for their constant help in our measurements. I thank Koç University

Animal Research Laboratory (KUARF), Nilhan Coşkun, and Mustafa Demir for their help with the X-ray instrument and experimental design.

Very special thanks to the people who were always with me…

I would like to express my gratitude to my wonderful family, especially my parents, Şükran and Murat Demir, and my brother, Emre Demir, for their full support, love, and trust in me. This Ph.D. would not have been completed without them. They are my biggest motivation in this life.

I would like to sincerely thank my beloved fiancée, Turab Ali Khan, for his constant support through my best and worst moments. He has always cheered me up and motivated me to pursue my dreams. His thoughtful advice and academic insights have guided me in making the right decisions. I am deeply grateful to him and hold endless love for him.

Finally, I would like to thank The Scientific and Technological Research Council of Türkiye (TUBİTAK). These projects are partially funded by Project No: 119F319 (PI: Prof. Burçin Ünlü) and partially with Project No: 22AG016.

Table of Contents

List of Tables

List of figures

ABBREVIATIONS

5-ALA	5-Aminolevulinic acid
3-MPA	3-mercaptopropionic
A549	Adenocarcinomic human alveolar basal epithelial cells
bPEI	Branched poly (ethylene imine)
BSA	Bovine Serum Albumin
Da	Dalton
ΔT	Temperature change
DLS	Dynamic Light Scattering
DMEM	Dulbecco's modified Eagles medium
DMSO	Dimethyl sulfoxide
EDC	N-(3-dimethylaminopropyl)-n′-ethylcarbodiimide hydrochloride
EDL	Electrostatic double layer
EtOH	Ethanol
FA	Folic Acid
FBS	Fetal Bovine Serum
FTIR	Fourier Transform Infrared Spectroscopy
GNP	Gold Nanoparticles
GNR	Gold nanorods
GGS	Gold-gold sulfide
$HAuCl_4$	Auric acid
HeLa	Human Cervical Carcinoma
IC50	Half maximal inhibitory concentration
ITC	Isothermal Titration Calorimetry
L929	Mouse fibroblast
LDH	Lactate dehydrogenase
MDA-MB-231	Human breast carcinoma
MW	Molecular weight
MTT	Thiazolyl blue tetrazolium bromide
$NaBH_4$	Sodium borohydride
Na_2S	Sodium sulfide
$Na_2S_2O_3$	Sodium thiosulfate

NHS	N-hydroxysuccinimide
NP	Nanoparticle
NIR	Near-infrared
PAI	Photoacoustic imaging
PBS	Phosphate buffered saline
PC3	prostatic adenocarcinoma
PDI	Polydispersity index
PDT	Photodynamic Therapy
PEG	Polyethylene glycol
Pen/strep	Penicillin/streptomycin
PpIX	Protoporphyrin IX
PS	Photosensitizer
PTT	Photothermal therapy
QD	Quantum dot
RDT	Radiodynamic therapy
RT	Radiotherapy
ROS	Reactive oxygen species
SD	Standard deviation
-SH	Thiol
SPR	Surface Plasmon Resonance
TEM	Transmission electron spectroscopy
TUBITAK	Scientific and Technological Research Council of Türkiye
TGA	Thermal gravimetric analysis
UV	Ultraviolet
vdW	Van der Waals
Vis	Visible
XPS	X-ray photoelectron spectroscopy
XRD	X-ray diffraction

Chapter 1: Introduction

*1.1 **Nanoparticles (NPs)***

Nanotechnology is the platform that brings solutions to many fields, including medicine, energy, safety, environment, food, and textile. Nanoparticles (NPs), the leading role of nanotechnology, are defined as particles smaller than 100 nm in at least one dimension [3].

1.1.1 Properties and classification of NPs

NPs display unique properties at the nanoscale compared to their bulk materials. Due to the high surface-to-volume ratio and quantum effects, size-dependent properties lead to significant changes in physical, optical, magnetic, electrical, chemical, and mechanical properties. Some of the examples of distinct properties of NPs are Brownian motion, melting point depression, catalytic activity, quantum confinement in semiconductor NPs, or surface plasmon resonance (SPR) in some metal NPs [4].

Nanoparticles (NPs) can be classified based on their properties and characteristics. One approach is categorization by chemical composition: (a) organic NPs, including micelles, dendrimers, polymeric nanoparticles, and liposomes; (b) inorganic NPs, such as quantum dots, and metallic, ceramic, or zeolite nanoparticles; and (c) carbon-based NPs, including graphene quantum dots, carbon nanodots, and polymer nanodots. Another classification method considers the number of nanoscale dimensions: (a) zero-dimensional (0D) NPs, such as nanoparticles and quantum dots; (b) one-dimensional (1D) structures, including nanorods and nanotubes; (c) two-dimensional (2D) materials, such as graphene and black phosphorus; and (d) three-dimensional (3D) structures, like nanoflowers and nanostars [5]. Figure 1.1 shows the schematic representation of the classification, properties, and applications of NPs.

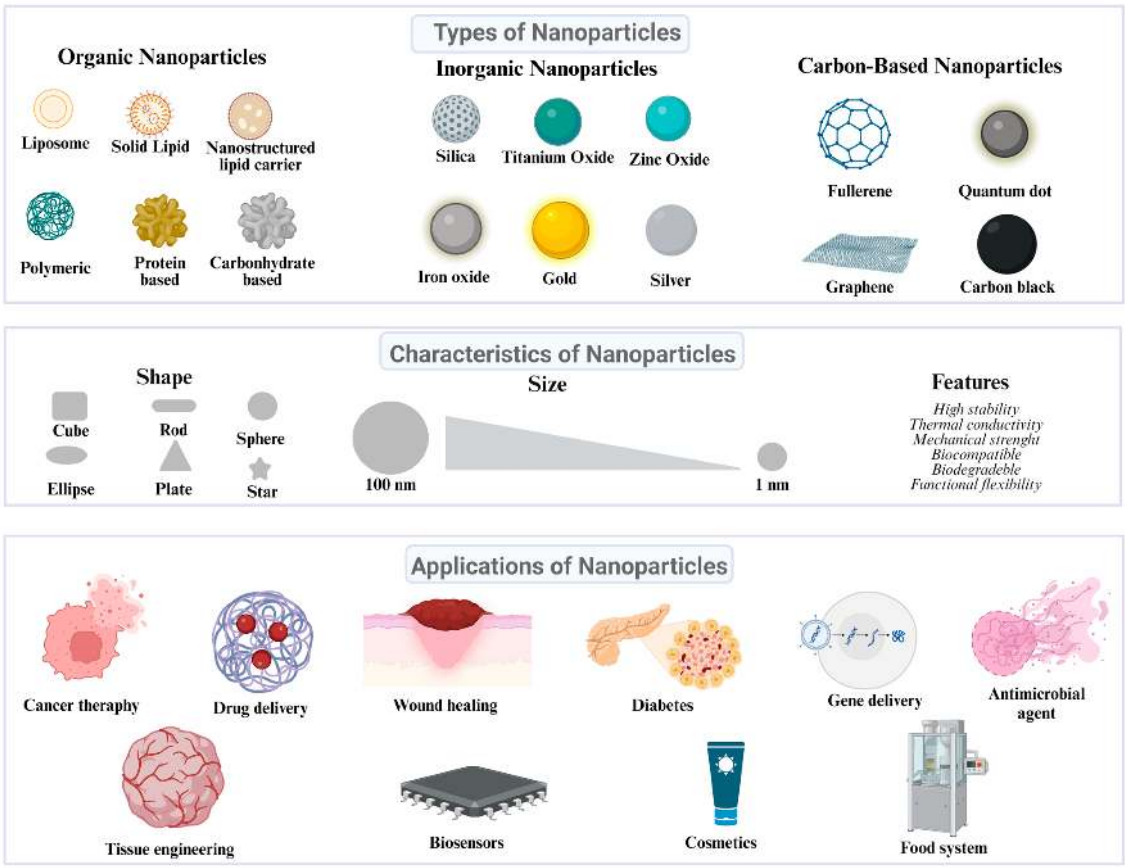

Figure 1.1 Schematic representation of classification, properties, and applications of NPs [6].

1.1.2 Synthesis methods of NPs

The main approaches for the synthesis of NPs include top-down and bottom-up synthesis. The top-down approaches are based on decreasing the size of a bulk material with ball-milling, thermal evaporation, laser ablation, and sputtering [7]. These methods offer large-scale production, simplicity, and no solvent usage. However, it can be destructive for the crystal structure, making it hard to control the size and shape, and there is a risk of contamination. Bottom-up synthesis aims for NPs to build up from the atomic level to the nanoscale. Bottom-up approaches are atomic condensation, chemical vapor deposition, hydrothermal, sol-gel, and co-precipitation. These methods may require solvent and be more expensive. However, keeping the atomic building blocks in order allows precise control of size, shape, and surface functionalization [8].

One of the most precise controls of colloidal NP synthesis can be ensured by the chemical reduction method. In this method, the metal precursor is dissolved by a solvent and reduced by a reducing agent such as borohydrides, amino boranes, hydrides, hydrogen peroxide, sulfites, hydrogen, hydroxylamine, and hydrazine [9]. The particle

formation process can be explained by the LaMer model, as in Figure 1.2. The formation of nanoparticles begins with an increase in reduced monomer concentration, leading to the creation of small, unstable clusters. As the monomer concentration continues to rise, stable clusters form through nucleation, reducing the monomer concentration. Once nucleation ceases, the clusters grow by consuming the remaining monomers until saturation is reached. Initially, growth is kinetically controlled and proportional to particle surface area. If growth persists after precursor reduction, it becomes thermodynamically controlled, with larger particles forming at the expense of smaller ones through Ostwald ripening, influenced by the metal, reaction medium, and other conditions [10]. Here, the synthesis allows surface passivation, a key factor in providing the colloidal stability of the NPs.

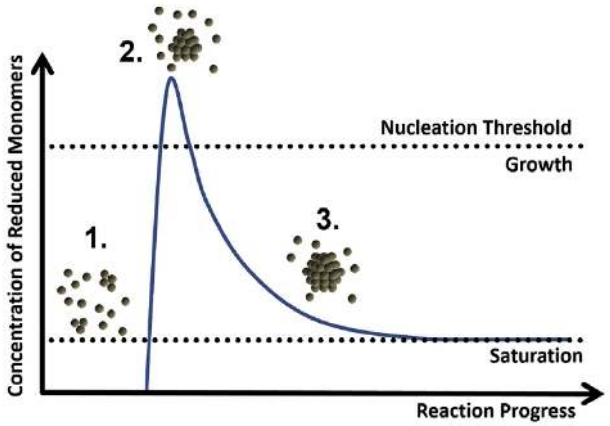

Figure 1.2 Nanoparticle formation process according to the LaMer model [10].

Stabilization of NPs is mainly provided by the balance of attractive and repulsive forces, which are steric or electrostatic interactions. The colloidal stability of NPs in aqueous suspension is governed by the interplay of intermolecular and surface forces, including van der Waals (vdW) forces, the electrostatic double layer (EDL), and structural forces [11, 12]. NPs have an inherent surface charge due to surface ions or functional small molecules (e.g. citrates, mercaptopropionic acids), leading to the formation of an EDL. The EDL consists of the Stern layer (adsorbed oppositely charged ions) and the diffuse layer (surrounding counterions). When two similarly charged particles come close, their EDLs overlap, creating a repulsive force that prevents aggregation. Zeta potential, measured at the shear plane, characterizes the charge of the Stern layer of bound ions and a diffuse layer of counterions.

The stability of colloidal nanoparticles can also depend on macromolecule adsorption, such as synthetic polymers or biopolymers (e.g., polyethylene glycol, oleic acid), which can provide steric stabilization. This stabilization prevents particle aggregation through osmotic pressure and elastic recoil effects, influenced by the density and uniformity of the polymer coating [13]. Charged macromolecules (e.g. polyacrylic acid, polyethyleneimine) can enhance stability via electrosteric repulsion. However, uneven polymer coatings or bridging effects, where a single polymer chain links multiple particles, can cause aggregation, particularly with high-molecular-weight polymers at insufficient concentrations [11].

*1.2 **Gold Nanoparticles (GNPs)***

Gold (Au) is an element that offers unique properties in the nanoscale. In the fourth century, gold flakes were used in glassmaking to create the Lycurgus Cup, which shifts between green and red colors depending on light exposure [14]. They were later utilized in stained glass to craft vibrant church windows, notably the ruby red color [15]. These examples represent some of the earliest uses of gold nanomaterials. From the earliest applications till today, gold nanoparticles (GNPs) have continued to express their unique optical and electronic properties across a wide range of fields.

1.2.1 Characteristic properties of GNPs

The vivid red color of GNPs arises from the absorption and scattering of light. The size, shape, dielectric constant, and interparticle spacing strongly influence this unique absorbance property of GNPs. When light interacts with a gold nanoparticle, its free electrons oscillate collectively in response to the electromagnetic field, a phenomenon known as localized surface plasmon resonance (LSPR). This occurs in nanomaterials with a high density of free electrons, such as metals and doped semiconductors [16, 17]. LSPR involves two key light-matter interactions: scattering (light re-radiation) and absorption (conversion of light to heat), which together cause light attenuation (extinction = scattering + absorption). Additionally, LSPR generates strong surface electric fields, enhancing optical signals like fluorescence or Raman scattering from nearby molecules.

When light interacts with larger GNPs, their free electrons oscillate less coherently, resulting in a redshift and broadening of the optical response [18]. The high distance between surfaces in these particles reduces the energy required for electrons to shift from

their equilibrium positions. Larger particles also support higher-order plasma oscillation modes, such as quadrupolar and multipolar resonances at lower energies (longer wavelengths), and exhibit increased light scattering. Similarly, agglomeration can lead to redshift in the LSPR peak as they will act as a larger nanoparticle. The symmetry and shape of nanostructures also influence their polarization modes and plasmonic properties. Increased symmetry allows more polarization modes, resulting in additional plasmonic peaks. Sharp corners cause redshifts due to electron accumulation and reduced restoring forces. Shape anisotropy, such as an increasing aspect ratio, leads to two distinct dipole oscillations: a longitudinal mode, which is stronger and occurs at longer wavelengths, and a transverse mode, which is weaker and appears in the visible region, as the single mode of spherical particles (Figure 1.3). This property is the reason for the diversity in the color of GNPs depending on their size and shape.

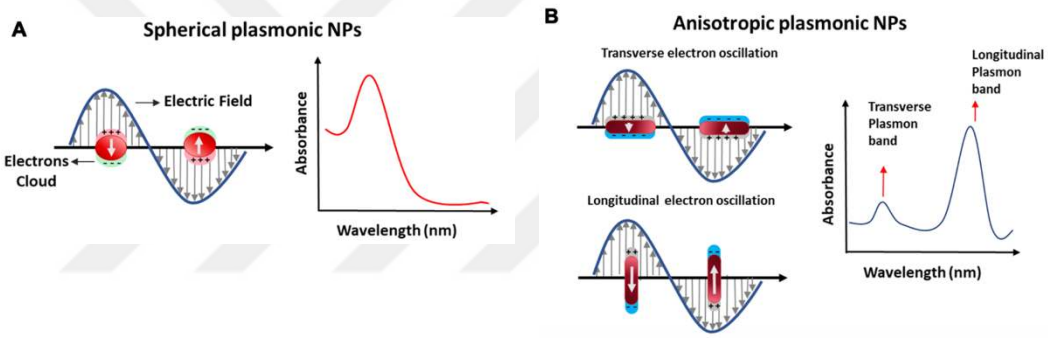

Figure 1.3 Schematic representation of SPR band in A) spherical GNPs and B) gold nanorods (GNR) [1]

Other than their unique optical properties, gold nanoparticles (GNPs) also possess properties that differentiate them from other nanoparticles. The inertness of gold nature of not allowing oxidation and corrosion makes GNPs especially well-suited for biomedical uses [19]. They are also highly amenable to surface functionalization due to the strong affinity between gold and thiol or disulfide groups. This allows for the binding of various molecules, such as antibodies, peptides, and folate, enabling their use in applications like sensing, targeting, and drug delivery [20]. The gold content in a nanoparticle solution can be quantified using instruments such as ICP-MS, ICP-OES, and optical absorption spectroscopy [21, 22]. Moreover, gold isotopes can be integrated into nanostructures for radioactivity for advanced biomedical applications [23].

1.2.2 Biomedical applications of GNPs

In nanotechnology-based research, GNPs have a significant place due to their unique properties. Ease of surface functionalization, precise size and shape control, and tunable optical properties of GNPs make them useful tools, especially for nanomedicine. Figure 1.4 shows the diversity of the biomedical applications of GNPs. The optical properties of GNPs are widely utilized in sensing applications for the detection of metal ions, molecules, nucleotides, and DNA [24]. GNP-based sensors can operate through colorimetric, fluorometric, electrical, LSPR, or surface-enhanced Raman scattering (SERS) mechanisms. Notably, the performance of these sensors is highly influenced by surface modifications and particle aggregation.

Anisotropic GNPs having surface plasmon absorption in the visible and NIR regions are widely used in medical diagnostics and therapeutic applications. The NIR region is advantageous for biomedical purposes due to its deeper tissue penetration compared to UV and visible light. Furthermore, in this range, tissues exhibit minimal autofluorescence and reduced absorbance of biological components, such as water, lipids, proteins, and hemoglobin [25]. This "NIR biological window," between 700–1100 nm, allows light to penetrate several centimeters into tissue. NIR-absorbing GNPs become relevant for PTT, a process wherein light absorption is transduced into heat to create localized heat [26]. Temperature increase helps kill biomaterials, leading to cell apoptosis [27]. Target molecules may be conjugated to agents of PTT and used as imaging agents to enhance localized heat.

The ease of surface modification of GNPs also enables their use as carriers for drugs, photosensitizers, and DNA [28]. Functional coatings and the ability to modify GNP surfaces with targeting molecules enhance their delivery efficiency. Photothermal efficiency allows drug-loaded GNPs to release their cargo in a controlled manner upon light irradiation. In photodynamic therapy (PDT), GNPs loaded with photosensitizers facilitate cell death through reactive oxygen species generation when exposed to light at the photosensitizer's absorption peak [29]. Combining PDT with GNP-mediated PTT enhances therapeutic efficacy, as the heat generated by GNPs complements the reactive oxygen species-induced cell destruction.

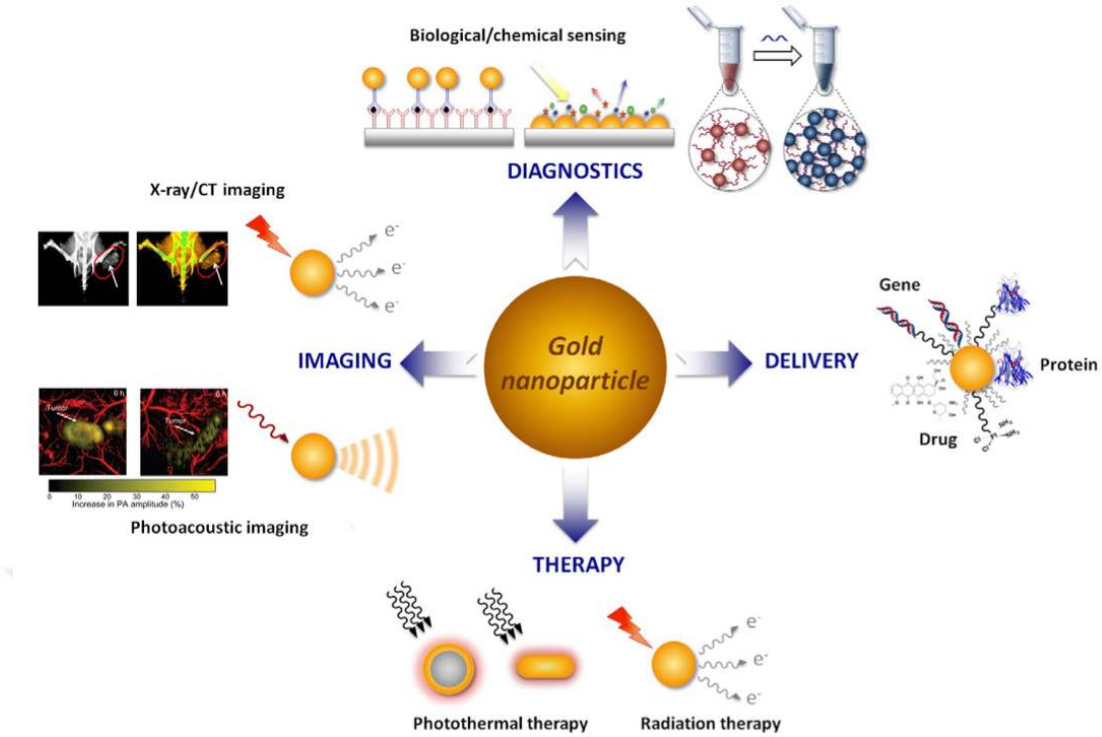

Figure 1.4 Biomedical applications of GNPs [30].

In imaging, GNPs are commonly used as X-ray contrast agents in computed tomography (CT) and positron emission tomography (PET) due to their high X-ray absorption coefficient, biocompatibility, and surface modification potential [31, 32]. While iodinated contrast agents are widely used in the clinic due to their water solubility and low toxicity, they suffer from short blood circulation times and rapid elimination [33]. GNPs possess longer blood retention and are, therefore, superior. GNPs are also potential radiosensitizers for X-ray radiotherapy [34]. By targeting GNPs to the tumor, the local X-ray dose can be enhanced, and the radiotherapy selectivity and efficiency can be improved compared to conventional methods.

Cumulatively, biomedical applications of GNPs, diagnostics, therapy, drug delivery, and imaging point toward the potential of GNPs in the advancement of healthcare. Their unique properties, combined with the ability for surface modification and integration into multifunctional systems, make them indispensable tools in modern medicine. The following chapters will focus on the biomedical applications that are used in the thesis.

1.3 X-ray-based therapies: Radiotherapy and Radiodynamic Therapy

Radiotherapy is a widely used treatment modality that employs high-energy radiation, such as X-rays, γ-rays, electron beams, and protons, to damage or kill cancer cells through direct or indirect damage of DNA. The therapeutic effect is achieved through the generation of secondary electrons, which induce radiolysis of water and lead to the formation of ROS. While radiotherapy offers the advantage of limitless tissue penetration compared to PDT and PTT, it is not without challenges. Dose heterogeneity, side effects on healthy tissues, and the radio-resistance of certain cancer cells are notable concerns associated with this treatment [35].

To enhance the efficacy of radiotherapy, high atomic number (Z) elements, such as bismuth, tantalum, tungsten, and gold, are employed as radiosensitizers [36]. These materials improve radiation delivery to cancer cells due to their strong photon attenuation and increased radiation deposition, as they have a higher mass energy absorption compared to soft tissues. Along with other radiosensitizers, GNPs are valuable due to their unique properties and their broad use in X-ray-based therapy and diagnostics. They offer another method of improving treatment selectivity and reducing harm to healthy tissues.

1.3.1 Radiotherapy with GNPs

GNPs are commonly used as radiosensitizers due to their i) strong photoelectric absorption coefficient, ii) inert nature and low toxicity, iii) ease of surface modification to conjugate or load therapeutic agents, iv) deposition passively to the tumor sites due to enhanced permeability and retention, v) contrast agent properties allowing tracking of cancer cells [36]. Upon X-ray irradiation, biological components go through physical, chemical, and biological mechanisms.

In the keV energy range, X-rays interact with GNPs primarily through the Compton and photoelectric effects (Figure 1.5). The Compton effect, which occurs at energies above 500 keV, involves the ejection of outer-shell electrons by incident photons. The photoelectric effect, dominant in the 10–500 keV range, leads to the ejection of inner-shell electrons. As outer-shell electrons move to fill these vacancies, lower-energy photons (fluorescence) and secondary electrons (Auger electrons) are released. These secondary electrons travel only a few micrometers, creating localized ionization and enhancing radiation-induced damage [37].

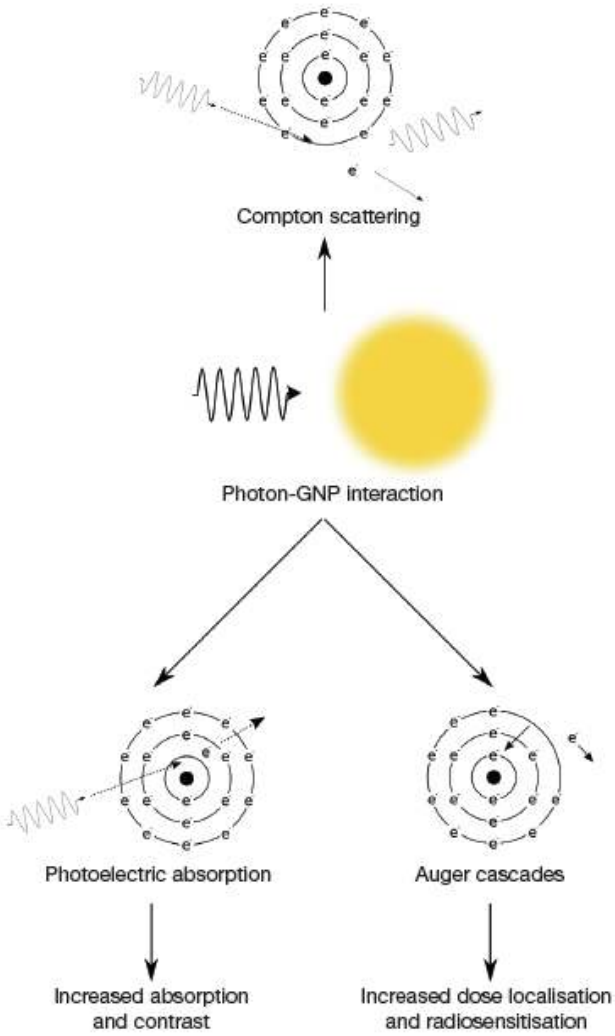

Figure 1.5 Schematic representation of physical events when X-ray interacts with GNPs [37].

Radiosensitization by GNPs also involves chemical processes, particularly the generation of ROS. The high surface-to-volume ratio of GNPs facilitates oxygen interaction, leading to superoxide formation and the subsequent generation of other ROS. A study by Misawa et al. demonstrated that the presence of GNPs increased hydroxyl radical (•OH) and superoxide (O_2^-) levels in water 1.46 and 7.68 times, respectively [38]. This ROS production is primarily attributed to the interaction of photo- and Auger electrons with water molecules, triggering radiolysis and amplifying oxidative stress. Increased ROS levels contribute to a series of biological effects, including DNA damage and oxidative stress, ultimately leading to cell death.

1.3.2 Biological mechanisms of GNP-mediated RT

Another key mechanism in GNP-mediated radiosensitization is the disruption of the cell cycle. The radiosensitivity of cells varies with the phase of the cell cycle, with the late G2 phase being the most sensitive and the late S phase being the most resistant [39]. Upon radiation exposure, cell cycle checkpoints (G1, S, G2) are activated to maintain genomic integrity and facilitate repair [40]. Studies have shown that glucose-capped GNPs track the cells in the G2/M phase, enhancing radiosensitivity by activating cyclin B1 and cyclin E while inhibiting p53 and cyclin A [41]. Similarly, the glucose-coated GNPs have been reported to increase the G2/M phase in SK-OV-3 cells, making them more sensitive to X-ray radiation [42, 43]. However, some studies suggest that smaller GNPs, such as tiopronin-GNPs and triphenyl monosulfonate-GNPs, have minimal effects on cell cycle progression [44, 45]. The influence of GNPs on cell cycle regulation appears to depend on their size, coating, concentration, and specific cell type, making it difficult to establish a general mechanism.

GNPs also enhance radiosensitization by influencing DNA damage and repair mechanisms. Radiation-induced double-strand breaks (DSBs) in DNA are critical for cell survival, and GNPs have been shown to increase the extent of these breaks [46]. γ-H2AX foci analysis has revealed that GNPs enhance early DNA damage (within one hour post-RT), likely due to their perinuclear localization [47, 48]. Sustained damage observed at 24 hours post-RT suggests that GNPs also interfere with DNA repair processes. However, not all GNP formulations exhibit this effect, as BSA-capped GNPs and AuroVist™ GNPs showed no significant impact on DSB repair [49, 50].

Beyond direct radiosensitization, GNPs may also influence intercellular radiation responses through bystander effects. The bystander effect occurs when non-irradiated cells exhibit radiation-like damage due to signals from irradiated cells. Key mediators include reactive oxygen and nitrogen species, cytokines, microRNAs, and extracellular DNA, which can be transmitted through diffusion, receptor binding, or gap junctions [51, 52]. Nanoparticles may modulate these signals, potentially altering cellular responses to radiation.

GNPs also regulate apoptosis by modulating key signaling pathways. The Bcl-2 family proteins, particularly pro-apoptotic (Bax) and anti-apoptotic (Bcl-2) members, play a crucial role in this process. Studies have shown that GNPs combined with radiation increase ROS production, depleting antioxidant defenses such as superoxide dismutase

and glutathione [53]. This oxidative stress leads to DNA damage and apoptosis. For instance, Zhang et al. reported that in HepG2 cells, GNP exposure combined with radiation upregulated Bax and caspase-3 while downregulating Bcl-2, promoting apoptosis via the p53/Bcl-2 pathway [54]. Similarly, Jabir et al. demonstrated that linalool-GNP conjugates (LG and LGC) selectively induced apoptosis in ovarian cancer cells by activating caspase-8 and p53, highlighting the potential of GNPs in targeted cancer therapy.

In addition to apoptosis, GNPs influence autophagy, a process crucial for maintaining cellular homeostasis [55]. While basal levels of autophagy support cell survival, disruptions can have significant consequences. Recent studies suggest that GNPs can either impair autophagic flux or promote autophagy-related cell death, depending on their physicochemical properties and cellular context [56]. Ma et al. found that GNPs enter cells via receptor-mediated endocytosis and accumulate in lysosomes, leading to lysosomal alkalinization and impaired autophagic degradation [57]. This blockage results in autophagosome accumulation and upregulation of autophagy markers like LC3II and p62. In contrast, Joshi et al. reported that 11-mercaptoundecanoic acid-coated GNPs conjugated with chloroquine induced autophagic cell death in breast cancer cells, suggesting a therapeutic potential for autophagy-targeting strategies [58].

GNPs also exhibit context-dependent cytotoxicity under different environmental conditions. Ding et al. found that in normoxic conditions, GNPs promoted autophagy [59]. In contrast, under hypoxia, they induced excessive ROS production, mitochondrial membrane depolarization, and a combination of apoptosis and autophagic cell death. Furthermore, GNPs have been engineered to target specific cancer pathways. Luo et al. demonstrated that quercetin-conjugated GNPs inhibited JAK2 overexpression in cervical cancer cells, simultaneously triggering apoptosis and autophagy through STAT-, PI3K/Akt-, and mTOR-related pathways [60]. These findings indicate the dual role of GNPs in autophagy regulation. While they can disrupt autophagic flux, they can also induce autophagy-driven cell death, making them valuable tools for cancer therapy. However, further research is necessary to optimize their therapeutic potential and minimize unintended effects.

GNPs enhance radiosensitization through multiple mechanisms, including ROS generation, cell cycle disruption, DNA damage, apoptosis, and autophagy modulation. Their effects are influenced by various factors such as nanoparticle size, surface coating, and cellular context. While promising as therapeutic agents, further research is needed to

fully understand their interactions with biological systems and optimize their application in cancer treatment.

1.3.3 In vitro techniques

As discussed in the previous chapters, exposure to radiation may cause cell death through different mechanisms. Detection of radiation-induced cell death is one of the first and most important steps in in vitro cancer research. Clonogenic and MTT assays are the most common techniques used to determine cell viability after radiation-based treatments. The clonogenic assay measures the survival rate of the cells after irradiation, whereas the MTT assay measures mostly the drug toxicity. Even though the clonogenic assay is commonly used for cell survival detection, it has limitations such as the long duration of the experiment, high material consumption, error possibility, and long duration of colony counting; therefore, it is a more difficult method for the optimization experiments with a high number of samples.

Chung et al. studied MTT and Trypan blue assays as alternative methods for clonogenic assay [2]. MTT assay is a colorimetric assay that is based on the reduction of yellow tetrazolium salt – MTT (3-[4,5-dimethylthiazol-2-yl]-2,5 diphenyl tetrazolium bromide) into purple formazan crystals due to the metabolic activity of the viable cells [61]. It is usually performed in a 96-well plate, allowing many samples and replicates, and final absorbance is measured by a microplate reader. Trypan blue, on the other hand, is a dye exclusion assay based on the diffusion of the dye through dead cells' membranes. The stained cells can be counted using a hemocytometer or a microscope [62].

In the experiment done with HEPG2 cells, Trypan blue and MTT were compared at the commonly used cell density for these assays ($1x10^4$ cell/well) (Figure 1.6 A, B)[2]. Cells were irradiated with 0 – 100 Gy, and the results were reported 1, 2, and 3 days after irradiation. here, the MTT assay did not show any sign of cell death, while viability dropped below 20% for trypan blue. Another experiment showed that the viability measured with MTT assay was dependent on the seeded cell density. The optimal cell density for MTT was found with $1x10^3$ cells/well (Figure 1.6 C). In summary, MTT, Trypan blue, and clonogenic assay can give similar results for cell viability measured after radiotherapy with some cell density and assay duration arrangements. To achieve fast results, an MTT assay can be used in optimal conditions; however, it is essential to support the MTT data with a clonogenic assay.

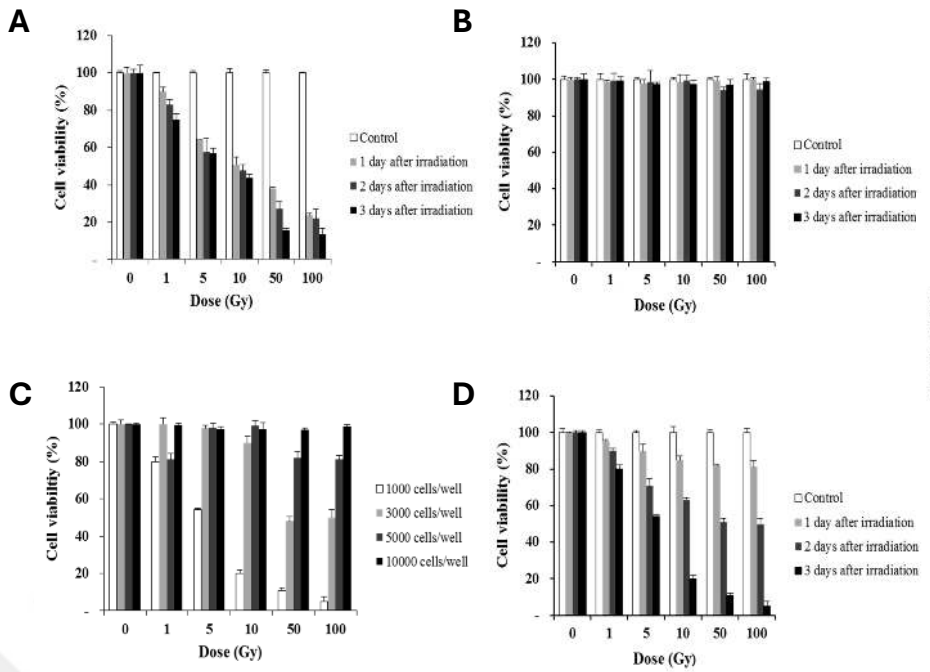

Figure 1.6 Radiation-induced cell viability in HepG2 cells by A) Trypan blue B) MTT assays ($1x10^4$ cell/well). C) Cell viability depends on the cell seeding density determined by MTT assay. D) Post-irradiation time-dependent cell viability was determined by an MTT assay (1×10^3 cell/well) [2].

1.4 Phototherapies: Photothermal- and Photodynamic Therapy

Alongside common cancer treatment modalities such as surgery, radiotherapy, and chemotherapy, phototherapy is a treatment that is gaining attention due to its high locality, low invasiveness, and minimal side effects [63]. The development of nanotechnology allowed phototherapies to be combined with nanoparticles. With surface functionalization, nanoparticles can be decorated with targeting molecules and carry drugs or photosensitizers (PSs), enhancing the treatments with higher localization. Photodynamic therapy (PDT) and photothermal therapy (PTT) are light-activated treatment methods with different damage mechanisms.

1.4.1 Photothermal Therapy

PTT is based on light/laser irradiation to the tissue and local heat generation. In this modality, localized heating of tumor tissue is induced by light-excited PTT agents, which transfer energy to surrounding molecules. Sources that can generate heat are visible/NIR light, microwaves, radiofrequency, and ultrasound waves [64]. This temperature-dependent process triggers different cellular responses: at 42°C, protein denaturation and

temporary cell inactivation occur; at 43–45°C, prolonged inactivation leads to oxidative stress; at 45–48°C, rapid cell necrosis takes place; and at 48–60°C, microvascular thrombosis and ischemia result in immediate cell death (Figure 1.7) [65].

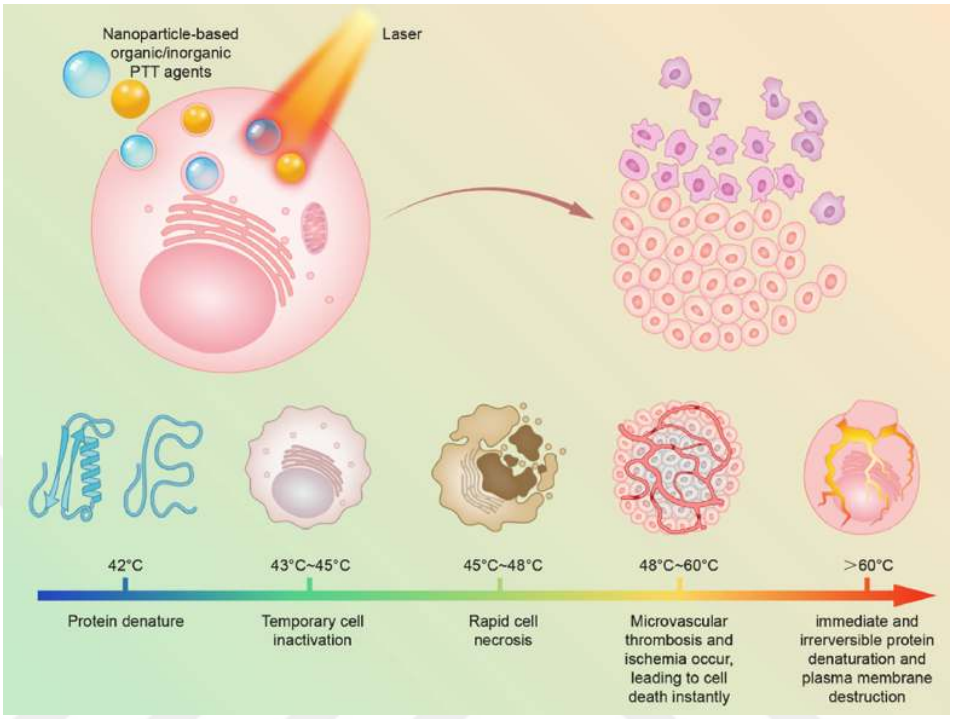

Figure 1.7 Schematic illustration of nanoparticle-induced photothermal therapy and the biological events due to hyperthermia [66].

PTT has shown promising efficacy in vivo models in treating primary tumors and metastases. NIR light is valuable as a source for PTT due to its ability to penetrate deeper into tissues while minimizing absorption by endogenous molecules, thereby maximizing therapeutic efficiency [67]. The therapeutic effect of PTT can be enhanced using organic dyes and photothermal agents, such as metallic nanoparticles, nanocarbons, and organic nanoparticles [68, 69]. Noble metal nanomaterials, such as gold, silver, palladium, and platinum, are highly effective PTT agents due to their strong SPR effect, synthetic tunability, and superior photothermal properties [70, 71]. Their high absorption cross-section and excellent photothermal conversion efficiency in the NIR region make them promising for cancer therapy and bioimaging. By modifying their size, shape, and structure, their SPR bands can be tuned for optimal NIR absorption. Recent advances focus on their application in multimodal theranostics, integrating PTT with chemotherapy, immunotherapy, photodynamic therapy, and imaging for enhanced cancer treatment. For instance, nanostructures loaded with antitumor drugs, such as doxorubicin

and paclitaxel, have demonstrated enhanced anticancer effects through hyperthermia-assisted drug delivery [72]. Additionally, image-guided PTT improves treatment precision, minimizes adverse effects, and allows for better therapeutic planning that leads to improved patient outcomes [72, 73].

1.4.2 Photodynamic Therapy

Photodynamic therapy involves a photosensitizer (PS) and irradiation of light at a certain wavelength to activate the PS. When the PS is activated by light, it transfers the energy to molecular oxygen and generates reactive oxygen species. In more detail, when the ground state PS absorbs activated by light, the excited singlet state may decay to the ground state by emitting fluorescence, and it can be used for fluorescence imaging. Also, it can undergo intersystem crossing and form a more stable triplet state. The triplet state can interact with the biological environment and subsequently with the molecular oxygen-producing superoxide, hydroxyl radicals, and hydrogen peroxide, called type I PDT. On another path, excited PS can directly transfer its energy to the ground state molecular oxygen, producing singlet state oxygen $^1O_2$, which is called type 2 PDT [74]. Figure 1.8 summarizes the nanoparticle-induced *photodynamic* and the biological events due to the generation of ROS.

Key properties of an ideal PS include localization in the tumor while rapidly clearing from normal tissue. Properties extend to minimal dark toxicity, high triplet state quantum yield, and sufficient triplet lifetime to generate ROS. Additionally, activation by light above 700 nm increases the efficiency since it enables deeper tissue penetration, avoiding interference from endogenous absorbers. However, most PSs do not satisfy all of these properties; thus, developing an ideal PS remains a significant challenge.

Nanoparticles offer a promising approach to enhancing PDT by overcoming many limitations of traditional PS. Their small size allows for precise engineering using natural or synthetic materials to deliver multiple theranostic agents in a targeted manner. Key advantages include increased PS loading capacity, controlled drug carriage and release, improved blood circulation, enhanced tumor accumulation via the EPR effect, and surface modifications for better targeting and biodistribution. Some of the nanocarriers for enhanced PDT applications are organic nanoparticles (solid lipid NPs, liposomes, micelles, polymeric NPsprotein NPs), carbon-based NPs (nanotubes, fullerenes, nanotubes), silica NPs, GNPs, magnetic NPs (SPIONs) [75-80].

One other challenge of PDT is the hypoxic environment of the tumor tissue. In order to supply oxygen to the tissue and enhance the PDT effect, strategies including catalysis with NPs to react and generate oxygen or delivery of oxygen via NPs such as liposome-encapsulated hemoglobin and perfluorocarbon carbide were studied [81].

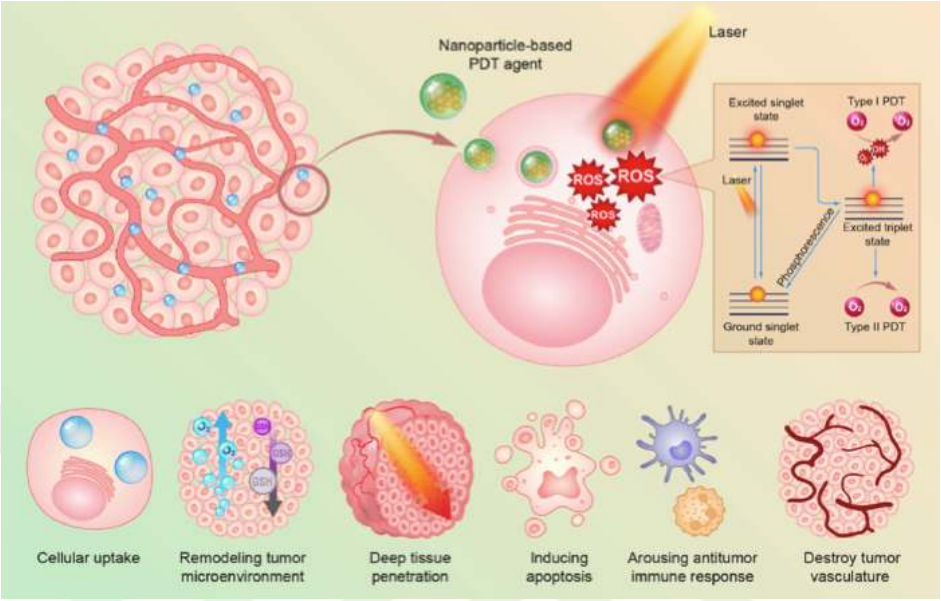

Figure 1.8 Schematic illustration of nanoparticle-induced photodynamic and the biological events due to the generation of ROS [66].

*1.5 **Radiodynamic Therapy***

As discussed in the previous chapter, PDT is a treatment modality based on a PS's light activation and ROS generation. It is an invasive and local treatment method offering a turn-on mechanism. However, the biggest restriction of this treatment method is the low penetration of visible and NIR light for deep-seated tumors. To overcome this limitation, high-energy X-rays and γ-rays are offered to be used as sources to excite PSs. In this dynamic process, high energy sources excite the PS and generate ROS, offering advantages such as deep penetration, higher efficiency compared to PDT, low doses of radiation, and higher localization. Further, it ensures that commonly used PSs such as photofrin, acridine orange, and protoporphyrin IX (PpIX) acid are functional for deep-seated tumors [82-85].

Briefly, the process is called X-PDT or radiodynamic therapy (RDT), depending on the nanomaterial used for the process. If the process is based on the excitation of a nanoscintillator and activation of PS, it is called X-PDT [86]. In X-PDT, luminescent nanoscintillators are excited by X-ray, and their emission matches the absorption of the

conjugated PS by Förster resonance energy transfer (FRET). In radiodynamic therapy, no fluorescence is required; an energy transfer from nanomaterial activates the PS, generating ROS [87, 88]. In summary, the mechanism of X-PDT/RDT includes a mediator nanomaterial as an X-ray antenna or X-ray absorber and a photosensitizer as a dynamic agent.

Nanomaterials with high Z numbers are valuable for the deposition of the X-rays locally to the tumor, as discussed in the radiotherapy section. Nanoscintillators, nano-metal organic frameworks (nMOF), and gold nanoparticles were studied as RDT agents that transfer the radiation energy to PS, increasing cell death and particularly enhancing DNA damage. Zhong et al. designed NaCeF4:Gd, Tb nanoscintillator and showed their X-ray-responsive properties. In this design, they used a single system where the in-the-ground state electrons of Ce^{3+} and Tb^{3+} are excited, with the energy of the secondary electron moving to the conduction band and reacting to molecular O_2 to form ROS [89].

Lu et al. reported the development of two Hf-based nanoscale metal-organic frameworks (nMOFs), which integrate Hf cluster scintillators with porphyrin-based PS ligands [90]. These moves demonstrated structural optimization for RDT and received positive clinical feedback when combined with checkpoint blockade immunotherapy. The Lin group followed their study by designing various Hf-based nMOFs and nanoscale metal-organic layers with tunable properties for RDT applications [91-93].

Gold nanomaterials attract attention due to their strong X-ray absorption properties and their dual role in PDT and radiotherapy. Zhu et al. demonstrated that dihydrolipoic acid-coated gold nanoclusters (AuNC@DHLA) exhibit two-photon excitation and enhance type I energy transfer, generating high ROS levels for PDT [94]. These nanoclusters induce apoptosis and mitochondrial damage while proving more effective and less toxic than conventional PSs. They also trigger antitumor immune responses, potentially preventing tumor recurrence and metastasis.

5-aminolevulinic acid (ALA) is a prodrug, the precursor of protoporphyrin IX (PpIX), which is commonly used as a photosensitizer for PDT [95, 96]. When topically or systemically applied, ALA can accumulate in tumor cells selectively. Toxicity and biodistribution are well-known in the literature, and they are used in the clinic for photodynamic diagnosis and fluorescence-guided surgeries [97]. There are several studies showing that pre-treatment of ALA enhances radiotherapy efficacy, promoting PpIX accumulation in tumor cells and increasing ROS generation, similar to PDT [98-101]. As a radiosensitizer, ALA could have an additive or synergistic effect when combined with

radiotherapy, enabling the treatment of deeper tumors that are beyond the reach of laser-based PDT, as shown in Figure 1.9.

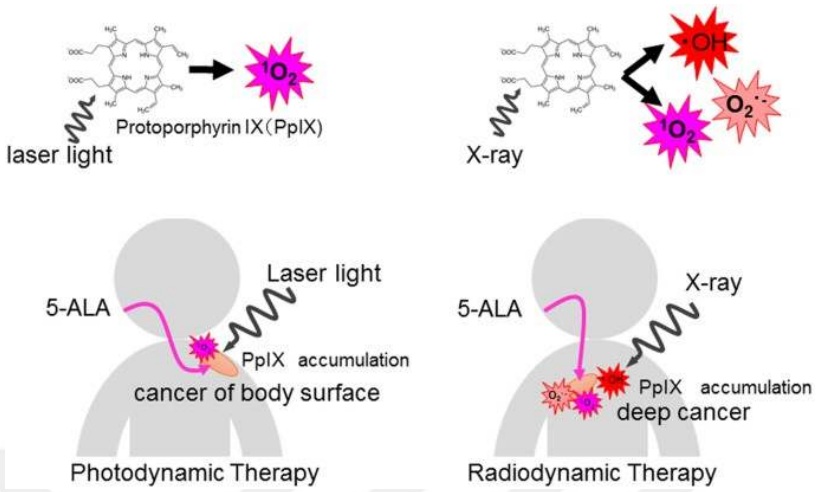

Figure 1.9 Schematic illustration of the usage of PpIX for PDT and RDT [102].

*1.6 **Photoacoustic Imaging***

Imaging is essential in cancer therapies for diagnosis, image-guided surgeries, or delivery of the therapeutic agent locally to the target tumor site with the help of non-toxic contrast agents [103]. Optical imaging offers high contrast based on light absorption and scattering, making it useful for detecting cancer hallmarks [104]. However, its penetration depth is limited due to light scattering in biological tissues. While ultrasound imaging provides deeper tissue penetration, it lacks molecular and functional contrast [105]. Photoacoustic imaging (PAI) overcomes these limitations by combining optical absorption contrast with ultrasonic spatial resolution, achieving imaging depths of up to a few centimeters, beyond the mm limit of optical methods [106, 107].

The photoacoustic (PA) effect occurs when pulsed optical energy is absorbed by biological tissue or contrast agents, leading to transient thermoelastic expansion and the generation of ultrasound waves [108, 109]. Under pulsed laser excitation, endogenous or exogenous contrast agents absorb light, causing rapid heating and expansion, which in turn produces a photoacoustic signal. This ultrasound wave is then detected by an ultrasound transducer on the tissue surface, similar to traditional ultrasound imaging, allowing for the reconstruction of detailed images.

PAI is sensitive to endogenous molecules such as hemoglobin, collagen, water, and lipids since they have absorption in the NIR biological window. Still, the absorption is weak, and exogenous contrast agents are needed for signal enhancement and precise imaging of the tissues [110]. To have a better signal-to-noise ratio, higher penetration depth, low tissue absorbance, and scattering, contrast agents in the biological window (NIR-I, 700-900nm, and NIR-II, 1000-1700 nm) are essential [111].

Various exogenous contrast agents have been developed to enhance PAI in living tissues and diseased areas. Effective PA contrast agents must possess several key characteristics, including strong NIR absorption, good biocompatibility, high photostability, targeted delivery, and favorable pharmacokinetics and metabolism [110]. Some exogenous contrast agents include small organic dyes, semiconducting polymer nanoparticles, carbon nanomaterials, gold nanoparticles, and transition metal dichalcogenides.

Among these contrast agents, GNPs are widely used in PAI due to their straightforward synthesis and tunable absorption properties, which depend on the shape and size of their LSPR. GNPs exhibit longer circulation times in the bloodstream and greater photostability under light irradiation than dyes such as indocyanine green and methylene blue [112]. However, simple GNPs have a single absorption peak, typically around 520 nm, which can be shifted to 600 nm by increasing particle size [113, 114]. To extend absorption into the NIR region, anisotropic GNPs with non-symmetrical structures can be utilized, as they enhance LSPR oscillations along their longitudinal axis [115]. As the aspect ratio of GNPs increases, the longitudinal plasmon band shifts further into the NIR region, making them more suitable for deep-tissue imaging applications.

*1.7 **Gold-gold Sulfide Nanoparticles (GGS)***

Gold–gold sulfide (GGS) nanoparticles are relatively underexplored in the literature; however, their characteristic SPR band around 530 nm, similar to colloidal spherical gold nanoparticles, along with a broader absorption band spanning 650–1100 nm, has raised increasing interest for their biomedical potential. Despite a few reported synthesis approaches, GGS nanoparticles often suffer from low colloidal stability and poor reproducibility. Two key factors contributing to these challenges are the absence of a stabilizing coating during particle growth and the choice of the sulfur source. Sodium sulfide (Na_2S) is the most commonly used sulfur source; however, its use is complicated because it is typically aged before use, which introduces variability in the outcome. One

of the aging byproducts, sodium thiosulfate, can potentially reduce gold ions, further affecting reproducibility.

Recently, we addressed the challenge of synthesizing colloidally stable GGS NPs and subsequently explored their potential as exogenous contrast agents for photoacoustic microscopy (PAM) in the visible and near-infrared regions [116]. To prevent nanoparticle aggregation and achieve colloidal stability, in situ coating of GGS was employed, providing surface passivation along with steric and/or electrostatic repulsion. Stability was achieved through in situ passivation using various coating materials, yielding a portfolio of GGS NPs with distinct surface chemistries. Specifically, anionic, cationic, and protein-coated GGS NPs were synthesized using 3-mercaptopropionic acid (3-MPA), branched poly(ethyleneimine) (bPEI), and bovine serum albumin (BSA), respectively. PEG-SH was incorporated into the 3-MPA and bPEI coatings to further enhance long-term stability. The impact of these coatings on colloidal stability, optical properties, cytotoxicity, and cellular uptake was systematically evaluated. Notably, the GGS NPs demonstrated exceptional stability, with no significant changes in hydrodynamic size or optical properties observed over a year, confirming their robust colloidal and optical performance.

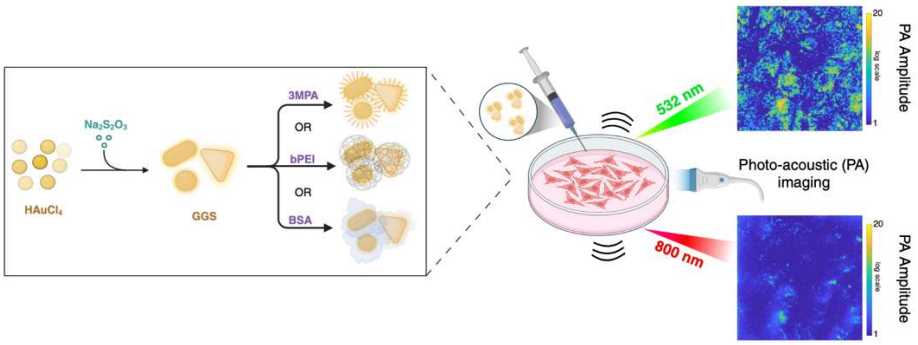

Figure 1.10 Schematic representation of the synthesis of GGS with 3MPA, bPEI, and BSA coatings. This study uses GGS as an exogenous contrast agent for PAM within the visible and near-infrared regions [116].

Despite stability challenges, GGS nanoparticles have been explored as promising theranostic agents in several studies. Day et al. reported the use of GGS as both a contrast and therapeutic agent for multiphoton microscopy and photothermal therapy. In their study, anti-HER2-conjugated GGS specifically targeted HER2-positive SKBR-3 cells, inducing membrane blebbing due to hyperthermia [117]. Gobin et al. demonstrated the potential of PEG-coated GGS as NIR PTT agents both in vitro and in vivo, highlighting

their biodistribution. Notably, GGS accumulation in the liver, spleen, and tumors suggested preferential tumor targeting over clearance by the reticuloendothelial system (RES), in contrast to gold/silica nanoshells [118]. Additionally, Huang et al. investigated the in vivo toxicity and biodistribution of 11-mercaptoundecanoic acid-coated GGS as a chemotherapeutic drug carrier, finding that nanoparticles at concentrations below 200 μg/mL exhibited good biocompatibility and safety [119]. Overall, GGS has the potential as a theranostic platform for further research to enhance its stability and clinical applicability.

1.8 ***Proposal and the Aim of the Thesis***

Cancer treatment is highly complicated, and it is the cause of one of the six deaths worldwide [120]. The most commonly used methods for the treatment are surgery, chemotherapy, and radiotherapy. Besides the success of these treatments, they have some limitations due to the heterogeneous structure of the tumor, lack of specificity, side effects, resistance, and metastases of cancer. Surgery is a successful but invasive method and can only be used for solid tumors. Some cancer cells may be left in the body after surgery; therefore, it is mainly combined with chemotherapy or radiotherapy. Chemotherapy has high side effects on healthy tissues, it lacks tumor specificity, and most of the time, due to short circulation time in the body or drug resistance, it is not sufficient when used alone. Radiotherapy can be applied locally, but it damages the surrounding healthy tissues and causes side effects as well.

Researchers are developing alternative treatment methodologies to increase the survival rate and improve patients' comfort. Nanotechnology is an essential platform for cancer theranostics and can be combined with conventional treatments to enhance tumor specificity and efficacy. Using nanoparticles, chemotherapeutic drugs can be carried to the tumor site, and image-guided combinational therapies can be applied. Theranostic nanoparticles include polymeric NPs, carbon dots, semiconducting quantum dots, gold NPs, and magnetic nanoparticles. Gold NPs are commonly used in cancer research due to their inert nature, ease of surface functionalization, precise size and shape control, tunable optical properties, and CT contrast.

NIR-absorbing GNPs are worthy in nano-theranostics, providing an opportunity to work in the "biological optical window" for medical imaging, surpassing the autofluorescence of the tissues and absorbance of the endogenous components, allowing

deeper penetration. Gold-gold sulfide nanoparticles with absorbance in visible and NIR regions are promising tools, especially for light-based applications such as imaging and photothermal therapy. In our previous studies, we enhanced the long-term colloidal stability of GGS with anionic, cationic, and protein functional coatings and showed their potential in broad-band photoacoustic imaging [116].

Phototherapy has gained attention due to its non-invasive application and high locality. PTT is based on the generation of hyperthermia by absorbing light and converting the light energy to heat. PDT is based on the photoactivation of a photosensitizer, which generates reactive oxygen species and singlet oxygen that cause cell death. Besides their advantages, the penetration of light and the ability to reach the tumor are the biggest challenges of phototherapies. Nanoparticles are helpful in enhancing the effect of light, selectively accumulating in the tumor area, and carrying chemotherapeutic drugs and PS for combinational therapies. However, PSs used in the clinic suffer from penetration depth of blue-red light used for the existing PSs, limiting the therapy the surface of the tissue or in case of large tumors.

Radiotherapy, on the other hand, has unlimited penetration depth in the body, allowing it to reach out to the deep tumor sites. The radiation doses used for the treatment are effective but highly destructive for the healthy tissues. GNPs are well-known radiosensitizers and valuable tools that enhance the effect of radiation by accumulating in the tumor area. GNPs have been successfully studied in vitro and in vivo models for imaging and radiotherapy.

Recently, an innovative strategy called “radiodynamic therapy” attracted attention, as it follows the photodynamic therapy process, but it uses X-ray instead of light as the irradiation source. Therefore, it bypasses the issue of light penetration into deep-seated tumors, and some photosensitizers may be activated with X-ray in this modality. This highly local, simple, but smart strategy can be promising for treating the various cancer types.

Looking at the limitations of cancer treatment, this thesis offers novel materials and approaches to improve the therapeutic outcome while reducing the side effects. This thesis proposes GGS nanoparticles as a new generation of theranostic nanoparticles delivering a combination of treatment modalities. GGS is offered for this task because:

- Its synthesis is more straightforward and robust compared to gold nanoparticles, especially to those with shape anisotropy providing NIR absorbance.
- Its strong NIR-absorbance offers long wavelength PAI and PTT potential.

- High-Z offers CT contrast.
- High-Z offers low-dose radiosensitization, preferably at and below 4 Gy, which would reduce the radiotoxicity on healthy tissue and reduce the side effects of traditional RT.
- Provide an opportunity to combine mild NIR-PTT with low-dose RT, maximizing the therapeutic effect locally.
- Provide advanced control in the locality of the treatment by using otherwise non-toxic agents in the absence of X-ray and/or laser irradiation.
- Imaging of GGS would allow timely irradiation of the tumor-accumulated nanoparticles and highlight the precise location that needs to be irradiated, again maximizing the toxicity locally and minimizing off-target toxicity and side effects.
- Functional surfaces may deliver ALA to tumors, which provide RDT with X-ray, bypassing the limitation of light penetration in traditional PDT.
- Functional surfaces may deliver site-specific, on-command, highly local RDT/RT and PTT/RT combination therapies
- Functional surfaces may be tagged with tumor-specific ligands for improved specificity.

In the first chapter, a combination of radiotherapy and radiodynamic therapy was investigated using ALA-loaded GGS theranostic nanoparticles. ALA was loaded onto cationic bPEI-GGS nanoparticles designed for low-dose X-ray activation. ALA is a clinically approved prodrug, but its quick clearance from the body limits its bioavailability, and high ALA doses are needed in the clinic. Firstly, ALA-loaded GGS would stabilize ALA and enhance its delivery and bioavailability in tumors, maximizing its effect in tumors at low doses. Secondly and most importantly, bPEI-GGS loaded with ALA should improve RDT efficacy through simultaneous radio-sensitizing and photosensitizing effects under low-dose X-ray irradiation, preferably between 0.5-4 Gy X-ray doses. Sensitized GGS would trigger ALA-RDT, providing a combination therapy. ALA on GGS could provide a level of tumor selectivity for ALA-GGS towards PEPT1/PEPT2 overexpressing tumors due to enhanced transport of ALA via PEPT1/PEPT2. Overall, ALA-GGS would bring about enhanced imaging-guided tumor therapy with otherwise non-toxic species utilizing deep-penetrating low-dose X-rays that

provide locality and on-commend toxicity in selected tumor tissue. In vitro studies on prostate cancer (PC3) and breast cancer (MDA-MB-231) cell lines provide proof for selectivity, low-dose RDT/RT therapy success, and information on cell-death mechanisms. This dual-therapy approach shows promise for advancing low-dose radiotherapy and RDT, especially for deep-seated and resistant tumors, providing insights for future clinical applications.

The second chapter of the thesis offers a combination therapy utilizing solely GGS nanoparticles: NIR mild PTT and RT. The hypothesis is sensitization of the tumor to RT by initial mild hyperthermia using NIR-PTT to maximize the efficiency of low-dose X-ray. GGS's NIR absorbance eliminates the need for another photosensitizer for PTT. Anionic 3MPA-GGS nanoparticles, which are potentially safer in vivo, were functionalized with folic acid to selectively target folate receptor-positive (FR+) cancer cells, improving therapeutic specificity and efficacy. FA-3MPA-GGS is expected to convert NIR light (808 nm) to heat for PTT in addition to NIR PAI, CT contrast, and radiosensitization. In vitro studies performed on FR+ HeLa and MDA-MB-231 and FR-A549 cell lines should provide proof to support the hypothesis.

The third chapter of the thesis offers an alternative away from RT and explores the PDT/PTT combination utilizing ALA-loaded superparamagnetic iron oxide nanoparticles (SPIONs). SPION-based PTT was demonstrated previously by our group on prostate cancer. Here, ALA-loaded poly(acrylic acid) coated SPIONs (ALA-PAA-SPIONs) for selective PTT/PDT combination therapy of prostate cancer cells with PEPT1/PEPT2 overexpression was suggested as an improved imaging-guided mild phototherapy under red-light illumination. These transporters allow ALA to act as a targeting agent in cancer therapy. Therapeutic outcome was tested on LNCaP, PC3, and DU145 prostate cancer cell lines with different PEPT1/PEPT2 expression levels. ALA-PAA-SPIONs were proven to be potential nanoparticles for effective dual-mode phototherapy for prostate cancer treatment with single wavelength irradiation (640 nm, 300 mW, 10 min).

Chapter 2: Gold-Gold Sulfide Nanoparticles for X-ray-Activated ALA-Based Radiodynamic Therapy in Cancer Cells

2.1 Abstract

Radiodynamic therapy (RDT) is an emerging cancer treatment that utilizes high-energy radiation as the irradiation source, along with an X-ray absorber and a photosensitizer. This approach has attracted attention for its ability to achieve effective treatment with low-dose radiation, enable deep tumor penetration, and extend the applicability of conventional photosensitizers, typically activated in the visible range, to target deep-seated tumors. Here, we electrostatically loaded 5-aminolevulinic acid (ALA) to branched polyethyleneimine-coated gold-gold sulfide nanoparticles (bPEI-GGS) as a promising approach for enhancing RDT in cancer treatment. ALA, a prodrug converted into the photosensitizer protoporphyrin IX (PpIX) within cancer cells, combined with bPEI-GGS nanoparticles designed for X-ray activation. Upon X-ray irradiation, the nanoparticles generated reactive oxygen species (ROS) and enhanced radiation-induced DNA damage, promoting cell death. In vitro studies with prostate cancer (PC3) and breast cancer (MDA-MB-231) cell lines revealed significant radiosensitization effects, particularly in PC3 cells, due to ALA targeting and increased PpIX-mediated ROS production. Mechanistic studies indicated that RDT with ALA-bPEI-GGS nanoparticles triggered apoptotic and autophagic pathways, with autophagy playing a crucial role in PC3 cell death. Inhibiting autophagy via CRISPR/Cas9 knockout of ATG5 significantly reduced cell death, highlighting the interaction between autophagy and apoptosis in RDT. This dual-action approach is promising for advancing targeted RDT, especially for deep-seated and resistant tumors, providing an alternative strategy for future clinical applications.

2.2 Introduction

Cancer remains a major global health challenge and drives continuous exploration of novel treatment strategies. Photodynamic therapy (PDT) has emerged as a promising non-invasive, localized treatment alternative to conventional therapies [121, 122]. PDT relies on light activation of photosensitizers (PS), leading to the generation of cytotoxic reactive oxygen species (ROS) such as singlet oxygen (O2•), hydrogen radicals (H•), and

hydroxyl radicals (•OH) [67, 123, 124]. While PDT offers significant advantages, including minimal invasiveness and local phototoxicity, the restricted penetration of light into deep tissues remains a significant challenge. Developing new-generation photosensitizers that may be activated with visible or near-infrared light sources is critical in advancing PDT [125, 126].

In contrast, X-rays, the primary modality in radiotherapy, offer high tissue penetration, enabling the treatment of deep-seated tumors. These high-energy ionizing radiations directly induce DNA damage and indirectly produce ROS, which can attack DNA and various cellular components, leading to apoptosis and necrosis in cancer cells [127-129]. However, radiotherapy also has drawbacks, such as suboptimal energy deposition due to low X-ray attenuation in biological tissues, reduced efficacy in hypoxic, radioresistant tumors, and side effects, as well as toxicity on the healthy tissues [130].

Radiodynamic therapy (RDT) offers a potential solution, combining X-rays' deep penetration with photosensitizers' ROS-generating ability to enhance localized radiotherapeutic effects [90]. Photosensitizers like hematoporphyrin derivatives (HpDs), protoporphyrin IX (PpIX), photofrin, acridine orange (AO), and rose bengal (RB) have demonstrated effectiveness in X-ray-activated ROS generators [83-85, 131].

5-Aminolevulinic acid (ALA) is a new-generation prodrug for PDT with great potential. ALA is an endogenous precursor of a natural photosensitizer protoporphyrin IX (PpIX). Exogenous ALA is metabolized to PpIX via the heme biosynthetic pathway, more so in cancer cells due to disturbed heme pathway providing a level of tumor selectivity [132]. ALA was approved by the FDA in 1999 for topical use in the treatment of actinic keratosis via blue light irradiation and in 2017 for fluorescence imaging in glioma surgery due to the red fluorescence of PpIX [133]. It is also zwitterionic and highly soluble in water, which is advantageous compared to traditional PSs, causing its quick clearance from the body, which minimizes the extended light sensitivity of skin but limits its bioavailability. Nanocarriers may enhance ALA`s stability, delivery, and bioavailability and, hence, allow dose reduction accompanied by improved PDT efficiency [134-136]. PpIX is typically irradiated with blue light (410-420 nm) but lately also with red light (630-640 nm). Such long-wavelength activation is an important improvement in terms of light penetration depth, yet still limited to 1-5 mm depth [133]. Intratumoral irradiation may be needed for large and/or deep-seated tumors in case of blue or red-light irradiation. From the perspective of light penetration, X-ray irradiation of PpIX offers tremendous advantages. Takahashi et al. demonstrated that X-ray

activation of PpIX leads to the generation of ROS [137]. This process is facilitated by Cherenkov radiation, which is emitted upon X-ray interaction with biological tissues. Cherenkov light has a wavelength range of 370–430 nm, overlapping with the absorption band of PpIX at 380–405 nm, enabling its excitation [138]. Following this work, other studies have further explored the use of ALA as a precursor of PpIX as a radiodynamic agent for various cancer treatments [99, 100, 139-141].

X-ray radiotherapy has been utilized either as the only method or in combination with other treatment methods in more than 70% of cancer cases [142]. Light doses of around 70 Gy are typically needed for successful treatment [143]. In order to reduce toxicity and side effects in healthy tissue, the dose of ionizing radiation needs to be lowered significantly. Nanomaterials with a high atomic number (Z) are particularly effective in sensitizing tumors for RT due to their enhanced X-ray attenuation, which boosts the radiotoxicity and reduces the X-ray dose [31]. Gold nanoparticles (GNPs) featuring high atomic numbers (Au, Z=79) show excellent X-ray absorption, biocompatibility, tunable size and shape, and surface functionalization potential [30]. When exposed to ionizing radiation, these nanoparticles emit photoelectrons, Compton electrons, and Auger electrons through interactions like the photoelectric and Compton effects, resulting in DNA damage, cell cycle disruption, radiolysis of water, ROS production and, ultimately, apoptotic cell death [30, 144-147]. Therefore, gold nanoparticles have been shown to enhance radiotherapy significantly [148-152]. In vitro studies report that their radiation dose enhancement factor ranges from 1.1 to 25, depending on factors such as GNP size, radiation energy, and cell line [47, 153-156].

Utilization of radiosensitizing nanoparticles loaded with ALA may offer multiple advantages in cancer treatment: radiosensitization and reduction in X-ray dose, improved stability and delivery of ALA to tumors, activation of PpIX with X-rays bypassing the blue-red light penetration limitation.

We recently developed a gold-gold sulfide nanoparticles (GGS) portfolio with various functional coatings and enhanced colloidal stability [116]. These GGS nanoparticles are produced in aqueous solutions in a low-cost, highly reproducible manner. The functional groups provided by the coating on GGS enable the attachment of various agents, including photosensitizers, such as ALA.

In this study, we investigated GGS as a radiosensitizer and the possibility of achieving enhanced radiotoxicity under low-dose X-ray irradiation by combining ALA-RDT with GGS-RT via loading ALA to GGS. ALA-loaded GGS will provide a

combination of RDT and RT simultaneously with a single agent activated with a single source, deep-penetrating X-ray. Such an approach would also improve the bioavailability of ALA and, therefore, enhance ALA-RDT. We designed branched polyethyleneimine-coated gold-gold sulfide nanoparticles (bPEI-GGS) loaded with ALA to test the hypothesis. The cationic nature and functional polymeric coating of bPEI-GGS facilitate the electrostatic loading of ALA, enhancing its stability and bioavailability. RT and RDT were tested at low X-ray doses between 0.5, 1, 2, and 4 Gy. Initial in vitro activity assessments were performed on PC3 prostate cancer and MDA-MB-231 breast cancer cell lines. The literature shows that ALA can be transported by PEPT1 and PEPT2 [157, 158], which may provide selectivity. Upregulation of PEPT1/PEPT2 in PC3 cells can present a valuable target for enhancing delivery and specificity in treatment.

Results demonstrate that bPEI-GGS is highly effective in radiosensitization, and ALA-GGS provides high radiotoxicity via RT-RDT combination at low X-ray doses. Hence, we propose ALA-GGS as a promising new radiosensitizer and RT-RDT as a potential strategy for low-dose radiation therapy.

*2.3 **Materials and Methods***

2.3.1 Materials

Gold (III) chloride trihydrate ($HAuCl_4 \cdot 3H_2O$) and sodium thiosulfate pentahydrate ($Na_2S_2O_3 \cdot 5H_2O$) were supplied from Sigma–Aldrich. Branched poly(ethyleneimine) (bPEI) with an average molecular weight of 10 kDa was purchased from Polysciences (USA). Methoxy poly (ethylene glycol) thiol (mPEG-SH) with an average molecular weight of 2kDa was bought from Laysan Bio, Inc. (USA). 5-Aminolevulinic acid hydrochloride (ALA) was from Research Products International (RPI, USA). Vivaspin 20 centrifugal filters were provided by Sartorius (Germany). All chemicals were of the highest purity or analytical grade, and only ultra-pure water was used (18.2 MΩ, Rephile Bioscience, and Technology, Shanghai, China).

Roswell Park Memorial Institute 1640 (RPMI) medium, Dulbecco's Modified Eagle Medium (DMEM), fetal bovine serum, trypsin-EDTA, L-glutamine, and penicillin-streptomycin were purchased from Diagnovum (Germany). Dimethyl sulfoxide Hybri-Max™ was from Sigma (USA). Phosphate-buffered saline (PBS) tablets and thiazolyl

blue tetrazolium bromide (MTT) were obtained from Bio-matik Corp. (Canada). 96- and 6-well plates were obtained from Nest Biotechnology Co. Ltd. (China).

2.3.2 Synthesis of bPEI-GGS

Synthesis of bPEI-GGS was done based on our previous work [116]. $6.6x10^{-3}$ mmol $Na_2S_2O_3$ solution was rapidly added into $8.55x10^{-3}$ mmol $HAuCl_4$. After 10 min of reaction, coating solutions of bPEI and mPEG-SH with mol ratios of bPEI:mPEG:Au 0.01:0.09:1 were injected into the reaction solution under vigorous stirring at room temperature (RT). After 30 minutes of reaction, the colloidal solution was washed several times with DI water using 30 kDa centrifugal filters to remove excess chemicals, filtered through 0.2 μm syringe filters, and stored in the dark at 4 °C.

2.3.3 Electrostatic loading of ALA to bPEI-GGS (ALA-bPEI-GGS)

ALA was dissolved in water at pH 7 and filtered using a 0.2 μm sterile filter. bPEI-GGS in water at pH 7 was titrated and mixed with ALA at RT for 1 h. Electrostatic loading was confirmed with Isothermal titration calorimetry (Affinity ITC, USA). bPEI-GGS NPs (1 mL, 1 mg/mL in water) were titrated with ALA (250 μL from 5 mg/mL in water) at a rate of 10 μL/s at 25°C. Exotherms observed throughout the titration confirmed the complete binding of 1/1 wt electrostatically (Figure 2.1D). ALA-bPEI-GGS was freshly prepared before every experiment, using the obtained ratio. Therefore, after the electrostatic loading, no washing was performed.

2.3.4 ALA Release

The release rate of ALA from the NPs was studied at pH 5.5 and 7.4 values. ALA-bPEI-GGS NPs (5 mL, 35 mg NP) were added to a 3500 MWCO dialysis bag and put into 200 mL of PBS buffer (pH 5.5 and 7.4) under constant stirring (100 rpm) at 37 °C. 2 mL of PBS solution was collected, and 2 mL of fresh PBS was added to the release beaker. The absorbance vs concentration standard curve was prepared with the ALA in PBS at pH 5.5 and 7.4 at 280 nm. Then, the amount of released ALA from NPs was calculated.

2.3.5 Characterization

The gold content of the NPs was determined using an Agilent 7700X inductively coupled plasma-mass spectrometer (ICP-MS). The samples were digested with aqua regia

solution (HCl/ HNO_3: 3/1 v/v). The organic content of the NPs was obtained by thermogravimetric analysis (TGA). The absorption spectrum of the NPs was measured by a Shimadzu UV-VIS-NIR spectrophotometer between 450 and 1300 nm. Malvern Zetasizer Nano ZS measured hydrodynamic sizes and zeta potentials. The size and shape of NPs were investigated with Hitachi 7800 TEM analysis.

2.3.6 Cell Culture

PC3 prostate cancer cells were cultured in RPMI, and L929 healthy fibroblast and MDA-MB-231 triple-negative breast cancer cells were cultured in DMEM medium supplemented with 10% fetal bovine serum, 2% L-glutamine (2 mM), and 1% penicillin-streptomycin at a 37 °C incubator with 5% CO_2 atmosphere. Cells were washed with PBS and trypsinized with 0.05% trypsin-EDTA before passage and seeding.

2.3.7 Cytotoxicity Assay

MTT metabolic activity assay was used to determine the cytotoxicity of NPs. NP solutions were sterilized by 0.2 μm sterile filters. L929, PC3, and MDA-MB-231 cells were seeded into 96-well plates with $2.5x10^3$ cells per well density. After overnight incubation of the seeded cells, the medium was replaced with a fresh medium, and NPs were added to the wells at 6.25-200 μg Au/ml concentration for 24 h. Then, the medium of the cells was removed, MTT reagent (5mg/mL in PBS) and medium were mixed with the volume ratio of 1:3, added to wells, and incubated for 4 h. Formed formazan was dissolved by adding 200 μL of ethanol: DMSO (1:1 v/v) solution. The formation of formazan crystals shows the metabolic activity of viable cells. The absorbance of the solution was measured by Synergy H1, BioTek Instruments microplate reader at 570 nm, and 650 nm was taken as a reference. The viability of the cells was calculated with the equation viability (%) = 100 x absorbance (treated) / absorbance (control) (n =5).

2.3.8 Cellular Uptake

The cellular uptake of NPs was determined quantitatively using ICP-MS analysis measuring the Au content of NP-treated cells. PC3 and MDA-MB-231 cells were first seeded in a 6-well plate at a density of 2×10^5 cells per well, using the complete medium, and then incubated for 24 hours at 37 °C with 5% CO_2. After incubation, the cells were exposed to bPEI-GGS and ALA-bPEI-GGS at a 100 μg Au/ mL concentration for 24

hours. To remove non-internalized particles, the cells were washed with PBS and then collected after trypsinization at RT for 20 minutes. The cells were then digested in an aqua regia solution (HCl/ HNO_3: 3/1 v/v) at room temperature for one week. The Au content was subsequently quantified using ICP−MS (n = 3).

2.3.9 Measurement of PpIX

PC3 and MDA-MB-231 cells were seeded as were seeded following the procedure outlined in the cytotoxicity assay section. The cells were then incubated for 24 hours with bPEI-GGS, ALA, and ALA-bPEI-GGS at a 25 µg Au/ mL concentration. After the NP incubation, the medium was replaced with a serum-free medium, and PpIX fluorescence was measured using a microplate reader with excitation and emission wavelengths at $\lambda_{ex}/\lambda_{em}$ = 420/635 nm (Synergy H1 microplate reader (BioTek)).

2.3.10 Radiodynamic therapy

Cells were seeded for in vitro RDT studies using the procedure described for the cytotoxicity assay. Both cell lines were treated with bPEI-GGS, ALA, and ALA-bPEI-GGS at 12.5-37.5 µg Au/ mL concentrations. After 6 h and 24 h incubation with NPs, the medium in the wells was replaced with fresh medium. Then, the cells were irradiated with 0.5, 1, 2, and 4 Gy doses of X-ray on an X-ray irradiator (Xstrahl Life Sciences, CIX cabinet). After an overnight incubation, the cell viability was measured using the MTT assay. Untreated cells were referred to as control, and cells not treated with the samples but with X-ray irradiation were referred to as RT control.

2.3.11 ROS generation

For ROS detection of NP solutions, 10 µM DCFH-DA dye was added to the bPEI-GGS, ALA, and ALA-bPEI GGS solutions between 12.5-37.5 µg Au/ mL concentrations. Then, the materials were irradiated with a 2 Gy dose of X-ray. Fluorescence intensity was read at $\lambda_{ex}/\lambda_{em}$ = 485/535 nm in a microplate reader.

PC3 and MDA-MB-231 cells were treated with bPEI-GGS, ALA, and ALA-bPEI-GGS at 25 µg Au/ mL for intracellular ROS detection. After 24 h of incubation, the medium of the cells was removed, washed with PBS, and treated with 10 µM DCFH-DA

for 40 min at 37 °C. Then, each group was irradiated with 0.5 Gy. Fluorescence intensity was read at $\lambda_{ex}/\lambda_{em}$ = 485/535 nm.

2.3.12 Live/dead staining

PC3 and MDA-MB-231 cells were treated with bPEI-GGS, ALA, and ALA-bPEI-GGS at 25 µg Au/ mL for 24 h and irradiated with 0.5 Gy dose of X-ray as described in the radiodynamic therapy section. After 24 h post-irradiation, cells were stained with Calcein-AM and ethidium bromide using a live/dead cell viability kit according to the manufacturer's protocol (Abcam). Fluorescence images were obtained using a fluorescence microscope (Zeiss Axio observer Z1).

2.3.13 Clonogenic assay

PC3 and MDA-MB-231 cells were seeded in a 6-well plate at a density of 500 cells per well, using the complete medium, and incubated for 24 hours at 37 °C with 5% CO_2. Then, cells were treated with NPs at 12.5 µg Au/ mL for 24 h, and the treatment group was irradiated with a 0.5 Gy dose of X-ray. Each group was repeated three times. The medium of the cells was replaced with fresh medium every three days. At the end of 10 days of culture, the cells were washed with PBS and fixed with cold methanol for 10 minutes. Then, the cells were stained with 0.5% crystal violet for 10 minutes and washed with PBS to remove un-attached dye.

2.3.14 Establishment of ATG5KO PC3 cells

PC3 ATG5 KO cells were generated in Gözüaçık laboratory by using the CRISPR/Cas9 system following the method of our previous publication [159]. PC3 cells were transduced with lentiviruses in the presence of 5 µg/ml of polybrene. 48 h later, the selection was carried out by the administration of selection antibiotic puromycin (1 µg/ml) for 5 days.

2.3.15 Protein extraction, Immunoblot analysis, and antibodies

Protein extraction was performed with RIPA buffer (50 mM TRIS-HCl pH 7.4, 150 mM NaCl, 1% NP40, 0.25% Na-deoxycholate) supplemented with a complete protease inhibitor cocktail (Roche, 04-693-131-001) and 1mM phenylmethylsulfonyl fluoride (PMSF; Sigma-Aldrich, P7626). For phosphorylated proteins, protein extraction

was performed with RIPA buffer supplemented with complete protease inhibitor cocktail and phenylmethylsulfonyl fluoride (PMSF; Sigma-Aldrich, P7626) and 100 nM okadaic acid, 1 μM cyclosporine A, 1 mM NaF, 50 mM β-glycerophosphate. Cell extracts (30-50μg) were separated in 15-10 % SDS-polyacrylamide gels and transferred to Nitrocellulose membranes (Amersham, GE10600002). Immunoblotting was performed as previously described [160]. Primary antibodies (ab) were used in this study: anti-Caspase-3 ab (CST, #9662, dilution 1:1000), anti-PARP ab (CST, #9542, 1:1000), anti-p-H2A.X (Milipore-05-636, 1:2000), anti-LC3 (CST, #2775, dilution 1:1000), anti-p62 (Abnova, H00008878, 1:4500), anti-β-actin/ACTB ab (Sigma-Aldrich, A5441, dilution 1:10.000). Protein bands were revealed with chemiluminescence under Chemidoc MP. Band intensities were quantified using ImageJ software.

2.3.16 Immunofluorescence staining

Cells were fixed with 4% paraformaldehyde and permeabilized in PBS with 0.1% BSA (Sigma, A4503) and 0.1% saponin (Sigma, 84510). Immunostaining was performed using an anti-LC3 antibody (Sigma-Aldrich, L7543, dilution 1:200) and anti-p62 (Abnova, H00008878-M01). As secondary antibodies, anti-mouse IgG Alexa Fluor 488 (Invitrogen, catalog no. A11001) and anti-mouse IgG Alexa Fluor 568 (Invitrogen, catalog no. A11004) were used. Cells also were co-stained with Hoechst for 10 min. (BD 33442). Cover slides were mounted and inspected under fluorescent microscopy (Olympus, BX53F).

2.3.17 Statistical Analysis

Tukey's multiple comparison tests were used for the statistical analysis of quantitative results (GraphPad Software, Inc., USA). All data were expressed as mean ± standard deviation (SD), and $p < 0.05$ was considered statistically significant.

2.4 ***Results and Discussion***

2.4.1 Development of bPEI-GGS and ALA-bPEI-GGS nanoparticles

Cationic, bPEI-coated GGS NPs were synthesized in a single-step aqueous reaction and fully characterized by our group [116]. These NPs have two specific absorption peaks at 530 nm and 750 nm (Figure 2.1A). TEM images show that bPEI-

GGS consists of small spherical nanoparticles with a diameter around 2–3 nm and large non-spherical particles with 20-30 nm edges (Figure 2.1B). The diffraction pattern showed rings corresponding to the (111), (200), (220), and (311) reflections of the face-centered-cubic (fcc) structure of gold (Figure 2.1C). The hydrodynamic size of bPEI-GGS NPs was 2.5/64.6 nm (number-based/intensity-based average), with a zeta potential of +7.1 mV (Table 2.1). Zwitterionic ALA was electrostatically loaded to the NPs without significantly changing the hydrodynamic size or absorbance characteristics of the NPs (Table 2.1). The electrostatic loading of ALA was confirmed by ITC with strong titration exotherms (Figure 2.1D).

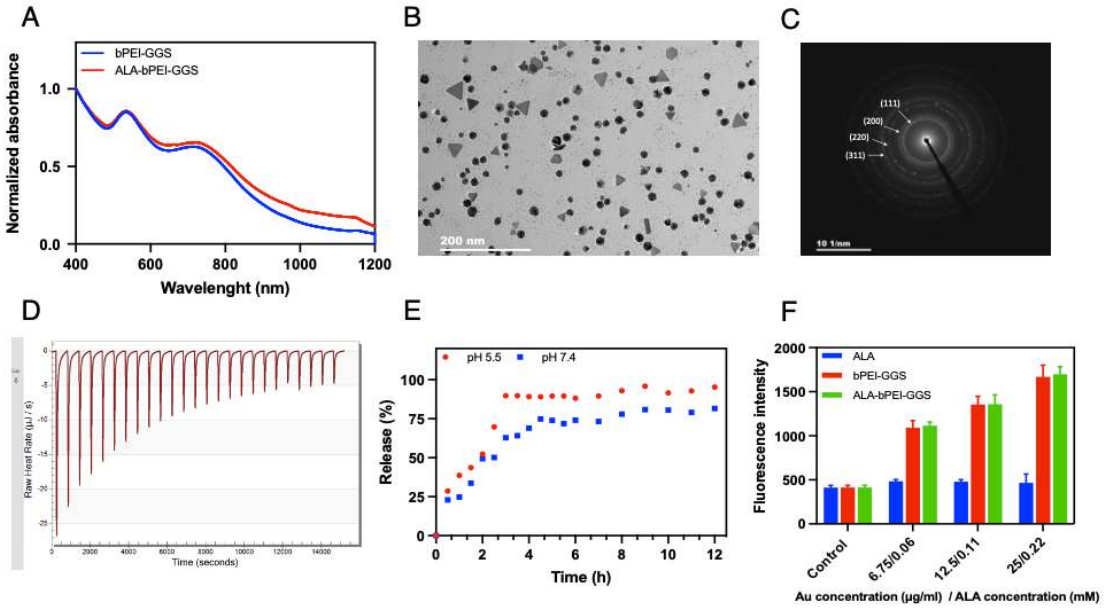

Figure 2.1 A) UV−vis spectra of bPEI-GGS and ALA-bPEI-GGS. B) TEM image and C) electron diffraction pattern of bPEI-GGS. D) Isothermal titration calorimetry (ITC) of ALA-bPEI-GGS NPs in PBS at pH 7. E) the pH-dependent release of ALA from ALA-bPEI-GGS NPs. F) Dose-dependent ROS production of bPEI-GGS, free ALA, and ALA-bPEI-GGS upon 2 Gy irradiation.

Table 2.1 Hydrodynamic sizes and surface zeta potentials of the nanoparticles.

Sample	Dh-number[a] (nm)	Dh-intensity[b] (nm)	Zeta potential (mV)
bPEI-GGS	2.522	64.60	+7.1
ALA-bPEI-GGS	2.163	70.44	+5.9

[a] Hydrodynamic size measured by DLS and reported as the number average. [b] Hydrodynamic sized measured by DLS and reported as the intensity average.

2.4.2 ALA release from bPEI-GGS

ALA has to be released from the NPs and converted to PpIX for ALA-RDT. Therefore, the release of ALA from NPs was investigated in a PBS buffer at acidic and physiological pH at 37 °C. ALA release was faster at pH 5.5. In the third hour of the study, the release of ALA from NPs reached 90 and 60 % at pH 5.5 and 7, respectively (Figure 2.1E). The protonation of carboxylic acids at acidic pH reduces the electrostatic interactions between the cationic GGS and ALA, leading to increased ALA release. Similar release trends were also reported in the literature [135, 161]. Faster release in the acidic microenvironment of the tumors is preferred for improved tumor accumulation and improved PpIX formation. The slower release of ALA at the physiological pH is also desired to protect the drug in circulation until it reaches the target.

2.4.3 GGS as a radiosensitizer

The potential of these NPs in RT and RDT was investigated first by the detection of ROS production under X-ray irradiation of the aqueous suspension of NPs using DCFH-DA dye. ALA-bPEI-GGS solutions were tested along with free ALA for comparison. All test samples were subjected to 2 Gy X-ray irradiation (Figure 2.1E). As expected, no significant ROS generation was observed in ALA solutions since ALA is a prodrug; it should be metabolized by viable cells and converted into PpIX during heme biosynthesis to act as a radiosensitizer or photosensitizer [162]. On the other hand, a significant amount of ROS generation with increasing concentrations of bPEI-GGS and ALA-bPEI-GGS was observed. Since ALA is not a photo/radiosensitizer, ROS generation in the aqueous solutions of these NPs originates from the radiosensitization of bPEI-GGS only. Hence, there is no significant difference in the ROS produced by ALA-bPEI-GGS and bPEI-

GGS.

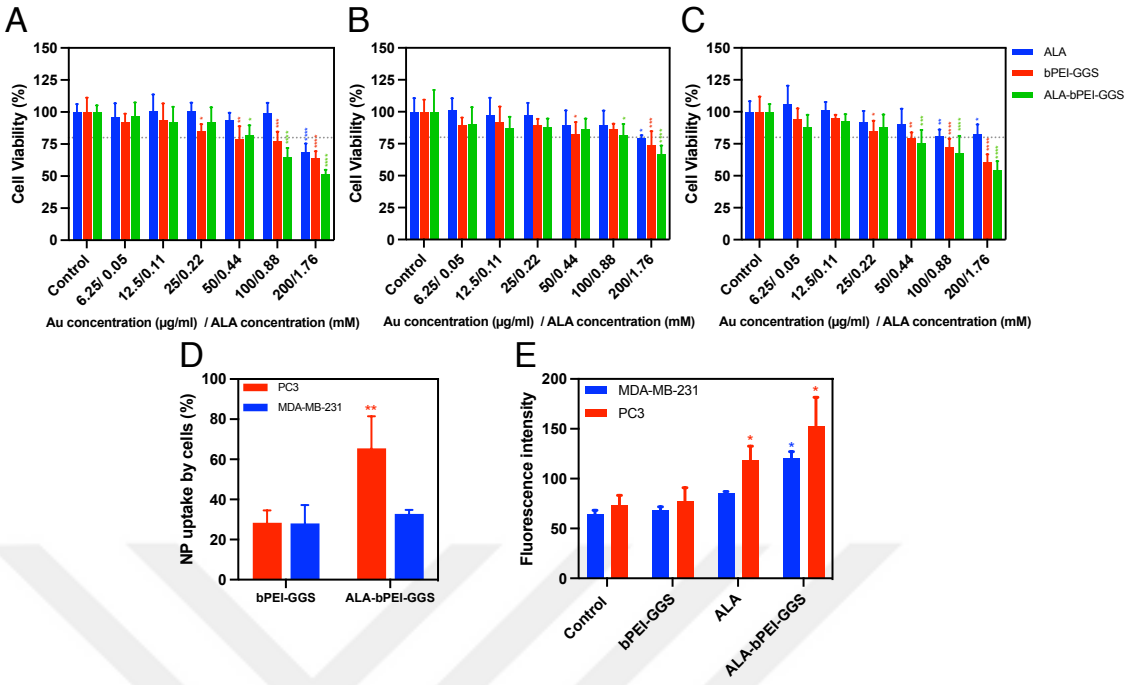

Figure 2.2 Viability of A) PC3, B) MDA-MB-231, and C) L929 cells treated with test materials at 6.25−200 µg Au/mL after 24 h of incubation determined by the MTT assay (n= 5). D) Intracellular quantification of NPs in PC3 and MDA-MB-231 cells after 24 hours incubation (Au concentration (µg/ml)/ALA concentration (mM): 25/0.22). E) Intracellular PpIX formation in PC3 and MDA-MB-231 cells after 24 h of incubation with free ALA or NPs (Au concentration (µg/ml)/ALA concentration (mM): 25/0.22, PpIX: λex/λem = 420/635 nm). (0.0332 (*), 0.0021 (**), 0.002 (***), <0.001 (****)).

2.4.4 In vitro cytotoxicity evaluation

Dose-dependent viability of PC3, MDA-MB-231, and L929 cells treated with bPEI-GGS, ALA, and ALA-bPEI-GGS was determined with MTT assay after 24 h incubation of the agents with the cells. Cells were treated with bPEI-GGS between 6.25 and 200 µg Au/ mL and free ALA between 0.05 and 1.76 mM concentrations, equivalent to the ALA content of ALA-bPEI-GGS. Considering viability above 80% as non-toxic based on ISO 10993-5, neither the NPs nor free ALA had significant toxicity between 6.25 and 25 µg Au/ mL concentration on these cell lines (Figure 2.2A-C). Dose-dependent significant cytotoxicity started at 50 µg Au/mL for NPs and at 0.88 mM for free ALA in healthy L929 but at 1.76 mM for the cancer cell lines. Cellular viability of PC3 and L929 decreased to 55-60% and MDA-MB-231 cells to 75-65% at the highest dose of bPEI-GGS and ALA-bPEI-GGS (200 µg Au/mL or 1.76 mM ALA), respectively.

2.4.5 Cellular Uptake

The internalization of NPs by PC3 and MDA-MB-231 cells was quantitatively determined by the intracellular [Au] concentration using ICP-MS after 24 h incubation of NPs at 100 μg Au/ mL concentration. As expected, ALA loading to NPs increased their uptake by PC3 significantly over the MDA-MB-231 cell line due to overexpression of PEPT1 and PEPT2 in PC3 cells [157, 158]. The uptake of NPs increased from 28 to 65% when loaded with ALA in PC3 but remained relatively the same (29% to 31%) in the case of the MDA-MB-231 cell line (Figure 2.2D).

2.4.6 In Vitro PpIX Generation

Generation of PpIX in PC3 and MDA-MB-231 cells was studied after 24 h incubation of the agents to allow internalization, release of ALA from NPs, and conversion of ALA to PpIX. No PpIX was detected with the bPEI-GGS treated cells, as expected. More PpIX in PC3 compared to MDA-MB-231 cells was detected for both free ALA and ALA-bPEI-GGS, again supporting selective uptake of ALA by PC3 cells. Yet, in both cell lines, more PpIX was produced if ALA was delivered with NPs. The PpIX fluorescence intensity was 1.5 and 1.4 times stronger in ALA-bPEI-GGS treated cells compared to ALA-treated cells for PC3 and MDA-MB-231, suggesting improved cellular internalization of ALA with the aid of NPs (Figure 2.2E).

2.4.7 In Vitro RT and RDT

The utility of GGS NPs as a radiosensitizer and the potential of ALA-GGS for RT/RDT were tested in vitro at different radiation doses between 0.5-4 Gy at a fixed NP dose of 25 μg Au/mL GGS or 0.22 mM ALA, confirmed non-toxic in the absence of X-Ray irradiation (Figure 2.1A-C). No loss in viability of cells exposed to 0.5-4 Gy irradiation confirmed the safety of these doses in the absence of a radiosensitizer (Figure 2.2A, B). Radiotoxicity in PC3 cells treated with free ALA was observed at and above 2 Gy with about 20% loss in viability. On the other hand, bPEI-GGS treated PC3 cells exhibited a dose-dependent loss in viability: about 50% between 0.5-2 Gy and 36% at 4 Gy. Notably, cells treated with ALA-bPEI-GGS showed a more pronounced radiotoxicity, decreasing the viability by 80-90% between 0.5-2 Gy and by 95% at 4 Gy, indicating nearly complete cell death at 4 Gy.

For MDA-MB-231 cells, ALA treatment alone had no significant effect on cell viability at any of the tested X-ray doses, which is in agreement with poor PpIX formation compared to PC3 cells (Figure 2.1E). Radiosensitization with bPEI-GGS reduced cell viability to 54-70% with no strong trend. Treatment with ALA-bPEI-GGS resulted in a significant improvement in radiotoxicity and dropped the viability of cells to about 17-29%.

These results highlight the potential of GGS as a radiosensitizer and the advantage of ALA-GGS in improving radiotoxicity at otherwise safe radiation doses. Higher internalization of ALA and hence ALA-GGS also come out as a strategy for improved radiotherapy for PEPT1/PEPT2 overexpressing cancer cell lines.

Dose-dependent cytotoxicity of the agents was studied at the lowest radiation dose, 0.5 Gy. Cells were incubated with NPs between 12.5–37.5 μg Au/mL concentrations or with free ALA between 0.11–0.33 mM, corresponding to the ALA load of the NPs. Free ALA at the studied doses did not cause radiotoxicity in MDA-MB-231 cells, but the viability of ALA-targeted PC3 cells dropped to 75% at 0.33 mM ALA (Figure 2.3C, D). On the other hand, bPEI-GGS showed a strong radiosensitization and increasing toxicity with increasing NP dose at and above 25 μg Au μg/mL concentration, reaching 24% and 32% viability at 37.5 Au μg/mL in PC3 and MDA-MB-231 cells, respectively.

ALA loading improved the radiotoxicity of NPs further, causing a significant reduction in viability even at the low agent doses, 12.5 μg Au/mL and 0.05 mM ALA, which was otherwise not toxic when introduced to cells alone. Cytotoxicity was improved with the dose of the ALA-GGS, which ended up with only 4 and 18% viability for PC3 and MDA-MB-231 at 37.5 μg Au/ml and 0.33 mM ALA. Higher radiotoxicity in PC3 than MDA-MB-231 agrees with better internalization of ALA and ALA-GGS by PC3 (Figure 2.2D-E).

The maximized therapeutic efficacy achieved here with a single 0.5 Gy irradiation with the use of ALA-loaded NPs is particularly significant for advancing safer, more targeted cancer therapies [163, 164].

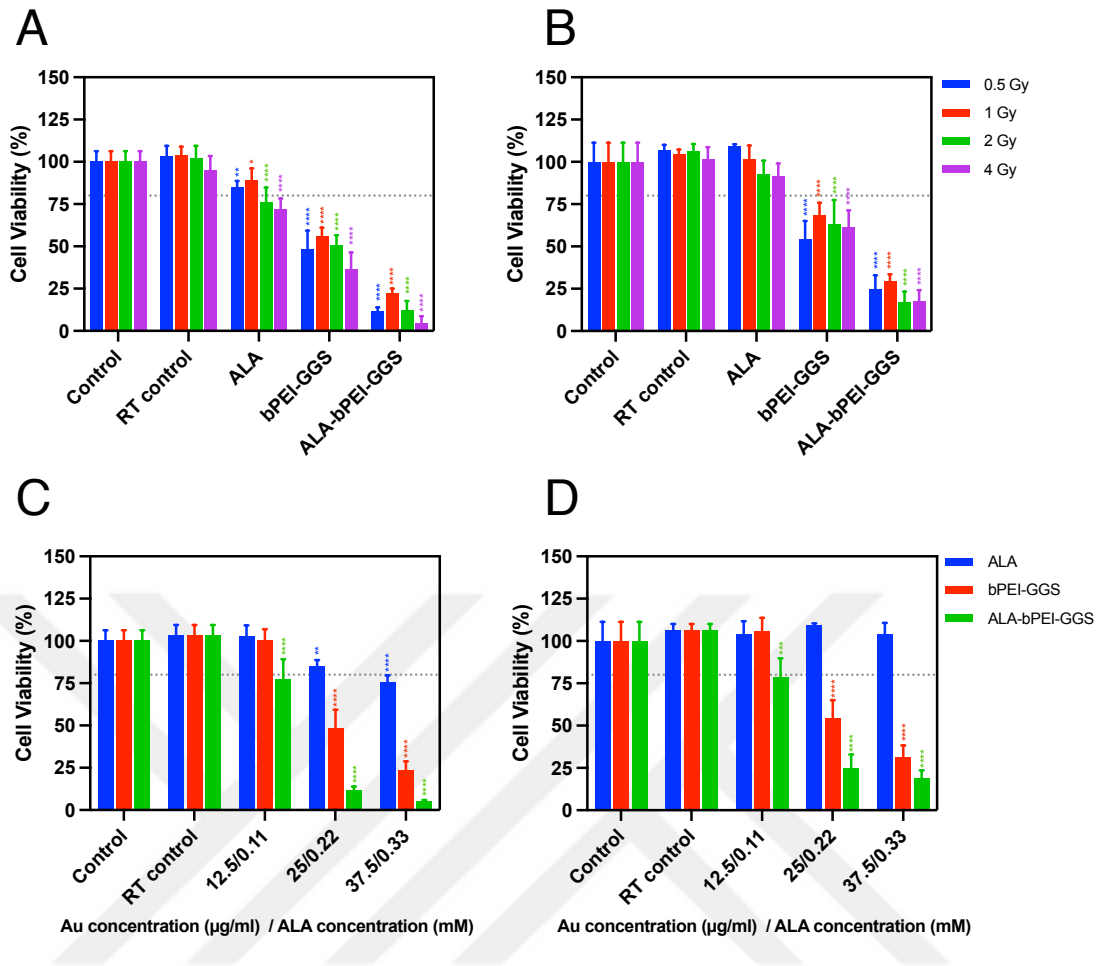

Figure 2.3 Dose-dependent viability of (A) PC3 and (B) MDA-MB-231 cells treated with free ALA and NPs exposed to 0.5 Gy irradiation. Radiation dose-dependent viability of (C) PC3 and (D) MDA-MB-231 after 24 hours of incubation with free ALA and NPs (Au concentration (µg/ml)/ALA concentration (mM): 25/0.22). Data expressed as mean ± S.D. (n = 5). (0.0332 (*), 0.0021 (**), 0.002 (***), <0.001 (****)).

Loss of cell viability was confirmed as cell death with live/dead assay using Calcein-AM/ Ethidium homodimer-1 staining (Figure 2.4). The study was performed for both cell lines treated with bPEI-GGS, ALA, and ALA-bPEI-GGS with and without 0.5 Gy X-ray irradiation. No dead cells were observed in test groups without X-ray irradiation. Similarly, no dead cells were observed when irradiated in the absence of test materials, indicating the safety of 0.5 Gy irradiation. A remarkable number of dead cells (red) and a decrease in the confluency were observed for bPEI-GGS treated and X-ray irradiated tumor cells. This shows that GGS is a promising and highly effective radiosensitizer, even at 0.5 Gy radiation, minimizing the off-target toxicity while maximizing the cell death at the target. An increasing number of dead cells with almost complete cell death for the two cell lines were observed as a result of a combination of

radiosensitizers via ALA-bPEI-GGS at such low doses of ALA, NP, and the irradiation dose.

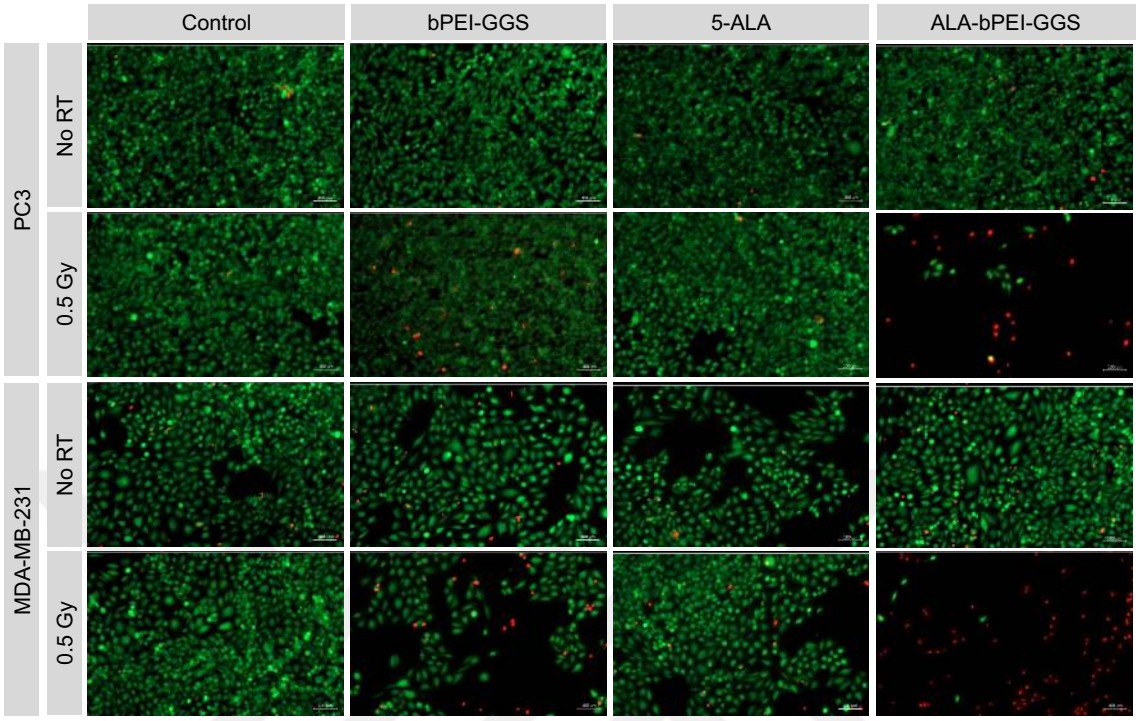

Figure 2.4 Live/dead staining images of PC3 and MDA-MB-231 cells upon no irradiation and 0.5 Gy irradiation after 24 hours of incubation with free ALA and NPs (Au concentration (μg/ml)/ALA concentration (mM): 25/0.22).

The cellular RDT efficacy was assessed using the cell colony formation assay, where we demonstrated the lethal effects on the cells with decreasing colonies. The study was performed at the same concentration and incubation time with Live/Dead assay. No change in the number of colonies was observed for the groups without irradiation compared to their control (Figure 2.5A, B). Here, we noticed that the surviving fraction decreases with free ALA-treated PC3 cells and bPEI-GGS-treated MDA-MB-231 cells. The increased accumulation of ALA in PC3 cells significantly improves the effect of RDT. Further, considering viability and colony formation assays, we can conclude that MDA-MB-231 cells are more sensitive to GGS radiosensitization. For both cell lines, RDT with ALA-bPEI-GGS prevents colony formation, showing the effectiveness of the therapy.

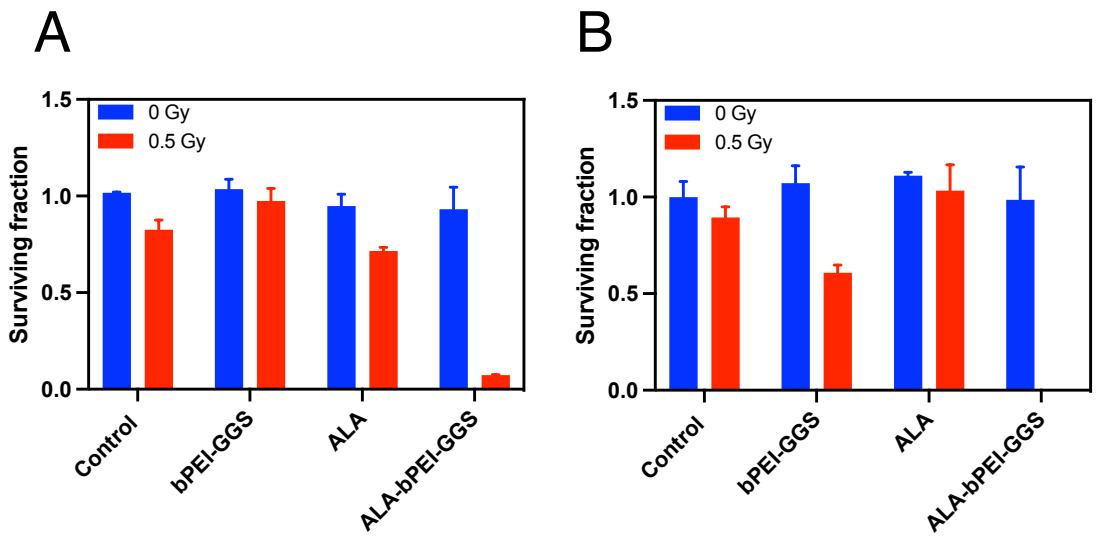

Figure 2.5 Surviving fraction of (A) PC3, (B) MDA-MB-231 cells upon no irradiation and 0.5 Gy irradiation after 24 hours of incubation with free ALA and NPs (Au concentration (µg/ml)/ALA concentration (mM): 12.5/0.22).

Here, we would like to emphasize that our radiodynamic therapy approach, using single, low-dose 0.5 Gy irradiation with 25 µg Au/mL NP and 0.22 mM ALA, significantly reduced the therapeutic dose of ALA and the required X-ray dose compared to previous studies. Yamamoto et al. demonstrated the radiosensitizing effect of 1 mM ALA with single X-ray irradiation on 9L gliosarcoma and C6 glioma cells, achieving significant radiosensitivity only in 9L cells with doses above 6 Gy compared to X-ray-treated control cells [165]. Similarly, Miyake et al. treated PC3 cells with 100 µM ALA and 2.5 Gy X-ray, reporting a reduction in colony numbers to below 20% of the control [139]. Han et al. designed a targeted nanoplatform incorporating doxorubicin and 1 mM ALA with polyaspartamide nanoparticles, achieving approximately 30% cell viability in H1299 lung carcinoma cells after 5 Gy irradiation [166]. In comparison, our approach achieved superior radiosensitization with significantly lower ALA and X-ray doses, demonstrating its potential as a more efficient and safer alternative for cancer therapy.

2.4.8 Intracellular ROS Generation

The in vitro ROS generation in both dark and 0.5 Gy X-ray-irradiated cells was assessed using DCFH-DA after a 24-hour incubation with NPs in PC3 and MDA-MB-231 cells (Figure 2.6A). No ROS production was observed in cells treated with NPs or ALA alone without X-ray irradiation. However, upon X-ray irradiation, both cell types

treated with NPs and ALA exhibited significant ROS production. Notably, MDA-MB-231 cells generated higher levels of ROS than PC3 cells following bPEI-GGS treatment and irradiation (Figure 2.6B). This elevated ROS generation in MDA-MB-231 cells correlates with the observed reduction in colony formation (Figure S4), highlighting the strong radiosensitization effect of bPEI-GGS. Furthermore, cells treated with ALA-bPEI-GGS demonstrated a substantial increase in ROS production, attributed to the synergistic effect of GGS-mediated radiosensitization and PpIX excitation, highlighting the enhanced therapeutic potential of the approach.

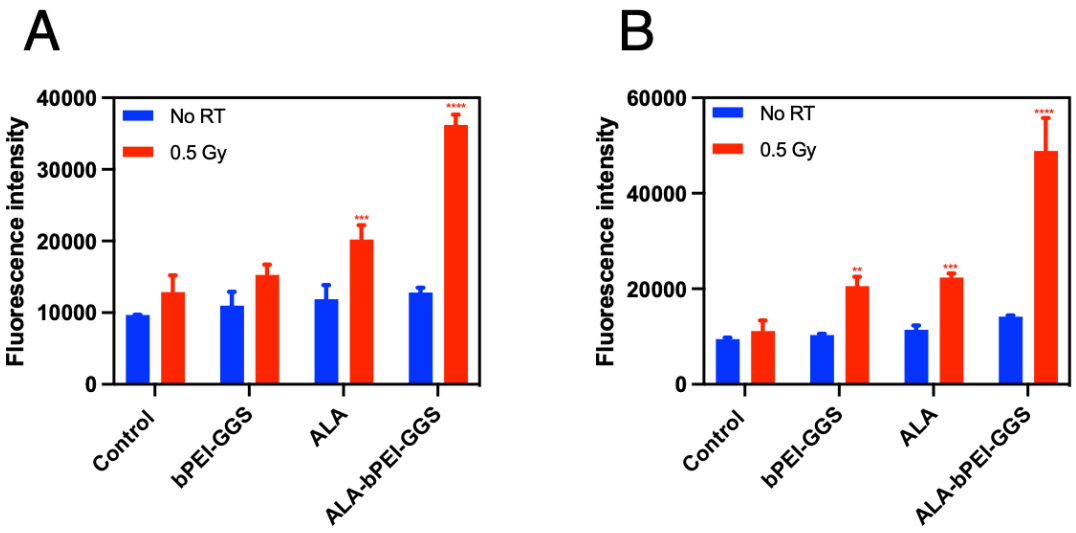

Figure 2.6 ROS production in (A) PC3 and (B) MDA-MB-231 cells upon no irradiation and 0.5 Gy irradiation after 24 hours of incubation with free ALA and NPs. The data are expressed as mean ± S.D. (n = 3). (0.0332 (*), 0.0021 (**), 0.002 (***), <0.001 (****)).

2.4.9 Characterization of cell death following radio sensitization with nanoparticles

In the previous part, we showed that the combination of ALA with bPEI-GGS successfully sensitized both PC3 and MDA-MB-231 cells against low-dose X-ray radiation. Of note, the elevation of cell death was observed more prominently in PC3 cells due to the targeting effect of ALA. In order to evaluate cell death mechanisms upon radiosensitization, we treated PC3 and MDA-MB-231 cells with ALA, bPEI-GGS, or ALA-bPEI-GGS nanoparticles and performed immunoblotting. The Caspase cascade occurs following apoptotic stimuli and results in the cleavage and activation of executioner Caspases, e.g., Caspase-3. Then activated or/else cleaved Caspase-3 further

cleaved its targets, including PARP, which is vital for the cell, eventually leading to cell death [167]. Under dark conditions, elevated PARP and Caspase-3 cleavage were shown in PC3 cells treated with bPEI-GGS NPs or ALA-bPEI-GGS compared to control and free ALA (Figure 2.7A). Notably, this effect was more prominent following the combination of low-dose radiation (Figure 4A). In MDA-MB-231 cells, there was no evident change in the cleaved PARP and Caspase-3 levels under dark conditions. Only cleaved PARP was observed to some extent in ALA and bPEI-GGS following the low-dose radiation (Figure 2.7B). However, in contrast to PC3, the ALA-bPEI-GGS with low-dose radiation did not cause any significant alteration in the level of both PARP and Caspase-3 cleavage in MDA-MB-231 cells (Figure 2.7B).

Accumulation of DNA damage without repair causes lethal lesions in cells [159]. Phosphorylation of Histone H2A.X (γ-H2A.X, p-H2A.X), a specific histone 2A variant, was shown to recognize specifically DNA damage, and its accumulation has been used as a marker for DNA damage [168]. Radiation is one of the leading causes of DNA damage. Hence, we check the level of phosphorylated H2A.X in our experimental setup. Our data revealed that following low-dose radiation, phosphorylated H2A.X increased with bPEI-GGS and ALA-bPEI-GGS nanoparticles in PC3 cells (Figure 2.7A). Under similar conditions, we did not monitor any alterations in the level of p-H2A.X in MDA-MB-231 cells (Figure 2.7B).

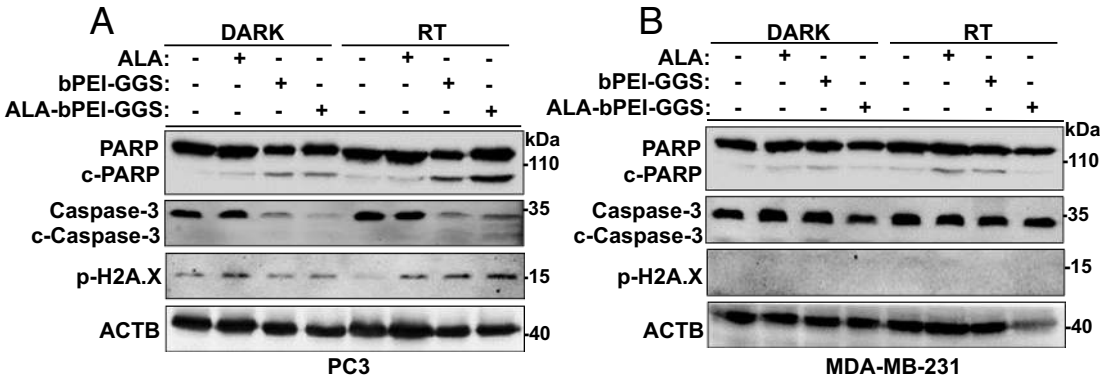

Figure 2.7 Characterization of cell death mechanisms in both cell lines. Immunoblotting of PARP, Caspase-3, and p-H2A.X was evaluated following low-dose radiation alone with ALA, bPEI-GGS, or their combination. Nanoparticle treatments were applied to (A) PC3 and (B) MDA-MB-231 cells for 24h, media replaced, and then cells were subjected to low dose radiation for another 24h (Au concentration (μg/ml)/ALA concentration (mM): 25/0.22). ACTB, β-actin protein, was used as a loading control. DARK represents no radiation, and RT represents low-dose radiation (0.5 Gy). c-PARP: Cleaved PARP, c-Caspase-3: Cleaved Caspase-3.

The autophagic activity results in the degradation of cellular demise upon stimuli to maintain cellular homeostasis. In addition, autophagy is considered one of the primary cell death mechanisms under certain conditions [169]. Of note, following therapy, including radiation, elevation of autophagy might be responsible for the therapy resistance and delayed cell death [170]. Upon autophagic stimuli, LC3-I is cleaved, and after binding with phosphatidylethanolamine (PE), it converts to LC3-II and is involved in the autophagosome membrane. Conversion of LC3-I to LC3-II is one of the markers of autophagic activity in cells [171]. p62 is one of the receptors of autophagy, and its degradation is associated with autophagic activity in cells [172]. Therefore, to identify autophagic status in our system, alterations in the level of autophagy markers were analyzed by immunoblotting. Under dark conditions, elevated LC3-I/-II conversion has been observed in bPEI-GGS and ALA-bPEI-GGS nanoparticles in PC3 cells. Surprisingly, the elevation of the LC3-I/-II conversion was more prominent with ALA-bPEI-GGS nanoparticles in low-dose radiation conditions (Figure 2.8A).

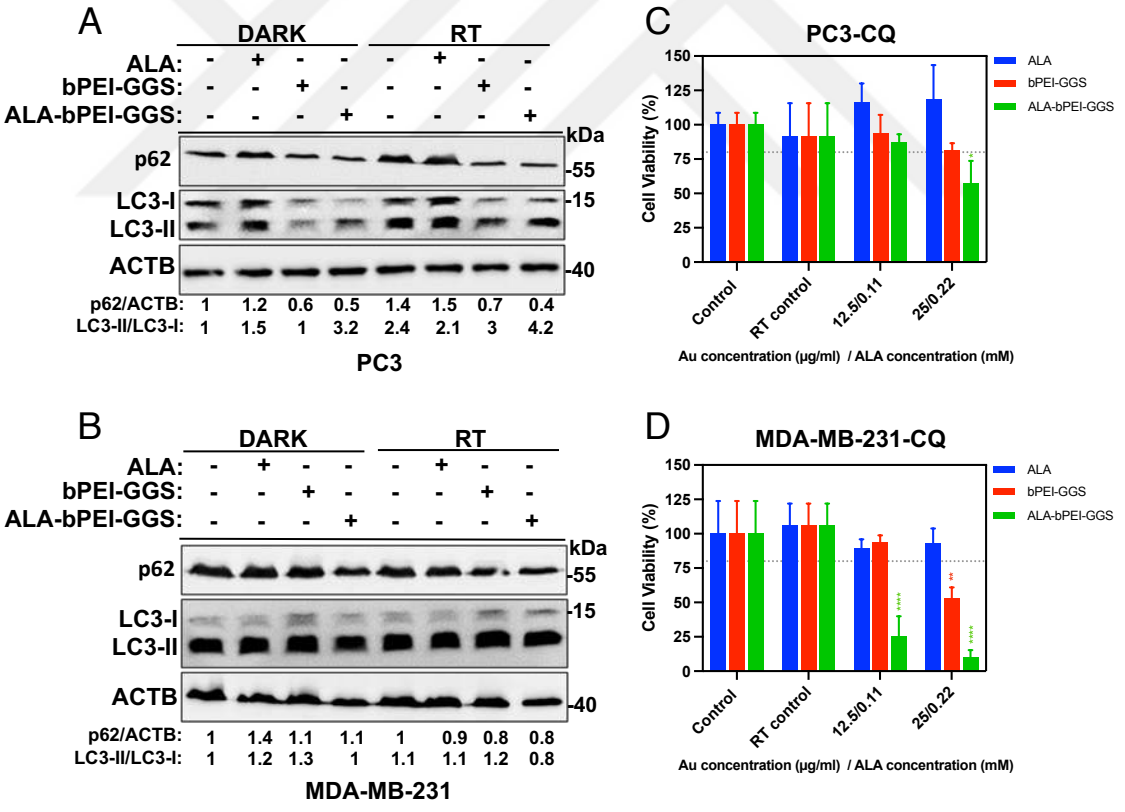

Figure 2.8 Role of autophagy in cell death decision in both cell lines. Immunoblotting of p62 and LC3 was evaluated following low-dose radiation alone with ALA, bPEI-GGS, or their combination. Nanoparticle treatments were applied to (A) PC3 and (B) MDA-MB-231 cells for 24h, media replaced, and then cells were subjected to low dose radiation for another 24h (Au concentration (µg/ml)/ALA concentration (mM): 25/0.22). Cell viability analyses were utilized following combination with Chloroquine (CQ, 10µM,

24h). Graph representing (C) PC3 and (D) MDA-MB-231 cell viability following treatments. ACTB, β-actin protein, was used as a loading control. DARK represents no radiation; RT represents low-dose radiation (0.5 Gy) condition. Band intensity of immunoblots LC3-II/-I, p62/ACTB were analyzed by ImageJ. (0.0332 (*), 0.0021 (**), 0.002 (***), <0.001 (****)).

In addition, neither different nanoparticles nor radiation combination resulted in some change in LC3-I/-II conversion in MDA-MB-231 cells (Figure 2.8B). We observed that basal autophagy was higher in MDA-MB-231 cells compared to PC3 cells (Figure 2.8B). We also further evaluated the correlation of cell death with autophagy status. Therefore, we combined our treatment setup with Chloroquine (CQ), an autophagy inhibitor, and measured cell viability in both cell lines. CQ had no striking effect on dark toxicity in both cell lines (Figure 2.9A, B). According to our analyses, CQ significantly increased cell viability in PC3 cells against all treatment conditions combined with low-dose radiation, especially in the ALA-bPEI-GGS nanoparticle condition (Figure 2.8C). A similar approach has been utilized for MDA-MB-231 cells, and no significant alteration in cell viability has been observed compared to PC3 cells (Figure 2.8D). Therefore, our data revealed that autophagy might occur in the decision of cell death in PC3 cells, yet it might not be involved in the decision in MDA-MB-231 cells under low-dose radiation. To support this, we created CRISPR/Cas9 *ATG5* knockout (ATG5KO) PC3 cells, and similar experiments were performed using them.

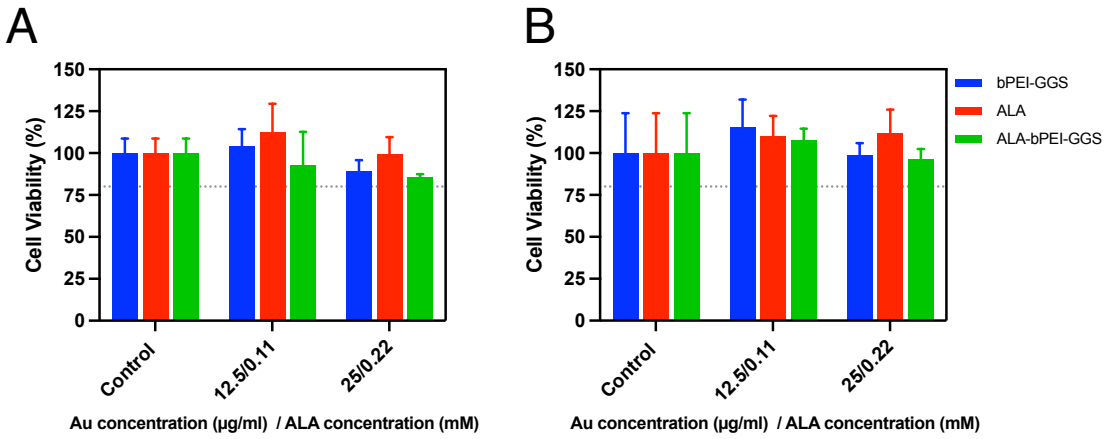

Figure 2.9 Effect of CQ under dark conditions on cell viability. Dark toxicity was assessed by following nanoparticle treatments on both cell lines for 24h, and media was replaced. Then, cells were kept for another 24 hours before protein isolation (Au concentration (µg/ml)/ALA concentration (mM): 25/0.22). Cell viability analyses were utilized following a combination with Chloroquine (CQ, 10µM, 24h)—graph representing (A) PC3 and (B) MDA-MB-231 cell viability following treatments.

We performed immunoblotting to confirm the loss of *ATG5* and consequent autophagic activity and checked ATG5, LC3, and p62 levels. ATG5 protein was abolished, p62 protein was accumulated, and LC3-I/-II turnover was blocked compared to wild-type (WT) cells upon loss of autophagy in ATG5KO PC3 cells (Figure 2.10A). Of note, starvation (STV) was used to induce autophagy under this condition. Although wild-type PC3 cells showed elevated autophagy with loss of p62 and increased LC3-I/-II turnover, ATG5KO cells were irresponsive against starvation, supporting the loss of autophagy in this context (Figure 2.10A). We also performed immunofluorescent analyses to validate these observations further. In line with our previous findings, LC3 positive dots were diminished, and p62 aggregates were augmented in ATG5KO PC3 cells (Figure 2.11A-C). Data here supported the successful creation of *ATG5* null PC3 cells. Lastly, we performed a cell viability assay with autophagy null PC3 cells, and in line with previous CQ data, loss of *ATG5* and autophagic activity totally abrogated cell death in ATG5KO PC3 cells upon low radiation with the combination of nanoparticles (Figure 2.10B).

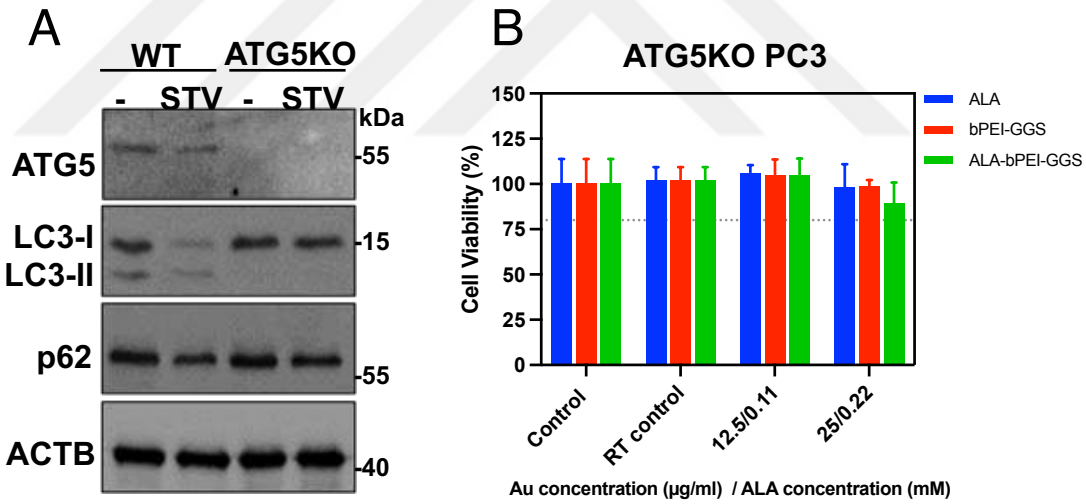

Figure 2.10 Autophagy is indispensable for PC3 cell death**.** (A) Immunoblotting of p62, ATG5, and LC3 was evaluated under basal or starvation (STV) induced conditions in ATG5KO PC3 cells compared to WT PC3 cells. ATG5KO PC3 cells were treated with bPEI-GGS, ALA, and ALA-bPEI-GGS for 24h, media replaced, and cells were subjected to low dose radiation for another 24h (Au concentration (μg/ml)/ALA concentration (mM):25/0.22). (B) Graph representing ATG5KO PC3 cell viability following treatments. ACTB, β-actin protein, was used as a loading control. DARK represents no radiation, and RT represents low-dose radiation (0.5 Gy). EBSS solution was used to starve the cells (STV, EBSS 4h).

Overall, our data revealed that not all nanoparticles but specifically a combination of ALA-bPEI-GGS with low-dose radiation prominently increased apoptotic cell death with elevated DNA damage in PC3 cells. In addition, autophagy is indispensable in the cell death decision of PC3 cells in this context. However, in MDA-MB-231 cells, although there was some increase in cleavage of PARP, it was not elevated upon low-dose radiation combination. Our data suggest that this might be due to resistance to DNA damage and lack of ALA-dependent targeting but not high autophagic activity in our experimental setup.

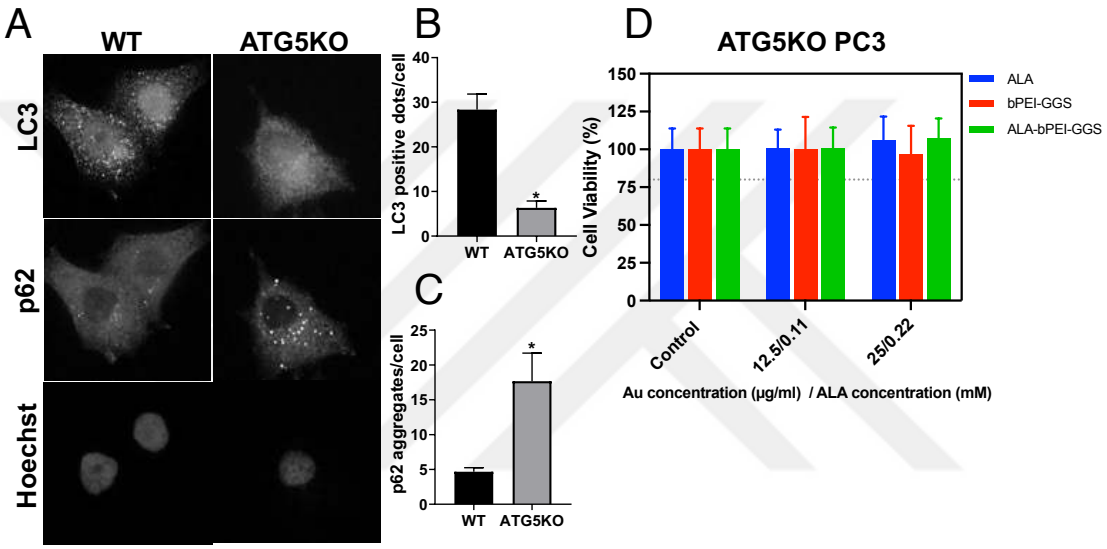

Figure 2.11 Immunofluorescence staining was performed to evaluate LC3 dot and p62 aggregate formation. (A) WT PC3 and ATG5KO PC3 cells were seeded on cover slides and let grow for 24h. Cells were fixed, and indirect immunofluorescent analysis was utilized. Alexa-488 (green) and Alexa-568 (red) were used as secondary antibodies against rabbit anti-LC3 and mouse anti-p62, respectively. Cells were visualized under a fluorescent microscope at 63× magnification. Nuclei were stained with Hoechst (blue). (B) Graph representing LC3 positive dots/cell calculated by counting 50 cells in each condition. (C) Graph representing p62 aggregates/cell that were calculated by counting 50 cells in each condition (mean ± S.D. of independent experiments, n = 3, *, $p < 0.05$). (D) Dark toxicity was assessed by following nanoparticle treatments on ATG5KO PC3 cells for 24h, and the media was replaced. Then, cells were kept for another 24 hours before protein isolation (Au concentration (µg/ml)/ALA concentration (mM): 25/0.22)—graph representing ATG5KO PC3 cell viability following treatments.

2.5 Conclusion

This study demonstrates the potential of ALA-loaded, branched polyethyleneimine-coated gold-gold sulfide nanoparticles as effective radiosensitizers in radiodynamic

therapy against PC3 and MDA-MB-231 cancer cell lines. The ALA-bPEI-GGS nanoparticles exhibited increased stability, bioavailability, and a controlled release of ALA, facilitating enhanced intracellular PpIX generation and efficient ROS production upon low-dose X-ray irradiation. ALA's targeting effect on prostate cancer cells contributes to its higher efficacy in PC3 cells than MDA-MB-231 cells. In PC3 cells, the treatment significantly increased apoptotic markers (cleaved PARP and Caspase-3), DNA damage (phosphorylated H2A.X), and autophagy (LC3-I/-II conversion). Conversely, MDA-MB-231 cells demonstrated minimal autophagic and apoptotic alterations. Chloroquine or ATG5 knockout inhibition of autophagy suppressed cell death in PC3 cells, as expected, to validate the fact that autophagy is a determining factor in how they respond to treatment. MDA-MB-231 cells, though, were resistant, most likely because they possess intrinsic DNA damage tolerance and are not subject to ALA-mediated targeting. Overall, ALA-bPEI-GGS nanoparticles, combined with low-dose radiation, are of great promise for enhancing the efficacy of RDT, especially against deeply seated and radioresistant tumors, and are a possible alternative to targeted cancer therapy.

Chapter 3: Targeted Gold-Gold Sulfide Nanoparticles for Photoacoustic Imaging and Enhanced PTT/RT Combination Therapy

3.1 Abstract

Advancements in nanomedicine have revolutionized cancer treatment by bringing diagnostic and therapeutic modalities into single multifunctional platforms. Gold nanoparticles are promising tools for their unique properties, high photothermal conversion efficiency, and radiosensitization capabilities. Gold-gold sulfide nanoparticles (GGS) are new-generation GNPs that offer strong near-infrared (NIR) absorption. In this study, we used GGS as a theranostic tool for photoacoustic imaging (PAI), photothermal therapy (PTT), and radiotherapy (RT). Multifunctional 3-mercaptopropionic acid-coated GGS (3MPA-GGS) nanoparticles were functionalized with folic acid (FA) to selectively target folate receptor-positive (FR+) cancer cells, enhancing therapeutic specificity and efficacy. FA-3MPA-GGS exhibited strong NIR absorption, photothermal stability, and high light-to-heat conversion efficiency under 808 nm irradiation. In vitro studies demonstrated increased nanoparticle uptake, enhanced ROS generation, and significant reductions in cell viability, particularly in FR+ cell lines (HeLa and MDA-MB-231), compared to folate receptor-negative cells (A549). Combining PTT and RT using FA-3MPA-GGS resulted in synergistic therapeutic effects, reducing the required treatment dose and minimizing off-target effects. In summary, FA-functionalized GGS nanoparticles are promising theranostic tools for targeted cancer therapy, combining imaging-guided precision with enhanced dual-modality treatment.

3.2 Introduction

Theranostic nanoparticles offer innovative solutions for cancer treatment. Their bimodal functionality offers real-time feedback of the treatment process as well as targeted delivery of therapy. Targeting molecules, drugs, and photosensitizers functionalized on theranostic nanoparticles offer localized and effective treatments with reduced off-target effects by reducing the therapeutic dose needed. This minimizes therapeutic agent exposure, reduces side effects, and presents a highly individualized treatment method that can be tailored to specific patients.

Gold nanoparticles (GNPs) stand out among theranostic nanoparticles' exceptional properties, including ease of surface functionalization [173, 174], tunable surface plasmon resonance [147, 175], high light-to-heat conversion efficiency [23, 176], and radiosensitization [36, 177] capabilities. A novel class of GNPs, gold-gold sulfide nanoparticles (GGS), attracts significant attention for their strong near-infrared (NIR) absorption [178, 179]. This property is particularly critical for biomedical applications. NIR light enables deeper tissue penetration, reduces tissue autofluorescence, and enhances imaging resolution, thus facilitating the visualization of deeper tumors and improving therapeutic outcomes.

Photothermal therapy (PTT) is a light-driven cancer treatment modality that converts absorbed light energy into heat, inducing localized temperature increases that effectively ablate tumor cells [180]. PTT offers several advantages, including strong anticancer effects, high precision, minimal side effects on healthy tissues, and reduced infrastructure costs. Nanoparticles with NIR absorption, such as GGS, are ideal photothermal agents, as they rapidly generate intense localized heat upon excitation with NIR light. This localized heating triggers various biological effects, including cell membrane disruption, protein denaturation, and DNA damage, leading to effective cancer cell destruction [181, 182].

While PTT offers a localized and precise approach to cancer ablation, other treatment modalities can further enhance its efficacy. Radiotherapy (RT) is a cancer treatment technique commonly used in clinics due to its ability to achieve curative or palliative outcomes in over half of all cancer patients [183]. Ionizing radiation such as X-rays has profound penetration into tissues, and hence RT is very effective for treating deeply seated tumors. Conventional RT, however, is not cell-type specific and often induces undesired damage to normal tissues. Nanoparticle-mediated radiosensitization is an appealing strategy by enhancing the radiotoxicity of cancer cells with little effect on normal tissues. High-Z metallic nanoparticles act as effective radiosensitizers due to their unique interaction with ionizing radiation, which produces secondary electrons and reactive oxygen species (ROS) [38, 184, 185]. These interactions induce DNA damage and sensitize cancer cells to radiation, significantly improving therapeutic outcomes even at lower radiation doses [186].

Beyond their therapeutic applications in PTT and RT, nanoparticles like GGS also offer significant advantages in cancer imaging. Besides photothermal effects, strong NIR absorption of these nanoparticles enhances their use as contrast agents in advanced

imaging techniques such as photoacoustic imaging (PAI). PAI is an emerging hybrid imaging modality that combines the high contrast of optical imaging with the deep penetration of ultrasound. Nanoparticles with strong NIR absorption, such as GGS, are particularly valuable for PAI due to their reduced scattering and increased penetration depth in the NIR region, providing high-resolution visualization of deeply seated tissues that are otherwise challenging to image [187, 188]. Our previous studies demonstrated the potential of GGS as a contrast agent for PAI [116].

In this study, we designed multifunctional 3-mercaptopropionic acid-coated gold-gold sulfide nanoparticles (3MPA-GGS) conjugated with folic acid (FA) for PAI-guided enhanced PTT and RT in folate receptor-positive (FR+) cancer cells. Folic acid conjugation facilitates selective targeting and improves treatment specificity. The strong NIR absorption of FA-3MPA-GGS supports effective PAI and PTT, while the gold core enhances radiosensitization for RT. In vitro studies on FR+ (HeLa and MDA-MB-231) and FR– (A549) cell lines demonstrated enhanced therapeutic efficacy and reduced IC50 values for FR+ cells. These findings were further corroborated by evidence of high nanoparticle internalization (tracked using PAI), increased LDH release, and elevated ROS generation in targeted cells.

3.3 Materials and Methods

3.3.1 Materials

Gold (III) chloride trihydrate ($HAuCl_4 \cdot 3H_2O$) and sodium thiosulfate pentahydrate ($Na_2S_2O_3 \cdot 5H_2O$) were obtained from Sigma-Aldrich. 3-Mercaptopropionic acid (3MPA) was sourced from Polysciences, while methoxy poly(ethylene glycol) thiol (mPEG-SH, 2 kDa average molecular weight) was supplied by Laysan Bio, Inc. Folic acid was purchased from Bio Basic. Poly(ethylene glycol) diamine (PEG-diamine, 2 kDa average molecular weight) was also acquired from Sigma-Aldrich. Vivaspin 20 centrifugal filters (10 kDa) were supplied by Sartorius, Germany. Ultra-pure water (18.2 MΩ) from Rephile Bioscience and Technology, China, was used in all experiments.

Roswell Park Memorial Institute 1640 (RPMI) medium, Dulbecco's Modified Eagle Medium (DMEM), fetal bovine serum, trypsin-EDTA, L-glutamine, and penicillin-streptomycin were obtained from Diagnovum. Dimethyl sulfoxide (DMSO) was

purchased from Sigma-Aldrich. Phosphate-buffered saline (PBS) tablets and thiazolyl blue tetrazolium bromide (MTT) were supplied by Biomatik. Paraformaldehyde solution (4% in PBS) was sourced from Santa Cruz Biotechnology, Inc., USA. 96-well plates were acquired from Nest Biotechnology, and glass-bottom petri dishes were purchased from Cellvis. LDH cytotoxicity assay was purchased from Merck. LDH Cytotoxicity Assay Kit was obtained from Sigma Aldrich (MAK529).

3.3.2 Synthesis of 3MPA-GGS

3MPA-GGS was synthesized, as reported in our previous work [189]. Rapid addition of $6.6x10^{-3}$ mmol $Na_2S_2O_3$ solution to $8.55x10^{-3}$ mmol $HAuCl_4$ was done under vigorous stirring at 500 rpm at room temperature. Coating materials of 3MPA and mPEG-SH with mol ratios of 3MPA/mPEG/Au 9/1/1 were injected into the reaction solution at the 10^{th} minute of the reaction. The obtained colloidal solution was washed with DI water using 10 kDa centrifugal filters at the 30^{th} minute of the reaction. The nanoparticles were kept in the dark at 4 °C.

3.3.3 Conjugation of folic acid to 3MPA-GGS

Folic acid (FA) was conjugated to PEG diamine (2 kDa) via an EDC/sulfo-NHS amidation reaction. Briefly, 50 mg of FA was dissolved in water, and its carboxylic acid groups were activated using 0.227 mmol of EDC and sulfo-NHS for 30 minutes at pH 6. Following activation, 0.113 mmol of H2N-PEG-NH2 was added to the reaction mixture, which was stirred overnight at room temperature. The resulting FA-PEG-NH2 product was lyophilized and stored in the dark at -20 °C.

The carboxylic acid groups on 30 mg of 3MPA-GGS were activated using EDC/sulfo-NHS amidation. A total of 0.019 mmol of EDC and an equimolar amount of sulfo-NHS were added to the reaction mixture and stirred for 30 minutes at pH 6. Excess EDC and sulfo-NHS were removed by washing the nanoparticles with water using 10 kDa centrifugal filters. The pH of the solution was adjusted to 7–7.5 before adding 10 mg of FA-PEG-NH2. The mixture was allowed to react overnight at room temperature, targeting 5 mol% of the surface carboxylic acids for FA-PEG-NH2 conjugation. To quench unreacted activated carboxylic acid groups, 0.095 mmol of hydroxylamine was added to the reaction. The final product was washed with water using 10 kDa centrifugal filters to remove unbound reagents.

The amount of conjugated FA was determined by measuring the absorbance of the wash solution containing unreacted FA-PEG-NH_2 at 320 nm. The concentration of FA-PEG-NH_2 was calculated using a pre-determined calibration curve of absorbance as a function of FA-PEG-NH_2 concentration.

3.3.4 Characterization

The absorption spectrum of the NPs was measured by a Shimadzu UV-VIS-NIR spectrophotometer between 450 and 1200 nm. Malvern Zetasizer Nano ZS measured hydrodynamic sizes and zeta potentials. Particle sizes and shapes were confirmed with Hitachi 7800 TEM analysis. The Au content of NPs was determined using an Agilent 7700X ICP-MS (inductively coupled plasma-mass spectrometer). Samples were digested with hydrochloric acid and nitric acid (3:1 v/v).

3.3.5 PTT potential in solution

The PTT potential of 3MPA-GGS and FA-3MPA-GGS NPs was assessed in aqueous solutions at varying concentrations. A 0.75 mL solution of NPs at 50, 100, and 200 μg Au/mL concentrations was irradiated using a homemade, continuous-wave, Ti^{3+}: sapphire laser at 808 nm with an incident power of 215 mW. Time-dependent temperature increase (ΔT) was continuously monitored over 25 minutes using a thermocouple and an infrared camera (FLIR, model no. A325SC) simultaneously. To evaluate the photothermal stability and reproducibility, the NPs underwent three laser cycles of on/off irradiation under the same experimental conditions. The ability of the NPs to maintain their photothermal effect over consecutive irradiations was analyzed.

The light-to-heat conversion efficiency calculation of the NPs was optimized previously and determined by analyzing the temperature dynamics during laser irradiation [190]. The steady-state temperature distribution on the surface of the cuvette was recorded using a thermal camera. Key parameters, including temperature increase, incident laser power, and the solution mass, were incorporated into a linearized heat transfer model to calculate the conversion efficiencies.ROS generation in solution

To detect ROS generation, 10 μM DCFH-DA dye was added to 3MPA-GGS and FA-3MPA-GGS solutions at 6.75, 12.5, and 25 μg Au/mL concentrations. The samples were then irradiated with a 2 Gy dose of X-ray. Following irradiation, the fluorescence intensity

was measured using a microplate reader at excitation/emission wavelengths of 485/535 nm.

3.3.6 Cell culture

L929 healthy fibroblast, HeLa cervical cancer, MDA-MB-231 triple-negative breast cancer cells were cultured in DMEM, and A549 lung cancer cells were cultured in RPMI, medium supplemented with 10% fetal bovine serum, 2% L-glutamine (2 mM), and 1% penicillin-streptomycin at a 37 °C incubator with 5% CO_2 atmosphere. Cells were washed with PBS and trypsinized with 0.05% trypsin-EDTA before passage and seeding.

3.3.7 Cytotoxicity assay

The cytotoxicity of 3MPA-GGS and FA-3MPA-GGS nanoparticles (NPs) was evaluated using the MTT metabolic activity assay. NP solutions were sterilized using 0.2 μm sterile filters before use. L929, HeLa, MDA-MB-231, and A549 cells were seeded into 96-well plates at a density of 2.5×10^5 cells per well and incubated overnight. Following incubation, the culture medium was replaced with fresh medium, and NPs were added to the wells at concentrations ranging from 25 to 500 μg Au/mL for 24 and 48 hours. After the treatment period, the medium was removed, and a mixture of MTT reagent (5 mg/mL in PBS) and medium (1:3 volume ratio) was added to the wells. The plates were incubated for 4 hours at 37 °C to allow for the formation of formazan crystals, which indicate the metabolic activity of viable cells. The formazan crystals were dissolved by adding 200 μL of ethanol: DMSO (1:1 v/v) solution to each well. The absorbance of the resulting solution was measured at 570 nm using a Synergy H1 microplate reader (BioTek Instruments), with 650 nm used as a reference wavelength. Cell viability was calculated using the equation: Viability (%) = 100 x absorbance (treated) / absorbance (control) (n =5).

3.3.8 Cellular uptake

The cellular uptake of 3MPA-GGS and FA-3MPA-GGS NPs was quantitatively determined using ICP-MS analysis by measuring the Au content in NP-treated cells. HeLa, MDA-MB-231, and A549 cells were seeded in 6-well plates at a density of 2×10^5 cells per well in a complete medium and incubated for 24 hours at 37 °C with 5% CO_2. After incubation, the cells were treated with NPs at 100 μg Au/mL concentrations for 6

hours. To remove non-internalized particles, the cells were washed thoroughly with PBS and collected by trypsinization at room temperature after 20 minutes. The collected cells were then digested in aqua regia (hydrochloric acid: nitric acid, 3:1 v/v) at room temperature for one week. The Au content of the samples was quantified using ICP-MS analysis (n=3).

3.3.9 In vitro photoacoustic imaging

HeLa, MDA-MB-231, and A549 cells were seeded at a density of 2×10^5 cells per well in glass-bottom plates and incubated overnight. The following day, the culture medium was removed, and a fresh medium containing 3MPA-GGS or FA-3MPA-GGS at a concentration of 100 μg/mL was added to the wells. The cells were incubated for 6 hours at 37 °C. After incubation, the medium was aspirated, and the cells were washed three times with PBS to remove any unbound nanoparticles. The cells were then fixed with 4% paraformaldehyde solution for 20 minutes at room temperature. Following fixation, the paraformaldehyde solution was removed, and the cells were washed three times with PBS. Finally, PBS was added to the wells to prevent cell dehydration.

Photoacoustic images were captured using an optically resolved photoacoustic microscope (OR-PAM) equipped with two laser sources. The schematic of the experimental setup is in Figure S4. For imaging in the visible range, a 10 kHz nanosecond pulsed laser (Spectra-Physics, Explorer One) was used at a wavelength of 532 nm. For the near-infrared (NIR) range, a tunable gain-switched Ti: Sapphire laser operating at 800 nm was utilized. Cultured cells immersed in PBS medium were exposed to pulse energies of 0.07 μJ at 532 nm and 0.36 μJ at 800 nm, where both laser beams were focused through a 40× objective to achieve high-resolution cellular imaging. The back reflection from the objective lens was imaged onto a CCD camera (Thorlabs DCU224M-GL) to capture bright-field images of the scanned region. The emitted photo-acoustic signals were detected using a 5 MHz single-element ultrasonic transducer, which was amplified by 50 dB through a two-stage amplification system. To record the photo-acoustic signals coming from the cells, a custom MATLAB code simultaneously translated the motorized stages and recorded the emitted signals through a DAQ card (Gage Compuscope). Later, recorded signals were constructed to the scanned position values to form the photo-acoustic images.

3.3.10 In vitro laser irradiation

Cells were seeded at a density of 2.5×10^5 cells per well and treated with 3MPA-GGS and FA-3MPA-GGS NPs at 50–200 µg Au/mL concentrations for 6 hours. Following the incubation, the medium was replaced with fresh medium, and the cells were irradiated from the bottom of the plate with a 795 nm laser (1 W, 2.6 W/cm^2) for 10 minutes. After overnight incubation, cell viability was assessed using the MTT assay. Untreated cells were the control, while cells exposed to laser irradiation without NP treatment were designated as the laser control (LC).

3.3.11 In vitro X-ray irradiation

Cells were seeded and treated with 3MPA-GGS and FA-3MPA-GGS NPs at 50–200 µg Au/mL concentrations. After 6 hours of incubation, the medium was replaced with fresh medium. The cells were then irradiated with a 0.5 Gy X-ray dose using an X-ray irradiator (Xstrahl Life Sciences, CIX cabinet). Following overnight incubation, cell viability was evaluated using the MTT assay. Untreated cells were the control, while cells subjected to X-ray irradiation without NP treatment were designated as the radiation control (RC).

3.3.12 In vitro ROS generation

HeLa, MDA-MB-231, and A549 cells were treated with 3MPA-GGS and FA-3MPA-GGS at 25 µg Au/mL concentrations for intracellular ROS detection. After 24 hours of incubation, the medium was removed, and the cells were washed with PBS. Subsequently, the cells were incubated with 10 µM DCFH-DA for 40 minutes at 37 °C. Following staining, each group was irradiated with a 0.5 Gy X-ray dose. The fluorescence intensity was measured at excitation/emission wavelengths of 485/535 nm ($\lambda_{ex}/\lambda_{em}$=485/535 nm).

3.3.13 LDH assay

HeLa cells were plated at $1x10^5$ cells per well (n=3) into 96-well plates, treated with 3MPA-GGS and FA-3MPA-GGS at 100 µg Au/mL concentrations, and incubated for 6 h. In addition to the samples, extra wells of cells without treatment (Control) and cells treated with Tergitol (Total Lysis) were included. 24 h after the laser and x-ray treatments, the LDH assay reagent was added to the wells and incubated for 10 minutes. The

absorbance was measured at 500 nm using a microplate reader. The cytotoxicity is calculated as the percentage of the maximum LDH release in the total lysis wells compared to the treated wells: Cytotoxicity (%) = 100 x (absorbance (treated) – absorbance (control)) / (absorbance (total lysis) - absorbance (control)) (n =3).

3.3.14 Statistical analysis

For the statistical analysis of quantitative results, Dunnett's multiple comparison tests were used (GraphPad Software, Inc.). All data were expressed as mean ± standard deviation (SD), and $p < 0.05$ was considered statistically significant.

3.4 Results and Discussion

3.4.1 Synthesis and Characterization of 3MPA-GGS and FA-3MPA-GGS

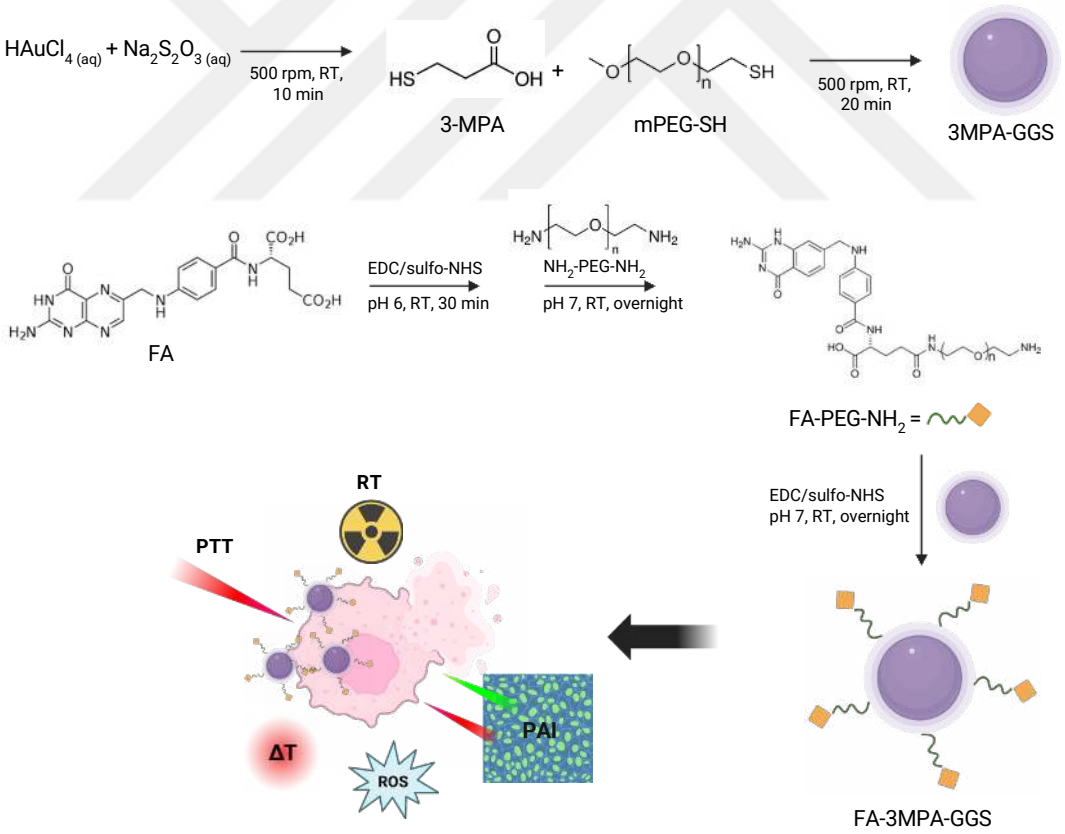

Figure 3.1 Schematic illustration of the synthesis of 3MPA-GGS and FA-3MPA-GGS.

The synthesis of 3MPA-GGS NPs was previously reported in our studies and is summarized in Figure 3.1 [189]. Briefly, the NPs were synthesized in a single-step reaction by reacting $HAuCl_4$with $Na_2S_2O_3$, followed by the addition of 3MPA as a stabilizing coating. The resulting 3MPA-GGS exhibited two absorption peaks at 530 and 840 nm (Figure 3.2A) and a hydrodynamic size of 2.5 nm (number-based average) and 63.0 nm (intensity-based average) with a zeta potential of -24.1 mV, indicating the anionic nature of the NPs (Table 3.1). TEM showed that 3MPA-GGS and FA-3MPA-GGS consist of small spherical NPs less than 3 nm and some non-spherical NPs larger than 30 nm from one edge (Figure 3.2B).

To conjugate FA to the NPs, an H_2N-PEG-NH_2 linker was employed. This linker introduced amine groups to the nanoparticles, providing an amidation reaction with the carboxylic acid groups of FA. Initially, the carboxylic acid groups of FA were activated using EDC/sulfo-NHS in water, allowing them to react with the amine groups of PEG-diamine. Subsequently, the carboxylic acid groups on 3MPA-GGS were activated using the same EDC/sulfo-NHS procedure and reacted with the pre-synthesized H_2N-PEG-FA conjugate. The efficiency of FA conjugation was calculated to be 70%.

FA conjugation did not significantly change the zeta potential or the optical properties of the nanoparticles. However, it caused a slight increase in the hydrodynamic size to 2.7 nm (number-based average) and 73.4 nm (intensity-based average). This size increase is associated with the presence of the 2 kDa PEG chains conjugated to the nanoparticle surface.

Table 3.1 Hydrodynamic sizes and zeta potentials of 3MPA-GGS and FA-3MPA-GGS.

Sample name	D_h-number[a] (nm)	D_h-intensity[b] (nm)	Zeta potential (mV)
3MPA-GGS	2.5	2.6, 63.0	-24.1
FA-3MPA-GGS	2.7	2.7, 73.4	-21.0

The hydrodynamic size was measured by DLS and reported as [a] number average and [b] intensity average.

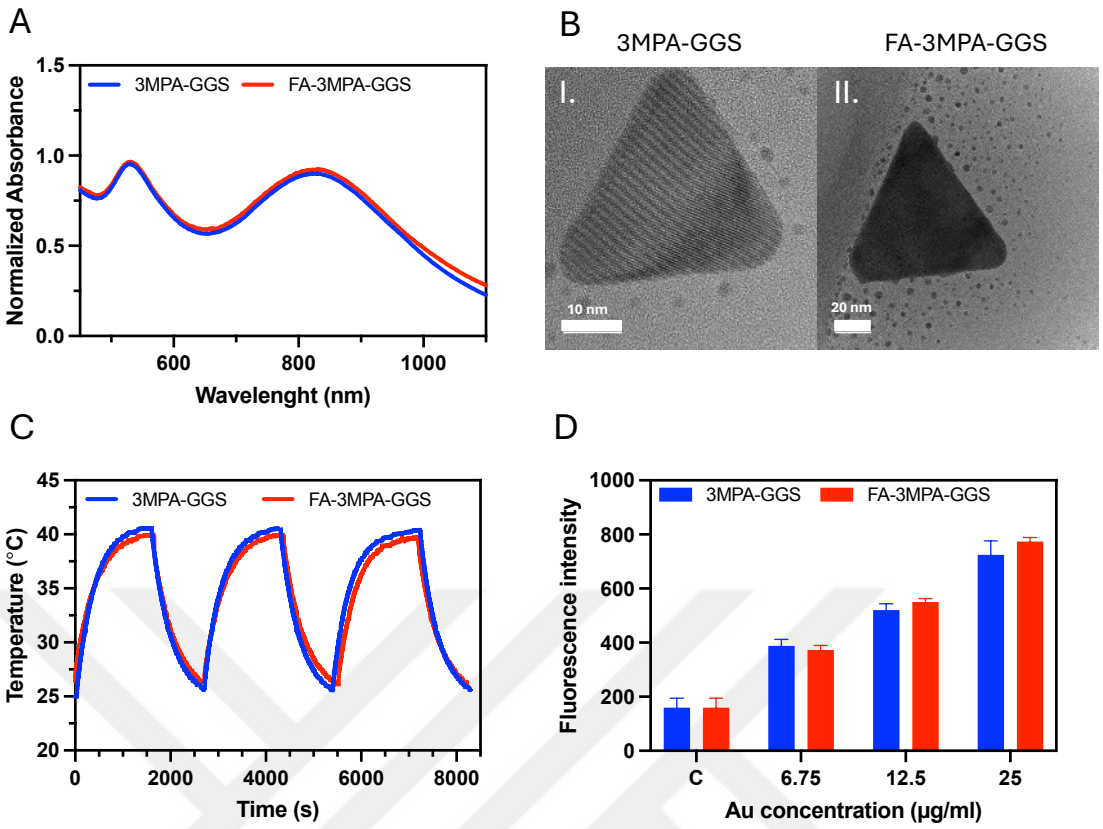

Figure 3.2 (A) UV−vis spectra and (B) TEM images of 3MPA-GGS and FA-3MPA-GGS. (C) Time-dependent change in the temperature of 3MPA-GGS and FA-3MPA-GGS solutions, after laser on/off cycles (200 µg/mL, 808nm, 215 mW) (D) Dose-dependent ROS production of 3MPA-GGS and FA-3MPA-GGS upon 2 Gy irradiation.

3.4.2 Photothermal potential

Solution heating.

The heating potential of 3MPA-GGS and FA-3MPA-GGS were investigated under continuous fiber-coupled laser diode laser irradiation at 808 nm using 215 mW power. Nanoparticle solutions of 50, 100, and 200 µg Au/mL concentrations were irradiated for 25 minutes, and the temperature increase was followed using a thermocouple. For 3MPA-GGS and FA-3MPA-GGS, the 200 µg Au/mL concentrations increased the solution temperature by 16.0 and 16.3 °C, respectively (Figure 3.3). Significant temperature increases in the NP solutions show the strong PTT potential of GGS. The light-to-heat conversion efficiency of 3MPA-GGS and FA-3MPA-GGS were calculated as 56% and 76%, respectively.

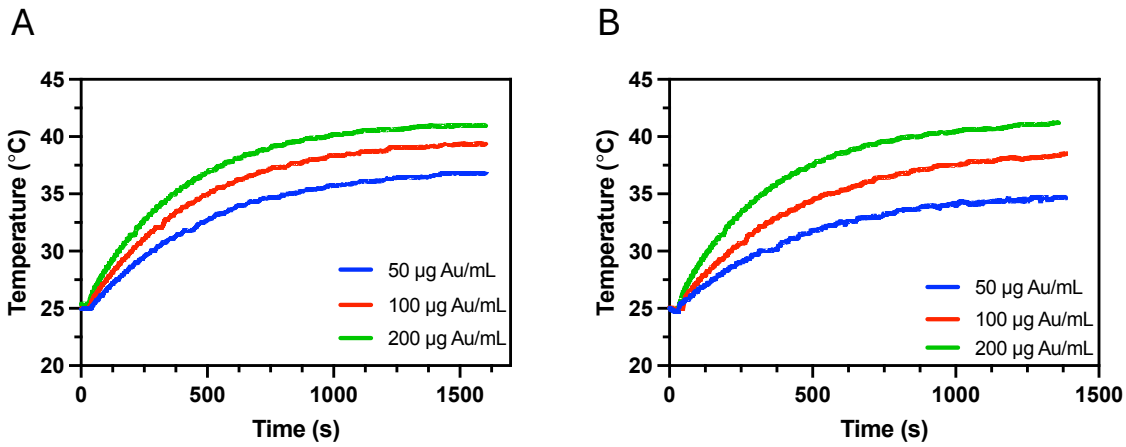

Figure 3.3 Time-dependent change in the temperature of (A) 3MPA-GGS and (B) FA-3MPA-GGS solutions at 50-200 µg/ Au/mL concentrations irradiated at 808 nm, 215 mW.

Further, to demonstrate the photostability of GGS NPs, we performed three cycles of on/off irradiation experiments (Figure 3.2C). 3MPA-GGS and FA-3MPA-GGS had the same ΔT after each heating and cooling cycle. This shows that GGS NPs can be used as PTT agents multiple times without showing any decrease in PTT efficiency.

3.4.3 ROS Generation

The generation of ROS during X-ray irradiation of gold NPs is primarily attributed to the ejection of electrons and subsequent chemical reactions [36]. These electrons interact with molecular oxygen and water, leading to the formation of ROS. ROS production was evaluated following X-ray irradiation to investigate the radiosensitization potential of the GGS NPs (Figure 3.2D).

DCFH-DA dye was used as a fluorescent probe to detect ROS in 3MPA-GGS and FA-3MPA-GGS solutions. Lower concentrations of GGS (6.75-25 µg Au/mL) were used in the experiments to avoid interference caused by the strong absorbance of GGS, which can interact with the fluorescence of DCFH-DA. Upon exposure to a 2 Gy X-ray dose, ROS generation was observed for both NPs, with ROS levels increasing proportionally with the Au concentration. Notably, the conjugation of FA to the NPs did not significantly change ROS production, indicating that FA conjugation does not affect the radiosensitization properties of the NPs.

3.4.4 Cytotoxicity evaluation

The cytotoxicity of 3MPA-GGS and FA-3MPA-GGS nanoparticles (NPs) was assessed dose-dependent using the MTT metabolic activity assay. The study included L929 healthy fibroblast cells, HeLa and MDA-MB-231 folate receptor-positive cancer cell lines, and A549, a folate receptor-negative cancer cell line. Cells were exposed to NPs at 25 to 500 µg Au/mL concentrations and incubated for 24 and 48 hours.

After 24 hours of incubation, both NPs demonstrated minimal toxicity to L929 and MDA-MB-231 cells, maintaining viabilities above 80%, in accordance with ISO 10993-5 guidelines (Figure 3.3A, C). In HeLa cells, 3MPA-GGS treatment showed no reduction in viability across all tested concentrations, whereas FA-3MPA-GGS at 350 µg Au/mL resulted in cell viability of approximately 75% (Figure 3.3B). For A549 cells, viability was reduced to around 75% and 70% at the highest tested concentration of 500 µg Au/mL for 3MPA-GGS and FA-3MPA-GGS, respectively (Figure 3.3D).

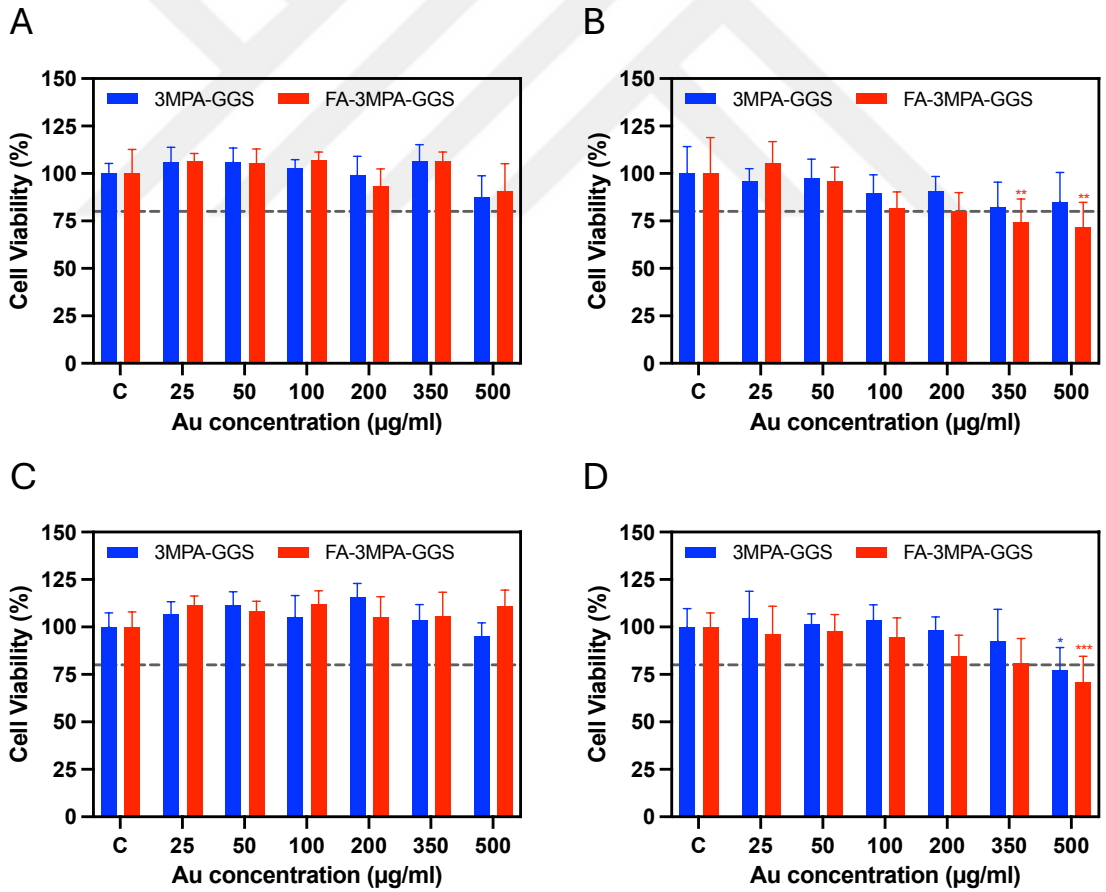

Figure 3.4 Viability of (A) HeLa, (B) MDA-MB-231, (C) A549, and (D) L929 cells treated with 3MPA-GGS and FA-3MPA-GGS at 25−500 µg Au/mL after 24 h of incubation determined by the MTT assay (n= 5). (0.0332 (*), 0.0021 (**), 0.002 (***), <0.001 (****)).

Extending the incubation to 48 hours revealed more pronounced effects. In HeLa cells, viability decreased below 80% at concentrations above 50 µg Au/mL, with a further decline observed at higher concentrations (Figure 3.5A). MDA-MB-231 cells displayed negligible changes in viability over the tested concentration range (Figure 3.5B). In contrast, A549 cells exhibited a decrease in viability below 80% at concentrations exceeding 100 µg Au/mL, with a progressive decline at higher concentrations (Figure 3.5C). For L929 cells, viabilities were 68% and 62% following treatment with 500 µg Au/mL of 3MPA-GGS and FA-3MPA-GGS, respectively (Figure 3.5D).

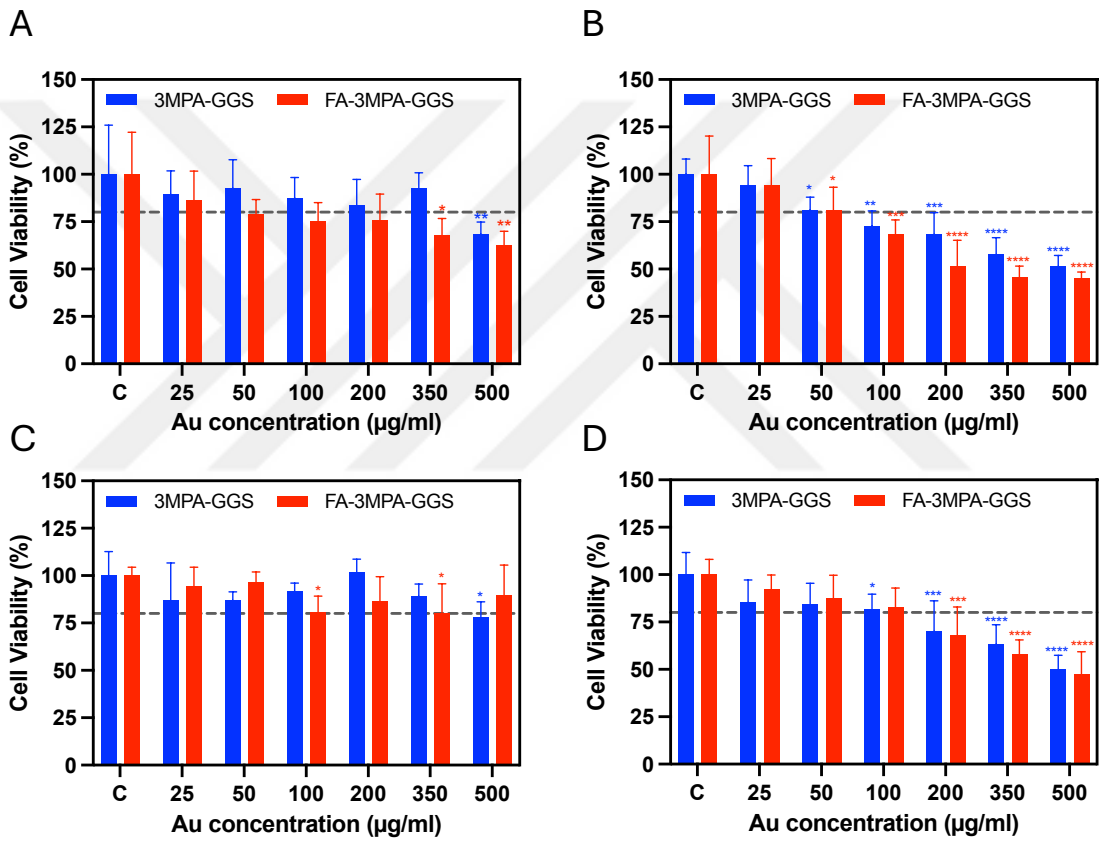

Figure 3.5 Viability of (A) HeLa, (B) MDA-MB-231, (C) A549, and (D) L929 cells treated with 3MPA-GGS and FA-3MPA-GGS at 25−500 µg Au/mL after 48 h of incubation determined by the MTT assay (n= 5). (0.0332 (*), 0.0021 (**), 0.002 (***), <0.001 (****)).

3.4.5 Cellular uptake

The internalization of 3MPA-GGS and FA-3MPA-GGS by HeLa, MDA-MB-231, and A549 cells were quantitatively detected using ICP-MS measurement (Figure 3.6). To

observe the active targeting of the nanoparticles through receptor-mediated endocytosis rather than a passive uptake for a long time, cells were treated with nanoparticles and incubated for 6 h. The [Au] content of HeLa cells was 34% when they were treated with 3MPA-GGS, and when NPs were folic acid tagged, the intracellular uptake rose to 77%. MDA-MB-231, a moderate folate receptor-positive cell, showed 27% and 43% cellular uptake of 3MPA-GGS and FA-3MPA-GGS, respectively. A549, folate receptor-negative cells, did not show a significant increase in the uptake when the nanoparticles were folic acid tagged. 7% and 11% cellular uptake was obtained with treatment with 3MPA-GGS and FA-3MPA-GGS.

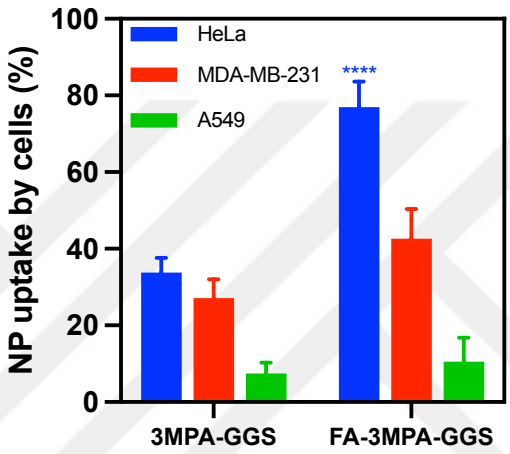

Figure 3.6 Intracellular quantification of 3MPA-GGS and FA-3MPA-GGS in HeLa, MDA-MB-231, and A549 cells after 6 hours incubation. (0.0332 (*), 0.0021 (**), 0.002 (***), <0.001 (****)).

3.4.6 In vitro photoacoustic imaging/microscopy:

Photoacoustic microscopy (PAM) is a powerful, label-free technique for visualizing nanoparticle distribution in biological tissues with high spatial resolution. The near-infrared (NIR) absorption of 3MPA-GGS nanoparticles makes them effective contrast agents for imaging deeply seated cancer cells, offering a noninvasive alternative to conventional optical imaging methods. Since the intensity of photoacoustic signals directly correlates with local optical absorption, PAM enables precise quantification of NP concentration without the need for fluorescent labeling. This capability is particularly advantageous for cellular uptake studies, where nanoparticle accumulation is influenced by size, morphology, and cell line specificity. This work further shows that integrating PAM with cellular uptake studies makes it possible to assess how these parameters directly impact NP uptake at the single-cell level, providing crucial insights for biomedical applications [191].

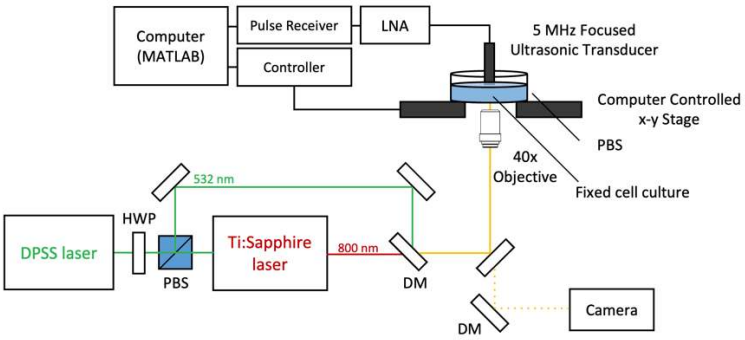

Figure 3.7 Schematic illustration of the photoacoustic microscope (PAM) with 532 and 800 nm lasers. HWP: half-wave plate, PBS: polarizing beam splitter, DM: dichroic mirror, LNA: low-noise amplifier.

In this section, we successfully demonstrated the potential of PAM in visualizing the accumulation of FA-3MPA-GGS NPs in FR+ (HeLa and MDA-MB-231) and compared it with FR- (A549) cell lines. Figure 3.8 (A-C) presents bright-field images of the scanned area and PAM images obtained with lasers operating at 532 and 800 nm. The laser wavelength selection was made based on the UV-VIS spectra of the 3MPA-GGS samples.

When we look at the PAM images recorded at 800 nm with FA-GGS-3MPA and GGS-3MPA, it can easily be understood that PAM was able to differentiate the uptake performance of the FR+ cell line of HeLa (Fig 3.8A) and MDA-MB-231 (Fig 3.8B) to the FR- cell line of A549 (Fig 3.8C). In Figure 3.8C, compared to Figure 4A and B, no significant contrast is left at 800nm, suggesting that in a mixture of folate receptor-sensitive cells, the FA-3MPA-GGS particles will only accumulate in the actively targeted ones, which dramatically enhance the local effect of RT and PTT. This is also reflected in the PTT/RT dose-dependent cell viability results in Figure 3.9.

We performed inductively coupled plasma mass spectrometry (ICP-MS) analysis to further validate the PAM imaging results and quantify [Au] content in FA-tagged cases. The results revealed a decreasing trend in NP accumulation across different cell lines, with HeLa (77%) exhibiting the highest uptake, followed by MDA-MB-231 (43%) and A549 (11%). Notably, while this trend is consistent with PAM imaging, it is essential to consider that PAM signals recorded at 532 nm and 800 nm correspond to different nanoparticle morphologies. Specifically, 532 nm imaging primarily detects smaller GGS particles, whereas the broader absorption band at 800 nm corresponds to larger GGS structures [189]. Despite these morphological variations, PAM imaging effectively

captures the overall distribution trend observed in ICP-MS (Figure 4), reinforcing its reliability as a visualization tool.

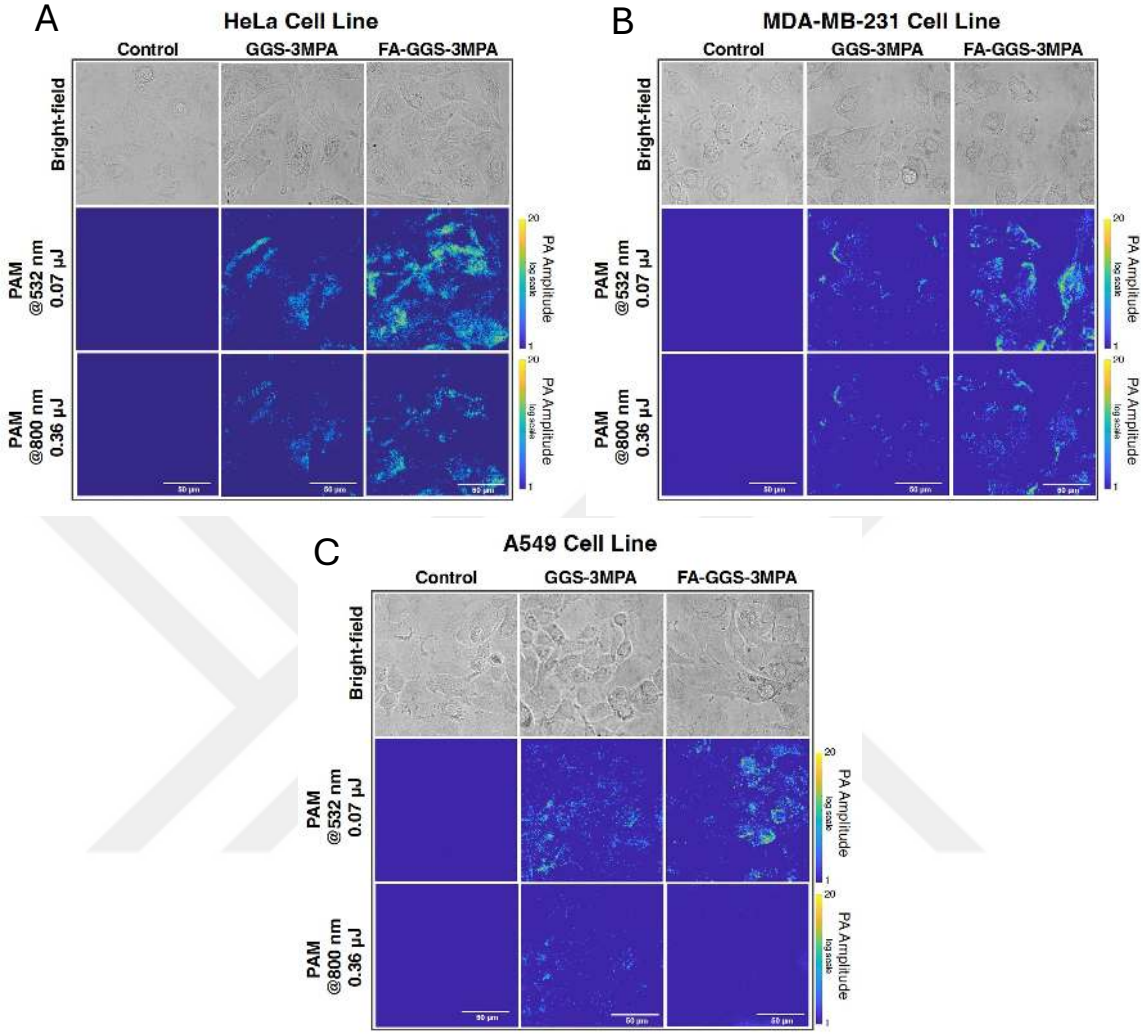

Figure 3.8 PAM images of (A) HeLa, (B) MDA-MB-231 cells, and (C) A549 at λ =532 and 800 nm, incubated with 100 µg Au/mL 3MPA-GGS and FA-3MPA-GGS for 6 hours. Blue corresponds to the background, and yellow shades represent the PA signal amplitude.

3.4.7 In vitro PTT/RT combination

Laser-only irradiation. Cells treated with 3MPA-GGS and FA-3MPA-GGS nanoparticles were exposed to 795 nm laser irradiation at 1 W power for 10 minutes after 6 hours of incubation with nanoparticle concentrations ranging from 50 to 200 µg Au/mL. Control groups receiving laser treatment alone did not exhibit any loss in viability, confirming that the chosen irradiation parameters do not induce phototoxicity. In HeLa cells, viability decreased to 73% with 3MPA-GGS treatment and 45% with FA-3MPA-

GGS at 200 μg Au/mL, demonstrating enhanced nanoparticle internalization due to folic acid tagging (Figure 3.9A). Similarly, MDA-MB-231 cells exhibited 51% and 34% viabilities for 3MPA-GGS and FA-3MPA-GGS, respectively (Figure 3.9B). A549 cells showed less sensitivity to PTT, with 84% and 79% viabilities for 3MPA-GGS and FA-3MPA-GGS, respectively (Figure 3.9C).

X-ray irradiation. Cells were exposed to a 0.5 Gy X-ray dose after 6 hours of incubation with nanoparticles at concentrations ranging from 50 to 200 μg Au/mL. Control groups exposed to X-ray irradiation alone showed no significant loss in viability. In HeLa cells, viability decreased to 85% with 3MPA-GGS treatment and 49% with FA-3MPA-GGS at 200 μg Au/mL (Figure 3.9D). For MDA-MB-231 cells, viabilities were reduced to 78% with 3MPA-GGS and 53% with FA-3MPA-GGS (Figure 3.9E). A549 cells exhibited 67% and 56% viabilities with 3MPA-GGS and FA-3MPA-GGS, respectively (Figure 3.9F). These results indicate that a low, single-dose X-ray treatment combined with folic acid-tagged nanoparticles can reduce cell viability to IC50 levels.

Laser and X-ray combination. Cells were first treated with laser irradiation followed by X-ray exposure under the same parameters as the individual treatments. This combined approach aimed to overcome cellular resistance by utilizing mild PTT and low-dose radiotherapy. At the highest nanoparticle dose (200 μg Au/mL), HeLa and MDA-MB-231 cells demonstrated significant reductions in viability, below 10%, when treated with folic acid-tagged nanoparticles (Figure 3.9G, H). For A549 cells, viabilities decreased to around 55-50% for 3MPA-GGS and FA-3MPA-GGS (Figure 3.9I). Combining PTT and RT with folic acid-tagged GGS nanoparticles enhanced therapeutic efficacy even more, particularly in folate receptor-positive cancer cell lines. The concurrent strategy efficiently inhibited cell viability, demonstrating its ability to overcome treatment resistance and achieve synergistic therapeutic effects, even at low X-ray doses.

When evaluating the therapeutic response, the cell viability results for combined PTT/RT deviate from the uptake trends observed of FR+ cells in ICP-MS and PAM imaging. Despite internalizing fewer targeted GGS NPs than HeLa cells, MDA-MB-231 cells exhibited a similar reduction in cell viability after PTT and RT treatments. This discrepancy likely stems from differences in the susceptibility of HeLa and MDA-MB-231 cells toward radiosensitization. Previous studies indicate that HeLa cells are less sensitive to radiation therapy. Nevertheless, in this study, the higher uptake of GGS NPs by HeLa cells appears to increase radiosensitivity, leading to a notable enhancement in RT efficacy at very low RT doses (0.5 Gy). Consequently, while PAM and ICP-MS

confirm selective NP accumulation in FR+ cells, these findings highlight the promising therapeutic potential of FA-3MPA-GGS NPs, particularly for enhancing RT/PTT outcomes.

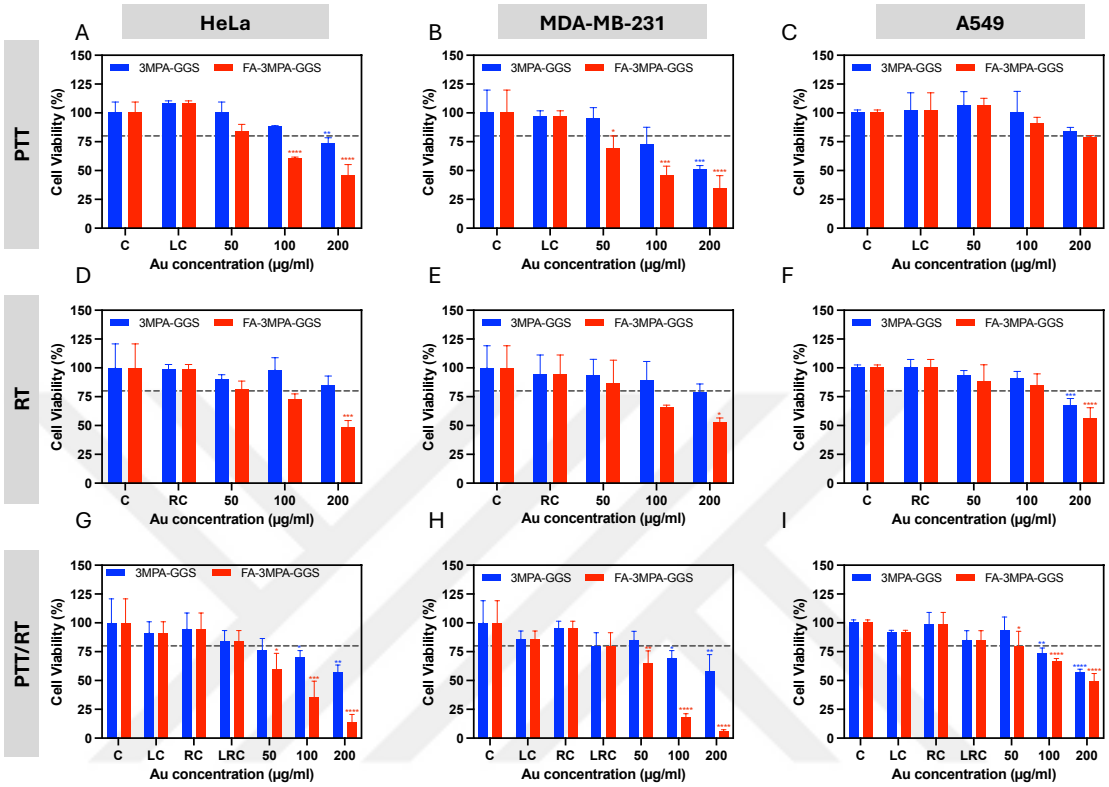

Figure 3.9 Cell viability in a dose-dependent manner for treatments with (A–C) PTT only, (D–F) RT only, and (G–I) PTT/RT combination on HeLa, MDA-MB-231, and A549 cell lines, respectively, treating with 3MPA-GGS and FA-3MPA-GGS nanoparticles for 6 hours. Data are presented as mean ± S.D. (n = 5). PTT parameters: 795 nm, 1 W power, 10 min irradiation; RT dose: 0.5 Gy. (0.0332 (*), 0.0021 (**), 0.002 (***), <0.001 (****)).

3.4.8 Cell heating

To show the photothermal effect of laser irradiation, the temperature rise in the cells was followed by a thermal camera (Figure 3.10A). HeLa, MDA-MB-231, and A549 cells were irradiated with the same PTT protocol. Only laser treatment did not cause a significant rise around 1 °C for all cell lines (Figure 3.10B). HeLa cells were heated at 2.8 °C when treated with 3MPA-GGS and at 6.4 °C with FA-3MPA-GGS, showing a higher accumulation of FA-tagged nanoparticles. The temperature of the MDA-MB-231 cells was raised to 2.1 °C, and the targeting temperature was increased to 3.4 °C. The

temperature of A549 cells increased 1.8 °C and 1.4 °C for 3MPA-GGS and FA-3MPA-GGS, respectively, showing no significant difference between nanoparticles.

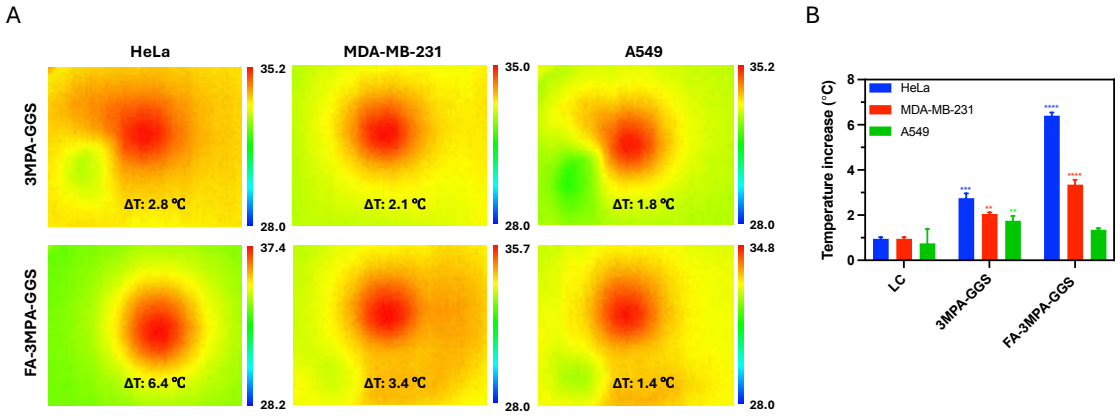

Figure 3.10 (A) Thermal camera images and (B) temperature increases of 3MP-GGS and FA-3MPA-GGS (200 µg Au/mL) treated HeLa, MDA-MB-231, and A549 cells irradiated at 795 nm for 10 min.

3.4.9 In vitro ROS generation

ROS production is a key mechanism of X-ray-induced cell death in radiotherapy, driven by the radiolysis of water and charge transfer processes initiated by the emission of electrons when gold nanoparticles are irradiated with X-rays [30]. In vitro ROS generation of dark, PTT, RT, and PTT/RT groups was evaluated using a fluorescent DCFH-DA probe following 6 h incubation of NPs and treatment procedures with HeLa, MDA-MB-231, and A549 cells. No ROS production was detected in all three cell lines treated with NPs in the dark and laser irradiated. A significant rise in the ROS generation was observed for the X-ray irradiated cells. However, a substantial increase in ROS levels was observed following X-ray irradiation, particularly in FA-3MPA-GGS-treated HeLa cells, where RT alone led to a 3.2-fold increase in ROS compared to the dark control group (Figure 3.11A). ROS levels increased further when RT was combined with PTT, reaching a 3.7-fold enhancement. The contribution of PTT to ROS levels can be attributed to the oxidative stress triggered by heat stress, especially in the mitochondria [192, 193]. The heat from PTT speeds up chemical reactions that produce ROS, causing cell damage and enhancing the therapy's effectiveness [194]. The study by Minai et al. demonstrated that gold nanoparticle-treated BJAB and MDA-MB-23 cells generate high concentrations of ROS upon laser irradiation [195].

In FA-3MPA-GGS-treated MDA-MB-231 cells, RT induced a 1.8-fold increase in ROS, which rose to 2.2-fold with the PTT/RT combination (Figure 3.11B). In A549 cells, RT and PTT/RT treatments led to 1.2- and 1.5-fold increases in ROS levels, respectively, showing similar radiosensitization of the two nanoparticles (Figure 3.11C). Overall, FA-3MPA-GGS enhances ROS production selectively in receptor-positive cells and supports the synergistic potential of combining PTT and RT for improved therapeutic outcomes.

3.4.10 LDH release

Lactate dehydrogenase (LDH) is an enzyme released when a cell's membrane integrity is disrupted due to necrosis [196]. Therefore, the detection of LDH release is essential for the demonstration of PTT-induced necrosis. Here, LDH levels in HeLa cells were measured for dark, PT, RT, and PTT/RT groups after the treatment with 3MPA-GGS and FA-3MPA-GGS at 100 μg Au/mL. A dramatic increase was observed for the PTT group treated with NPs, showing that laser treatment is the leading cause of the LDH release. LDH levels of FA-3MPA-GGS treated cells were higher than non-targeted GGS, which is relatable with the cell death according to the MTT assay (Figure 3.11D). No significant change was observed for the RT group for control and 3MPA-GGS treated cells, and a minimal rise in the LDH levels was observed for the FA-3MPA-GGS treated group. High LDH levels were observed for the PTT/RT combination similar to the PTT-only. There was no significant change between the PTT and PTT/RT combination. These results indicate that all the LDH-related cytotoxicity arises from PTT, causing necrotic cell death.

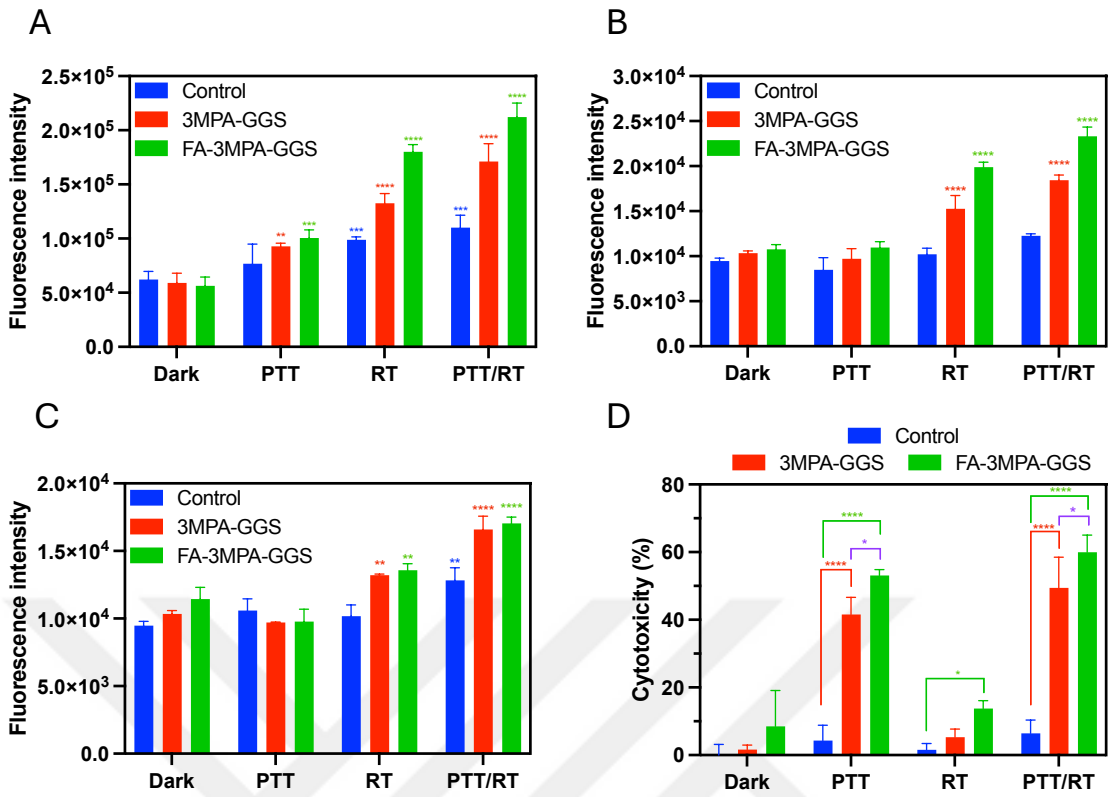

Figure 3.11 ROS production in (A) HeLa, (B) MDA-MB-231, and (C) A549 cells under different treatment conditions: no irradiation, PTT, RT, and PTT/RT combination, after 6 hours of incubation with 100 µg Au/mL of 3MPA-GGS and FA-3MPA-GGS. (D) Cytotoxicity assessment through LDH levels in HeLa cells under the same treatment conditions and nanoparticle concentrations. Data are presented as mean ± S.D. (n = 3). (0.0332 (*), 0.0021 (**), 0.002 (***), <0.001 (****)).

3.5 Conclusion

This research demonstrated the efficacy of folic acid-coupled gold-gold sulfide nanoparticles as a novel theranostic nanoplatform for targeted anticancer therapy. By combining the high NIR absorbance, high photothermal efficacy, and radiosensitization features, the like nanoparticles become cancer treatment-effective with specificity. With the assistance of folic acid conjugation, targeted folate receptor-specific delivery was conducted, enhancing substantially increased nanoparticle internalization as well as the therapeutically enhanced effects within FR+ cells. Furthermore, the photothermal properties enabled effective PTT under NIR irradiation, achieving significant localized temperature increases with high photostability over repeated cycles. Enhanced radiosensitization was evident through enhanced ROS generation and synergistic therapeutic effects when combined with low-dose RT.

The FA-3MPA-GGS nanoparticles exhibited excellent performance in photoacoustic imaging, enabling precise visualization of targeted cancer cells due to the high cellular uptake of the nanoparticles. In vitro studies on FR+ (HeLa and MDA-MB-231) and FR– (A549) cell lines confirmed the superior cytotoxicity of FA-3MPA-GGS in targeted cells. The combination of PTT and RT using FA-3MPA-GGS resulted in significant reductions in cell viability, demonstrating the potential to overcome treatment resistance while minimizing the required therapeutic dose. LDH assays and ROS measurements also showed the cell death mechanism, highlighting the critical roles of membrane disruption and oxidative stress in inducing cancer cell death. These multifunctional nanoparticles represent a promising platform for integrated cancer diagnostics and treatment. Their ability to combine imaging-guided precision with synergistic dual-modality therapy offers a minimally invasive, targeted, and efficient approach to cancer theranostics.

Chapter 4: Targeted Dual Phototherapy of Prostate Cancer with ALA-loaded SPIONs

4.1 Abstract

Phototherapies, photothermal therapy (PTT), and photodynamic therapy (PDT) offer alternative, minimally invasive treatment options, particularly for localized cancer treatment, compared to conventional therapies like surgery, chemotherapy, and radiotherapy, which often have limitations such as systemic side effects and non-specific targeting. Nanoparticle-mediated phototherapy has emerged as a promising strategy, as nanoparticles can enhance treatment specificity and efficiency by delivering therapeutic agents directly to tumor cells and facilitating controlled activation with laser irradiation. In this study, we developed and evaluated ALA-loaded superparamagnetic iron oxide nanoparticles (ALA-PAA-SPIONs) for targeted combined PTT and PDT therapy of prostate cancer (PCa) cells. These nanoparticles utilize the selective uptake of 5-aminolevulinic acid (ALA) via PEPT1 and PEPT2 transporters, enhancing accumulation and therapeutic efficacy within cancer cells. Characterization studies confirmed the successful ALA loading and stability of these nanoparticles. In vitro studies on LNCaP, PC3, and DU145 prostate cancer cell lines demonstrated increased cellular uptake, ROS generation, and apoptosis induction with combined PTT and PDT, significantly reducing cell viability. The potential of ALA-PAA-SPIONs as effective dual-mode phototherapy agents for prostate cancer treatment was demonstrated.

4.2 Introduction

Prostate cancer (PCa) is the second most frequently diagnosed cancer and the fifth leading cause of cancer-related deaths among men worldwide [197]. By 2040, a 40-50% increase in PCa incidence is anticipated due to factors such as aging populations and lifestyle changes [198]. Standard treatment options for PCa include surgery, chemotherapy, radiotherapy, and androgen deprivation therapy; however, these methods can have limitations, including non-specific targeting and adverse side effects, especially during prolonged therapy.

In recent years, phototherapies, particularly photothermal therapy (PTT) and photodynamic therapy (PDT) have emerged as promising alternatives for treating various cancers, including PCa [199]. Combining these phototherapies or using single-modality phototherapies with conventional treatments may enhance therapeutic outcomes. In PTT, nanoparticles such as gold [200], copper [201], carbon nanotubes [202], and superparamagnetic iron oxide nanoparticles (SPIONs) [203] are irradiated with laser light to ablate tumor cells through localized heating. SPIONs, in particular, are favored in PTT due to their biocompatibility and FDA-approved formulations [204]. However, single-modality SPION-based PTT often requires high doses and laser power to achieve efficacy. Combining PTT with PDT allows for localized, minimally invasive treatment where tumor-specific irradiation generates heat (PTT) and reactive oxygen species (PDT), selectively damaging cancer cells with minimal systemic effects. This light-activated, controlled method not only enhances targetability but also decreases the risk of injury to nearby healthy tissues, and thus these treatments are extremely appealing for prostate cancer and other localized cancers.

PDT is a form of phototherapy that generates reactive oxygen species (ROS) to destroy cancer cells when photosensitive molecules are irradiated at specific wavelengths [205]. A common PDT agent is 5-aminolevulinic acid (ALA), an FDA-approved prodrug converted within cells to the photosensitizer protoporphyrin IX (PpIX) [206, 207]. Upon irradiation at 400 or 630 nm, typically using LED or laser light, ALA-generated PpIX produces ROS, leading to cell death.

Notably, ALA can exhibit selective uptake in cancer cells that overexpress the membrane transporter proteins PEPT1 and PEPT2, facilitating cellular uptake [208, 209]. These transporters allow ALA to act as a targeted agent in cancer therapy, enhancing its accumulation in cancer cells over healthy ones. However, ALA's zwitterionic, hydrophilic nature has advantages compared to other conventional photosensitizers. However, the low bioavailability of ALA limits its clinical application, resulting in quick removal from the body [210, 211]. By providing ALA’s delivery to target cells and improving bioavailability, nanocarriers may enhance PDT efficiency and allow for dose reduction.

Utilizing these transporters, our previous studies demonstrated that delivering ALA via nanoparticles can reduce the required dose and increase phototoxic effects against tumor cells [136]. This selective uptake by PEPT1 and PEPT2, especially in prostate

cancer cells, holds significant potential for improved targeting, as it maximizes ALA's accumulation and therapeutic impact within the tumor microenvironment.

In this study, we developed ALA-loaded SPIONs (ALA-PAA-SPIONs) as multifunctional agents for combined phototherapy in prostate cancer treatment. By integrating 5-ALA as a targeting moiety and photosensitizer, these nanoparticles allow for precise cancer cell targeting and enhanced phototoxicity under laser activation. This approach utilizes the selective uptake properties of ALA and maximizes the therapeutic impact, specifically within prostate cancer cells. Using ALA-PAA-SPIONs for combined PTT and PDT enhances treatment efficiency. It is highly effective in killing tumor cells at lower doses, illustrating the potential of such targeted phototherapies in the therapy of prostate cancer.

*4.3 **Materials and Methods***

4.3.1 Materials

Iron (II) chloride and iron (III) chloride were supplied from Merck (purity levels 99 %, Darmstadt, Germany). Poly (acrylic acid) (PAA) with an average molecular weight of 5100 Da was purchased from Sigma (MO, USA). Ethyl-3-(3-di- methylaminopropoyl) carbodiimide (EDC) and N-hydroxysulfosuccinimide (sulfo-NHS), and Alexa Fluor 647 were purchased from Thermo Scientific (USA). 5-Aminolevulinic acid hydrochloride (ALA) was bought from Research Products International (RPI, USA). Vivaspin 20 centrifugal filters were obtained from Sartorius (Gottingen, Germany). Ultra-pure water was used in the experiments (18.2 MΩ, Rephile Bioscience, and Technology, Shanghai, China). Roswell Park Memorial Institute 1640 (RPMI) medium, fetal bovine serum, trypsin-EDTA, L-glutamine, and penicillin-streptomycin were obtained from Gibco (Gibco, Grand Island). Phosphate-buffered saline (PBS) tablets and thiazolyl blue tetrazolium bromide (MTT) were supplied from Bio-matik Corp. (Canada).

4.3.2 Synthesis of PAA-SPIONs

Poly (acrylic acid) coated SPIONs were synthesized by a co-precipitation method from iron salts Fe^{3+}/Fe^{2+} of 2/1 (mol ratio) basic pH at 85 °C under an argon atmosphere, as described in our previous work [212]. After one hour of reaction, the colloidal solution was cooled to room temperature and left on a magnet to remove any precipitated particles.

Finally, PAA-SPIONs were washed several times with DI water using 5 kDa centrifugal filters and stored at room temperature.

4.3.3 Electrostatic loading of ALA to PAA-SPIONs (ALA-PAA-SPION)

ALA was dissolved in PBS at pH 7, filtered using a 0.2 μm sterile filter, added to PAA-SPION in PBS at RT for 1 hour, and kept in the dark. Electrostatic loading of ALA was confirmed with Isothermal titration calorimetry (Affinity ITC, USA). PAA-SPIONs (1 mL, 1 mg/mL in PBS) were titrated with ALA (250 μL from 5mg/mL in PBS) at a rate of 5 μL/s at 25°C. Exotherms observed throughout the titration confirmed the electrostatic binding of ALA to SPIONs (Fig. S2).

4.3.4 Characterization

The iron content of the SPIONs was determined using an Agilent 7700X inductively coupled plasma-mass spectrometer (ICP-MS). The samples were etched with nitric acid (65%) and sulphuric acid (96%). The absorption spectrum of the SPIONs was measured by Shimadzu UV-VIS-NIR spectrophotometer. Hydrodynamic sizes and zeta potentials were measured using Malvern Zetasizer Nano ZS. The size and shape of the nanoparticles were investigated with Hitachi 7800 TEM.

4.3.5 Cell Culture

LNCaP, PC3, and Du145 prostate cancer cells were cultured in Roswell Park Memorial Institute Medium (RPMI), L929 healthy fibroblast cells were cultured in Dulbecco's Modified Eagle Medium (DMEM) supplemented with 10% fetal bovine serum, 2% L-glutamine (2 mM), and 1% penicillin-streptomycin at a 37 °C humidified incubator with 5% CO_2 atmosphere. For every experiment, cells were collected when they reached 80% confluence, washed with PBS, and trypsinized with 0.05% trypsin-EDTA before passage and seeding.

4.3.6 Cytotoxicity Assay

MTT metabolic activity assay was used to determine the cytotoxicity of the samples. Materials were sterilized using 0.2 μm sterile filters. LNCaP, PC3, Du145, and L929 cells were seeded into 96-well plates with 1 x 10^4 cell/well density. After overnight incubation, cells were treated with PAA-SPION, free ALA, and ALA-PAA-SPION between 6.25–

200 µg Fe/ mL, and free ALA between 0.03–1.15 mM, equivalent to ALA content of ALA-PAA-SPION and incubated for 24 hours. After sample incubation, the medium of the cells was removed, and wells were washed with PBS. MTT reagent (5 mg/mL in PBS) was diluted with medium (1:3 v/v), added to wells, and incubated for 4 hours. Then, formazan was dissolved by adding ethanol: DMSO (1:1 v/v) solution and the plates were slowly shaken on the orbital shaker. The absorbance of the solution was measured at 570 nm and 650 nm by Synergy H1, Biotech microplate reader, and 650 nm was taken as a reference. The viability of the cells was calculated with respect to control cells according to the formula viability (%) = 100 x absorbance (treated) / absorbance (control) (n =5).

4.3.7 Cellular Uptake

For quantitative determination of cellular uptake, the Fe content of treated cells was measured by ICP-MS. LNCaP, PC3, and Du145 cells were seeded into 6-well plates with 1.75 x 10^5 cell/well density in complete RPMI medium and incubated overnight at 37 °C and 5% CO_2. Then, the cells were incubated with PAA-SPION and ALA-PAA-SPION at 100 µg Fe/mL and 0.58 mM ALA for 12 hours. After incubation, the cells were washed three times with PBS to remove un-internalized nanoparticles, trypsinized, and collected. Cells were digested with nitric acid (65%) and sulphuric acid (96%) mixture for one week, and Fe content was measured with ICP-MS (n=3).

4.3.8 PpIX formation

LNCaP, PC3, and Du145 cells were seeded as described in the cytotoxicity assay section. Cells were incubated with PAA-SPION, ALA, and ALA-PAA-SPION at 100 µg Fe/mL and 0.58 mM ALA for 12 hours. After the incubation, the medium was replaced with a serum-free medium, and PpIX fluorescence was measured using a Synergy H1 microplate reader (BioTek) at $\lambda_{ex}/\lambda_{em}$ = 420/635 nm.

4.3.9 In vitro laser irradiation

Each cell line was seeded and treated with PAA-SPION, free ALA, and ALA-PAA-SPION at 25-200 µg Fe/mL and 0.14-1.15 mM ALA concentrations for 12 hours. After 12 hours of incubation, the medium in the wells was removed and replaced with fresh medium before irradiation. Then, the cells were irradiated with a fiber-coupled laser diode at 640 nm (300 mW, 2.6 W/cm^2) for 10 minutes from the bottom of the well plate. During

laser irradiation, the ambient temperature was kept constant at 37 °C inside an incubator. Overnight incubation was followed by irradiation of the cells, and then the cell viability was determined using the MTT assay. Cells not treated with samples but with laser irradiation were referred to as laser control, and cells that were not treated were used as a control.

4.3.10 Determination of cell death mechanisms by flow cytometry

LNCaP, PC-3, and DU-145 cells were seeded into 96-well plates at 1×10^4 cells per well (n=4) and treated PAA-SPION, free ALA, and ALA-PAA-SPION at 100 µg Fe/mL and 0.58 mM ALA and incubated for 12 hours. At the end of the incubation, the cells were collected, washed with PBS, and analyzed for detecting apoptosis and cell death with the caspase 3/7 kit (Millipore, Darmstadt, Germany) and annexin V/dead cell removal kit (Millipore, Darmstadt, Germany) according to the manufacturer's protocol. Cells were treated as described above for cellular reactive oxygen species (ROS) generation. At the end of the treatment, cells were collected and analyzed using the total ROS assay kit by flow cytometry.

4.3.11 Statistical Analysis

Tukey's multiple comparison test was used for the statistical analysis (GraphPad Software, Inc., USA). All data were expressed as mean values ± standard deviation (SD), and $p < 0.05$ was considered statistically significant.

4.4 ***Results and Discussions***

4.4.1 Synthesis and characterization of ALA-PAA-SPIONs

PAA-SPIONs and ALA-loaded PAA-SPIONs (ALA-PAA-SPIONs) were developed for dual PTT and PDT based on our recent work, as shown in Figure 4.1. Electrostatic loading of ALA was confirmed by isothermal titration calorimetry (Figure 4.2B). PAA-SPIONs were produced in small hydrodynamic sizes (number-based hydrodynamic size of 18.8 nm) with strong negative surface charge (-41.9 mV) (Table 4.1). After ALA loading, there was no significant change in hydrodynamic sizes (20.1 nm) and absorbance, while the surface charge increased to -35.9 mV. Overall, ALA-PAA-SPIONs

were successfully developed for the dual PTT and PDT for the treatment of prostate cancer.

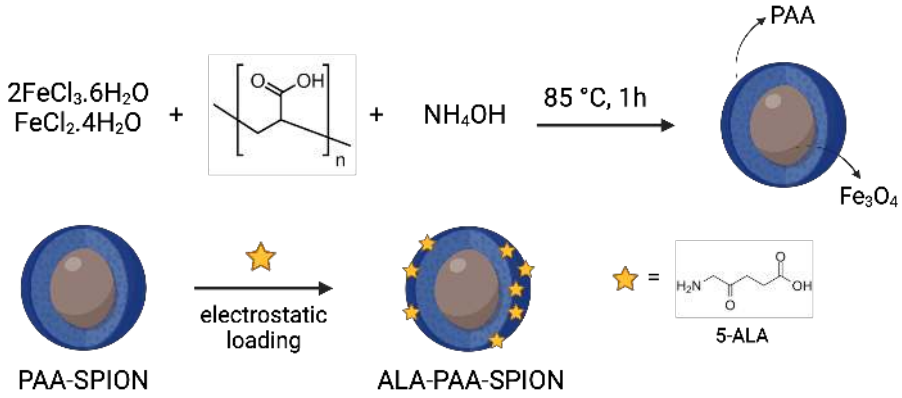

Figure 4.1 Synthesis of ALA-loaded PAA-SPIONs (ALA-PAA-SPIONs).

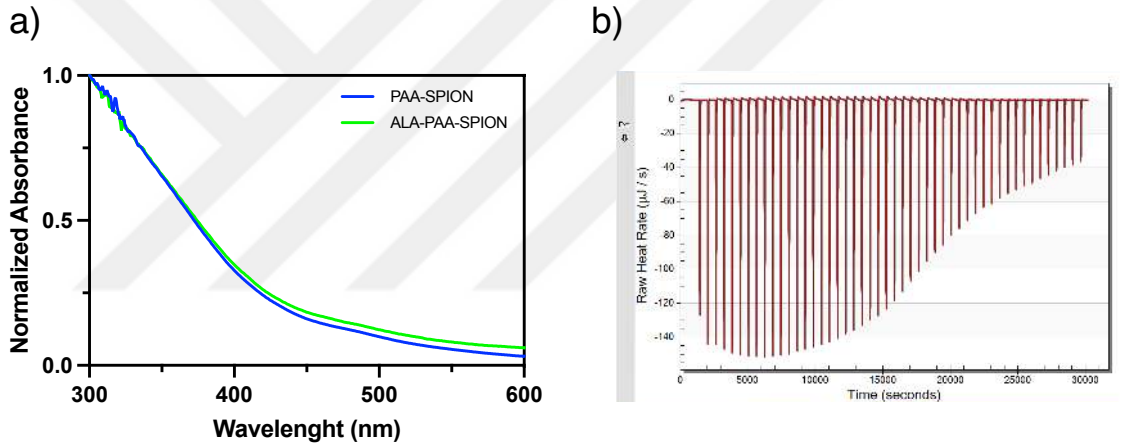

Figure 4.2 a) Absorbance spectra of PAA-SPION and ALA-PAA-SPION NPs. b) Isothermal titration calorimetry (ITC) of ALA-PAA-SPIONs in pH 7 PBS.

Table 4.1 Hydrodynamic sizes and surface zeta potentials of the nanoparticles.

Sample	PDI	Dh-number[a] (nm)	Dh-intensity[b] (nm)	Zeta potential (mV)
PAA-SPION	0.2	18.8	170.4	-41.9
ALA-PAA-SPION	0.2	20.1	171.0	-35.9

[a] Hydrodynamic diameter measured by DLS and reported as the number average. [b] Hydrodynamic diameter measured by DLS and reported as the intensity average.

4.4.2 Combined photothermal and photodynamic therapy

Free ALA, PAA-SPION, and ALA-PAA-SPION phototoxicity were studied on prostate cancer cells, LNCaP, DU145, and PC3, with 640 nm laser treatment at various concentrations. Before testing the photo-therapeutic efficacy, the dark toxicity of each agent was measured at 6.25-200 µg Fe/mL and 0.035-1.15 mM ALA concentrations after 24 h incubation by MTT assay (Figure 4.3). All agents showed negligible toxicity in all cell lines in the studied range; however, slight dark toxicity was observed on the LNCaP cell line at the highest studied dose, reducing the viability to 75-70 %. Further, the biocompatibility of free ALA, PAA-SPION, and ALA-PAA-SPION was confirmed in a healthy fibroblast L929 cell line.

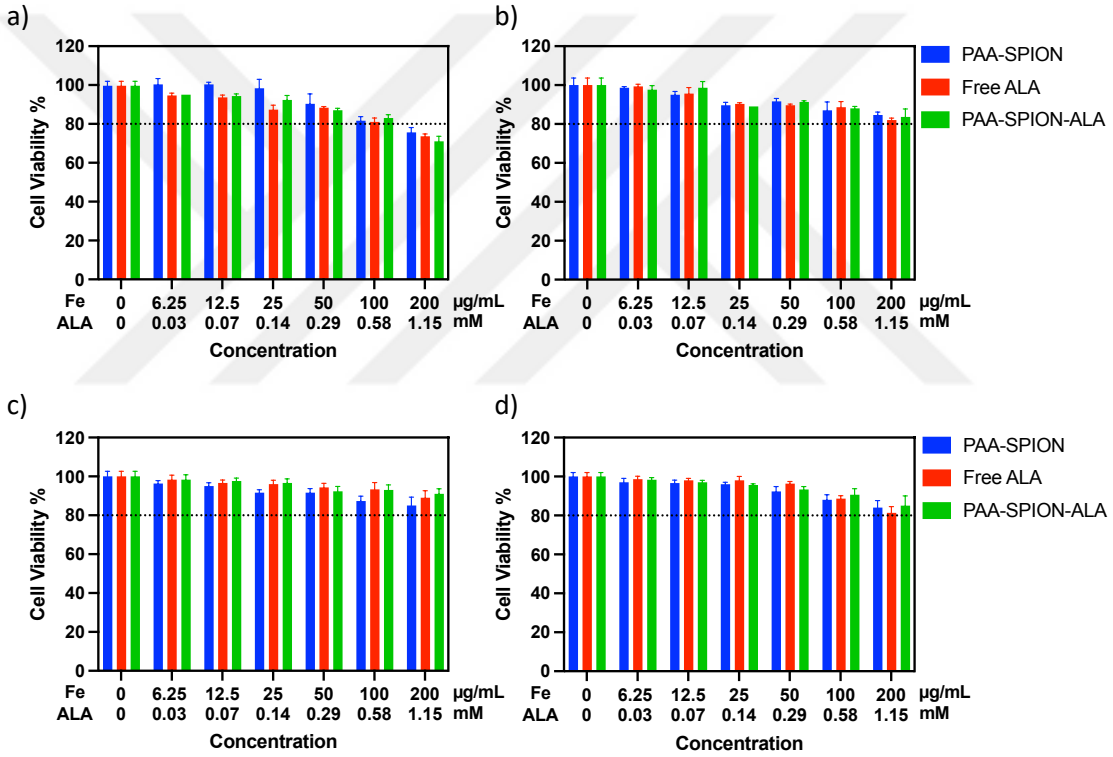

Figure 4.3 Viability of a) LNCaP, b) PC3, c) DU145, and d) L929 cells treated with free ALA, PAA-SPION, and ALA-PAA-SPION as determined by MTT assay at 6.25-200 ug Fe/mL and 0.03-1.15 mM ALA concentrations

The internalization of PAA-SPION and ALA-PAA-SPION by PCa cells was quantified using ICP-MS after a 12-hour incubation at a 100 µg Fe/mL concentration. This relatively short incubation period allows for assessing selectivity between free ALA and ALA-loaded SPIONs across different PCa cell lines.

ALA-PAA-SPION-treated LNCaP cells showed a threefold increase in Fe content compared to those treated with PAA-SPION alone, with uptake levels rising from approximately 21% to 66% (Figure 4.4a). Similarly, PC3 cells displayed an increase in nanoparticle uptake from 27% to 56% following ALA loading. In contrast, DU145 cells did not exhibit significant differences in nanoparticle uptake between PAA-SPION and ALA-PAA-SPION treatments.

This trend in nanoparticle uptake across cell lines likely correlates with the expression levels of PEPT1 and PEPT2 transporters [157]. Studies on the expression profile and activity of PEPT1 and PEPT2 transporters done by Tai et al. demonstrate that LNCaP cells express a high level of PEPT1, while PC3 cells express a high level of PEPT2 [157]. Du145 cells, on the other side, have a weak expression of PEPT1. In this study, a fluorescent dipeptide probe was used as a substrate of peptide transporters, and the substrate accumulated in the cytoplasm of LNCaP and PC3 cells selectively but not in Du145 cells.

LNCaP cells, which express high levels of PEPT2, demonstrated substantial uptake of ALA-functionalized SPIONs, while PC3 cells, characterized by high PEPT1 expression, also showed notably increased internalization. Our findings suggest that loading 5-ALA to SPIONs enhances transporter-mediated uptake and results in more efficient internalization in cells where these transporters are overexpressed. In contrast, limited uptake was observed in the cell line with lower PEPT1 and PEPT2 expression levels.

Additionally, PpIX generation was evaluated in PCa cells following a 12-hour incubation with PAA-SPION, free ALA, and ALA-PAA-SPION (Figure 4.4b). Since the effective conversion of ALA to PpIX is crucial for successful photodynamic therapy (PDT), the substantial increase in fluorescence intensity across all cell lines, especially in LNCaP and PC3, indicates enhanced ALA delivery via SPIONs. As expected, PpIX generation was absent in cells treated with PAA-SPION, confirming the presence of ALA for this conversion.

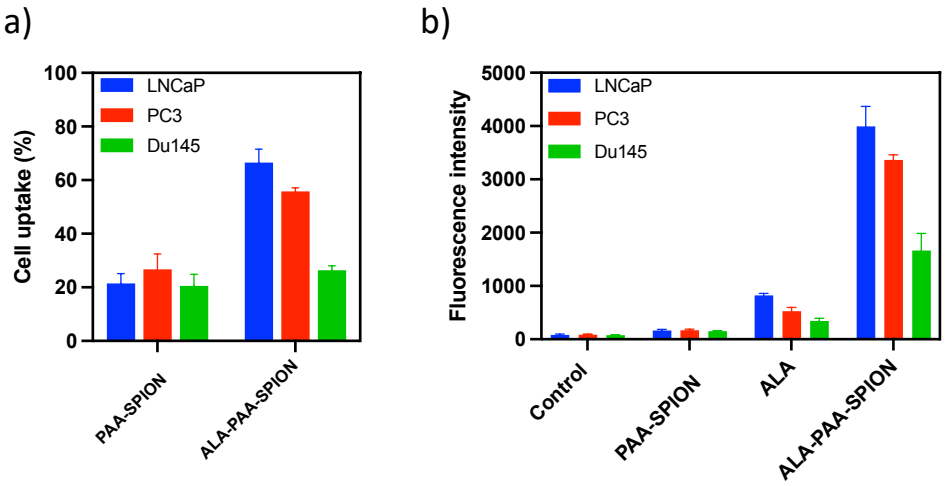

Figure 4.4 (a) Intracellular quantification of PAA-SPION and ALA-PAA-SPION NPs in LNCaP, PC3, and Du145 at 100 µg/mL Fe and 0.58 mM ALA for 12 h. (b) Intracellular PpIX formation in LNCaP, PC3, and Du145 cells after 12 h of incubation with free ALA or PAA-SPION and ALA-PAA-SPION NPs at 100 µg/mL Fe and 0.58 mM ALA for 12 h (PpIX: λex/λem = 420/635 nm).

The effects of PTT and PDT as both single and combined treatments were evaluated in PCa cells at four concentrations using 640 nm laser irradiation at 2.6 W/cm². Cells were pre-treated with PAA-SPION, free ALA, and ALA-PAA-SPION for 12 hours at concentrations ranging from 25 to 200 µg Fe/mL for nanoparticles and from 0.14 to 1.15 mM for free ALA, equivalent to the ALA content in ALA-PAA-SPION. Laser irradiation alone caused no cell death, confirming the safety of the protocol.

Single PTT and single PDT treatments at higher doses showed limited reductions in PCa cell viability. At the same time, the combined PTT and PDT approach induced significant cell death across the tested range, with the most pronounced effects observed in LNCaP and PC3 cell lines due to enhanced internalization. Notably, in LNCaP cells, single PTT or PDT at 200 µg Fe/mL or 1.15 mM ALA reduced cell viability to only 70-60% (Figure 4.5a). In contrast, the combined approach yielded substantial reductions even at lower doses, with viability dropping to 33%, 20%, and 6% at 50, 100, and 200 µg Fe/mL (0.29, 0.58, and 1.15 mM ALA). Similarly, PC3 cells showed viability reductions to 80% and 42% under single PTT and PDT at the highest dose (Figure 4.5b). In combination therapy, cell viability fell to 56%, 42%, and 10% at 50, 100, and 200 µg Fe/mL (0.29, 0.58, and 1.15 mM ALA), respectively. In contrast, the combination therapy had a less significant effect on Du145 cells, with a maximum viability reduction of 38% at the highest nanoparticle concentration (Figure 4.5c).

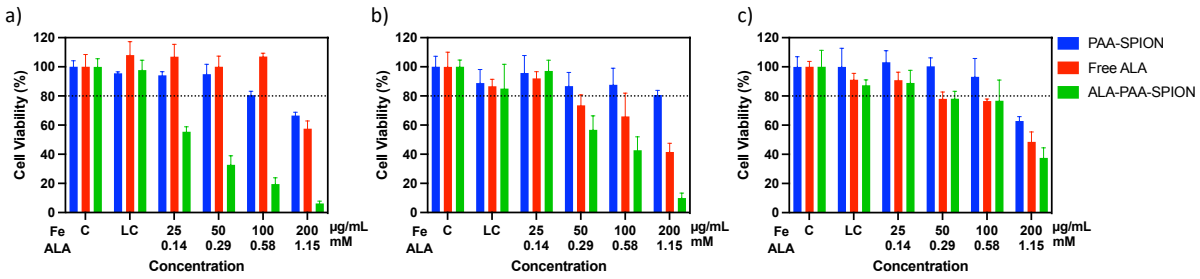

Figure 4.5 Dose-dependent viability of (a) LNCaP, (b) PC3, and (c) Du145 cells treated with PAA-SPION, ALA, and ALA-SPION irradiated at 640 nm for 10 min.

4.4.3 Intracellular ROS Generation

The production of reactive oxygen species (ROS), a potential contributor to cell death, was evaluated on the LNCaP cell line at 100 µg Fe/mL or 0.58 mM ALA with and without laser treatment and measured using flow cytometry (Figure 4.6). The metric M2 represents the percentage of cells exhibiting elevated ROS levels. In the absence of laser irradiation, no ROS production was detected across any treatment conditions, including laser-only or PAA-SPION with laser. However, free ALA-treated LNCaP cells showed an M2 level of approximately 20% upon laser activation, indicating that a subset of LNCaP cells is inherently responsive to ALA, producing ROS upon irradiation. ALA-PAA-SPION treatment also raised the levels of M2 by about 33%, consistent with the increased nanoparticle uptake and enhanced cell death in combination therapy. This correlation underscores the effectiveness of ALA-functionalized nanoparticles to increase ROS generation and augment cell death when combined with PTT.

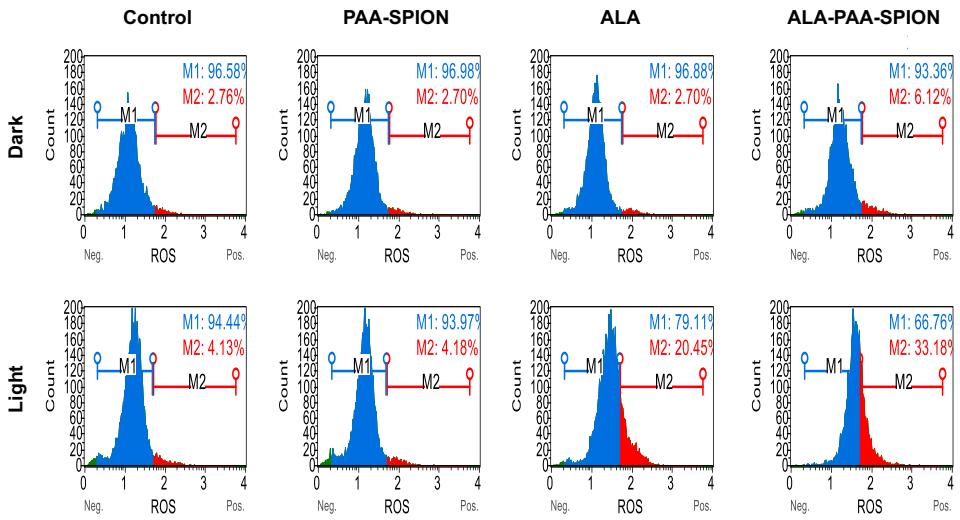

Figure 4.6 ROS generation in PAA-SPION, free ALA, and ALA-PAA-SPION treated LNCaP cells with and without laser irradiation at 100 ug Fe/mL and 0.58 ALA concentration determined by flow cytometry (640 nm, 10 min).

4.4.4 Cell Death Mechanism

Apoptotic cell death in LNCaP cells was evaluated at 100 µg Fe/mL or 0.58 mM ALA, with and without laser treatment, using a Caspase 3/7 assay (Figure 4.7). The Caspase 3/7 assay detects the activity of caspases involved in the execution phase of apoptosis, indicating the degree of apoptotic cell death [213]. At this concentration, no dark toxicity was observed for LNCaP cells. However, with laser treatment, the combination therapy group exhibited a marked decrease in cell viability to 6% as measured by the MTT assay. Figure 6 demonstrates that the treatment materials alone do not induce cell death without laser activation.

Upon combination therapy, a significant reduction in the live cell population was evident, with the dead cell population reaching 35% and the apoptotic/dead cell population reaching 49%. This apoptosis was further validated by an annexin V assay (Figure 4.8), which binds phosphatidylserine on the cell surface, marking early apoptotic cells [214]. In line with the Caspase 3/7 results, over 90% of cells remained viable across all non-laser conditions, including laser-only or PAA-SPION with laser treatments. In contrast, the free ALA-treated group showed a slight reduction in live cell population to around 86%, with early apoptotic and late apoptotic/dead populations at 9% and 3%, respectively. For the laser-treated ALA-PAA-SPION group, a substantial drop in the live population was observed, decreasing to 24%. In comparison, late apoptotic/dead and dead cells rose to approximately 52% and 22%, respectively.

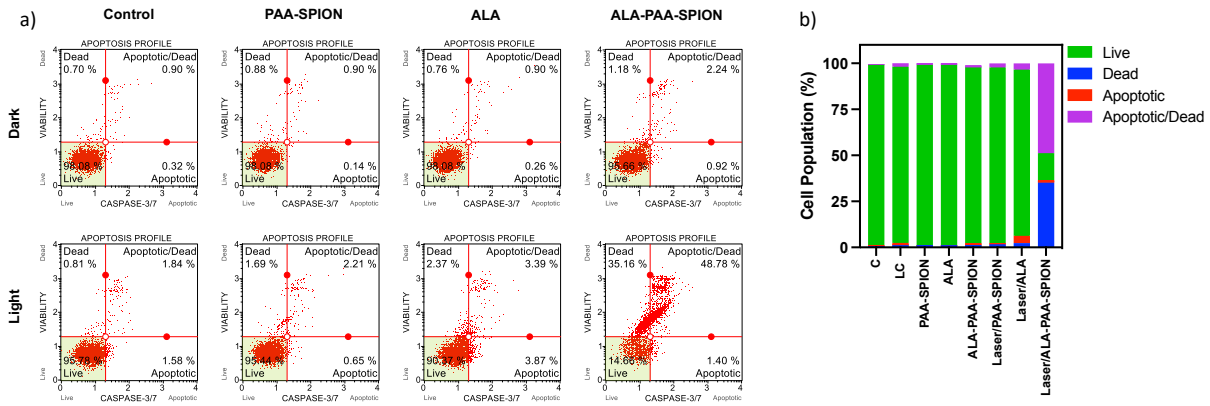

Figure 4.7 (a) Caspase 3/7 activity of LNCaP cells treated with PAA-SPION, ALA, and ALA-PAA-SPION at 100 µg/mL Fe (0.58 mM ALA) with and without laser irradiation determined by flow cytometry (640 nm, 10 min). (b) Summary of LNCaP cell populations after treatment.

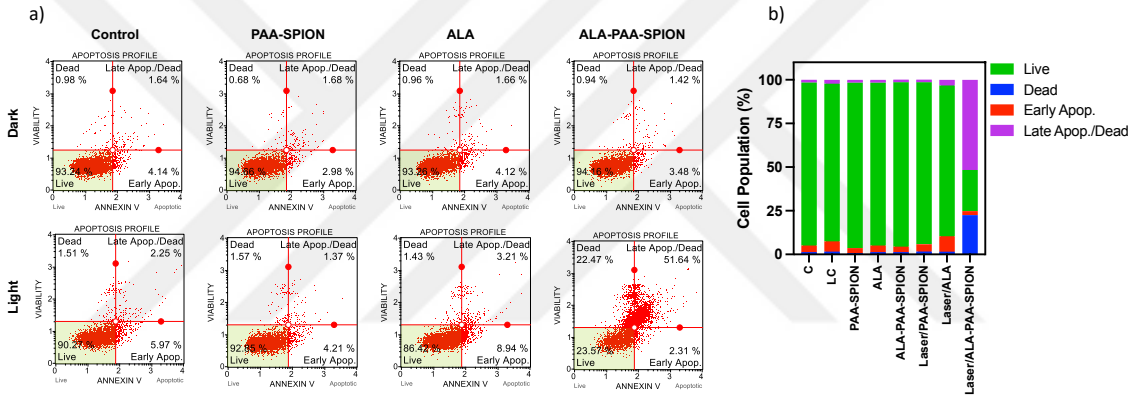

Figure 4.8 (a) Annexin V/dead cell profiles of LNCaP cells treated with PAA-SPION, ALA, and ALA-PAA-SPION at 100 µg/mL Fe (0.58 mM ALA) with and without laser irradiation determined by flow cytometry (640 nm, 10 min). (b) Summary of LNCaP cell populations after treatment.

During apoptosis, cellular signals frequently lead to a loss of mitochondrial membrane potential (Δψm), a process known as mitochondrial depolarization [215, 216], which is a hallmark of cell death pathways study, LNCaP cells treated with 100 µg Fe/mL or 0.58 mM ALA, with and without laser activation, were analyzed for changes in Δψm. As shown in Figure 4.9, treatment with PAA-SPION, free ALA, and ALA-PAA-SPION alone (without laser) did not induce significant mitochondrial depolarization. However, ALA-PAA-SPION-treated laser-irradiated LNCaP cells exhibited significant depolarization, affecting approximately 84% of cells. This high level of depolarization on combination with ALA-PAA-SPION and laser treatment reflects the breakdown of mitochondrial membrane integrity, which is an important step in apoptosis induction.

This loss of Δψm most likely involves the activation of downstream apoptosis pathways, confirming the efficacy of ALA-PAA-SPION to cause effective cell death under controlled laser irradiation.

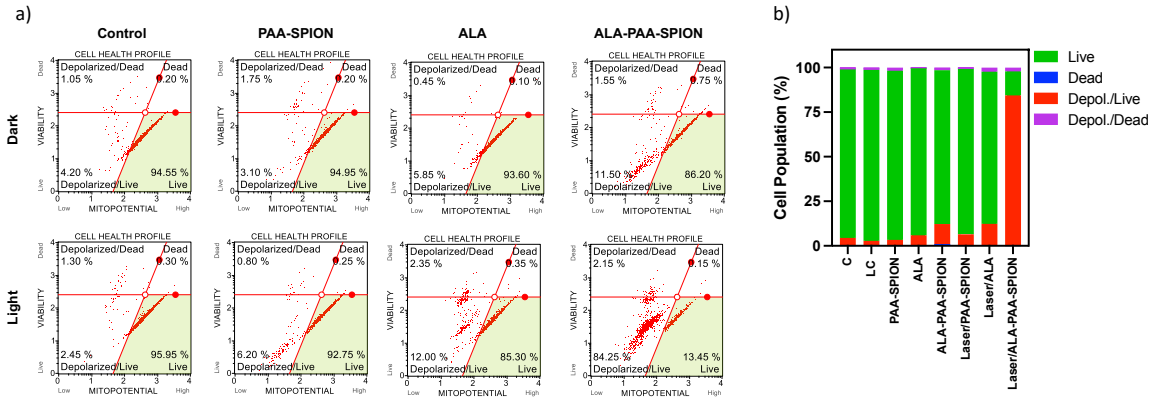

Figure 4.9 (a) Mitochondrial membrane potential of LNCaP cells treated with PAA-SPION, ALA, and ALA-PAA-SPION at 100 µg/mL Fe (0.58 mM ALA) with and without laser irradiation determined by flow cytometry (640 nm, 10 min). (b) Summary of LNCaP cell populations after treatment.

4.5 Conclusion

This study presents a promising approach to prostate cancer treatment through the use of ALA-PAA-SPIONs for combined photothermal and photodynamic therapy. By promoting the selective uptake of 5-ALA, these nanoparticles achieve enhanced accumulation in prostate cancer cells, resulting in significant cell death upon laser irradiation. The dual-mode treatment was highly effective in vitro, especially in LNCaP and PC3 cells, where the PEPT1 and PEPT2 transporters are expressed in high levels. The combination therapy offers a reduced treatment dose compared to single-mode treatments, thus demonstrating its effectiveness in minimizing side effects and attaining maximum therapeutic gain. Our findings show that ALA-PAA-SPIONs are a promising targeted phototherapy therapy for prostate cancer, warranting further investigation in preclinical and clinical models to optimize their therapeutic potential.

Chapter 5: Conclusion and Future Perspectives

5.1 Conclusion

Cancer is a massive threat to public health and the economy due to the rising number of cases and concerning survival rates. Theranostic nanoparticles offer powerful alternative approaches to realize remarkable achievements in cancer treatment. Nanoparticles may combine conventional treatments (e.g., radiotherapy, chemotherapy) with next-generation treatment modalities (e.g., phototherapies) and imaging modalities, improving specificity, locality, and efficacy of the treatment and offering an opportunity to monitor the direct outcome of the treatment. The ideal theranostic nanoparticle would selectively target the cancer cells, improve the diagnostic and therapeutic effect locally, and be eliminated naturally without significant harm to healthy tissues.

This thesis mainly focused on theranostic GGS nanoparticles as a new class of nanoparticles with potential in diagnosis/tracking via PAI and/or CT and with great potential as therapeutics due to high-Z Au atoms providing radiosensitization in RT and strong NIR absorption for PTT; hence as a unique nanoparticle allowing combination therapy, RT and PTT, under imaging and mild conditions.

The first chapter demonstrated significant radiotoxicity at radiation dose at and below 4Gy via GGS-sensitization of tumor cells. Further improvement in therapy by combining RT with an emerging treatment modality, radiodynamic therapy (RDT), was demonstrated successfully. ALA-loaded bPEI-GGS nanoparticles provided enhanced stability, bioavailability, and controlled ALA release, improving intracellular PpIX generation and efficient ROS production upon low-dose X-ray irradiation. The use of X-ray and GGS-producing Cherenkov radiation capable of activating PpIX bypassed the typical penetration depth limitation of blue-red light in ALA-PDT. In vitro studies performed on PC3 and MDA-MB-231 cell lines showed dramatic radiotoxicity even at 0.5 Gy with a low dose of ALA-GGS (Au concentration (μg/ml)/ALA concentration (mM): 25/0.22) in both cell lines. The combination therapy was more efficient in PC3 cells due to the targeting action of ALA on PEPT1/PEPT2 overexpressing PC3 prostate cancer cell lines, which significantly increased apoptotic cell death, DNA damage, and autophagy. Inhibition of autophagy prevented cell death in PC3 cells, demonstrating its critical role in the therapeutic effect. MDA-MB-231 cells were shown to be more resistant to therapy, as indicated in the literature, but the combination therapy successfully killed

these cells, too. Yet, the mechanism of cell death differs from those detected for PC3 and needs further investigation. Overall, the RT/RDT combination therapy provided greater toxicity to tumor cells than ALA-RDT or GGS-RT under low-dose radiation, which was otherwise safe at low doses of the agents, proving the original hypothesis of this thesis. X-ray to deliver RT/RDT is especially valuable for treating deep-seated and/or large tumors bypassing penetration depth challenges of PDT. Hence, the material designed and the method offered here have great potential to improve therapeutic outcomes while minimizing/eliminating potential side effects in the fight against cancer.

The second part of the thesis demonstrated the potential of GGS nanoparticles as the sole multifunctional theranostic agent delivering combination therapy on its own, exploiting its high-Z Au content as a radiosensitizer and NIR absorbance for PTT. Folic acid-functionalized anionic GGS (FA-3MPA-GGS) nanoparticles were developed to provide selective treatment to FR(+) tumors as a proof of concept, which may be adopted for other types of tumors with specific surface receptors. These nanoparticles exhibited strong NIR absorption, high photothermal conversion efficiency (76%), and effective radiosensitization, enabling their use in PAI, PTT, and RT. Functionalization with folic acid increased their accumulation in FR(+) cancer cells by 2.3-fold in HeLa and 1.6-fold in MDA-MB-231 cells compared to FR(–) A549 cells. Such selective accumulation provided almost complete loss of viability of FR(+) cancer cells exposed to PTT/RT combination therapy at 200 μg Au/mL concentration with 795 nm (1 W) laser irradiation for 10 min, followed by 0.5 Gy X-ray exposure. ROS generation increased up to 3.7-fold in FA-3MPA-GGS-treated HeLa cells under PTT/RT conditions, and LDH assays confirmed membrane disruption as a key cell death mechanism. Combination therapy provided a stronger therapeutic outcome than either the PTT or RT, supporting the original hypothesis of the thesis: Mild PTT sensitized tumor cells for RT, allowing reduction of X-ray dose and maximizing the radiotoxicity. Both the material designed and the PTT/RT delivery with GGS at low doses of the agent and the radiation coupled with receptor targeting and imaging modality brought out a new material and approach for a minimally invasive and efficient strategy for precision treatment of cancer.

The third and last chapter focused on a combination of PTT and PDT for improved treatment of prostate cancer cells via ALA-loaded superparamagnetic iron oxide nanoparticles irradiated at a single wavelength. SPIONs are effective PTT agents under NIR irradiation and may be delivered selectively to PEPT1/PEPT2 overexpressing cell lines due to surface-residing ALA molecules. SPIONs stabilized ALA and improved their

bioavailability, maximizing ALA-PDT efficiency in the cancer cells. ALA-PDT and SPION-PTT were tested at a single wavelength, 640 nm, for practical clinic translation of the strategy. Red-light ALA-PDT is not considered as effective as blue-light ALA-PDT due to the lower absorbance of red-light by PpIX, but the combination with PTT improved the red-light PDT. SPION-PTT triggered in red instead of NIR laser provided simplicity for the combination therapy, otherwise requiring dual irradiation, one at 640 nm and another at 808 nm. In vitro studies on LNCaP, PC3, and DU145 prostate cancer cell lines demonstrated increased nanoparticle uptake, elevated ROS generation, apoptosis, and mitochondrial membrane depolarization, and near complete cell death after 640 nm laser irradiation at 2.6 W/cm² in LNCaP and PC3 cells, which overexpress PEPT1 and PEPT2. DU145 cells exhibited lower sensitivity, likely due to reduced transporter expression. Overall, ALA-PAA-SPIONs show promising results for a prostate cancer portfolio as a targeted combinational red-light phototherapy, offering improved treatment specificity and reduced systemic toxicity.

GGS nanoparticles are relatively new in the literature. Previously, these nanoparticles were unsuitable for biomedical applications because they lacked stability and tended to aggregate quickly. Our group first studied enhancing the colloidal stability of GGS. Functional coatings protect the properties of GGS for up to one year and allow further functionalization of the nanoparticles for cancer theranostics. One drawback of GGS for biomedical applications is the polydispersity of anisotropic nanoparticles. For in vivo tests, the shape-dependent biodistribution of the nanoparticles will be critical. Also, different shapes of GGS may show different properties upon treatment. Therefore, it is essential to investigate the shape-dependent properties and separation of the nanoparticles for further studies.

This thesis opens up a new platform in cancer treatment, imaging, and imaging-guided therapy but offers a good alternative to gold nanoparticles. GGS effectively reduces the dose of ionizing X-ray and offers opportunities for enhancement of RDT and PTT. This thesis gives insights into combinatory approaches in cancer theranostics. Especially radiodynamic therapy is a simple, innovative strategy to enhance the effect of radiotherapy. Of course, GGS can be combined with other conventional photosensitizers and with other tumor-specific ligands for different cancer types. *In vivo* biosafety studies are also needed to understand the biodistribution and long-term toxicity assessment of the GGS.

These projects are partially funded by Project No: 119F319 (PI: Prof. Burçin Ünlü) and partially with Project No: 22AG016.

*5.2 **Spin-off this thesis***

Gold-gold sulfide nanoparticles offer many advantages for cancer theranostics, such as radiosensitization, photothermal conversion, drug carrier potential, and PAI contrast agent potential, as mentioned in the previous chapters. One concern for the further application of GGS is the polydispersity of nanoparticles. GGS consists of small spherical and large non-spherical particles ranging in size and shape [189]. Non-spherical particles are mostly triangles, truncated triangles, pentagons, and cuboctahedrons. Even though these anisotropic nanoparticles are the key sources for NIR absorption, a mixture of differently shaped nanoparticles may raise some problems in the clinic. The uptake, biodistribution, toxicity, response to treatment (e.g., radiotherapy), and clearance of the nanoparticles vary with size and shape.

In this brief study, we tried to understand the response of cells when GGS is separated into small and large portions. Separation of all different shapes needs detailed research, but in this study, we separated the GGS into two groups by centrifugation. 6000 rpm and 3 cycles of centrifugation were used, and supernatant (small) and precipitate (large) particles were obtained. Figure 4.1A shows the absorbance change of the GGS when it is separated. The small-spherical portion only exhibits an SPR peak of around 530 nm, while the large portion has absorbance at 525 and 740 nm. The NIR absorbance intensity of the large particles enhanced compared to the primary GGS solution due to the higher concentration of anisotropic nanoparticles. TEM images confirmed that the rough separation of GGS has been achieved (Figure 5.1B). However, small and large GGS portions also contain the other portion. This distribution did not change the hydrodynamic size of small and large nanoparticles compared to the primary solution (Table 5.1). This may be due to the presence of large particles in both solutions shown by TEM, and DLS cannot detect the exact size distribution.

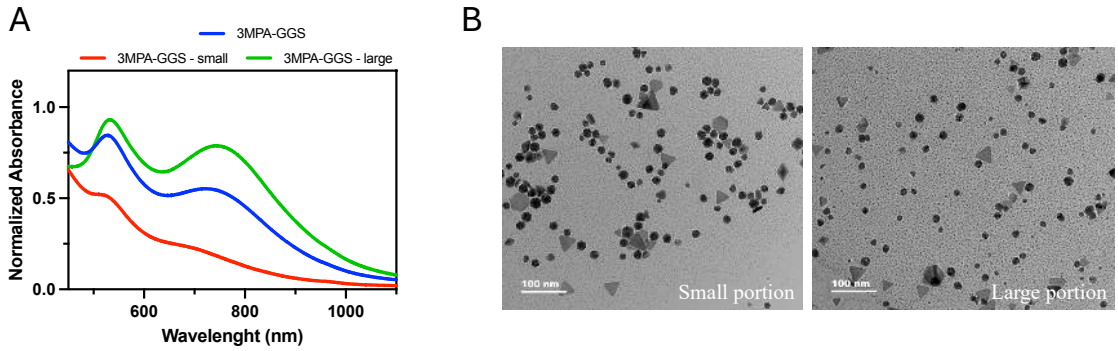

Figure 5.1 A) Absorbance of the primary 3MPA-GGS solution and separated portions of 3MPA-GGS after centrifugation. B) TEM images of separated 3MPA-GGS.

Table 5.1 Hydrodynamic size and zeta potentials of separated 3MPA-GGS portions.

Nanoparticle	Zeta Potential (mV)	Dh-Intensity (nm)	Dh-Number (nm)
3MPA-GGS	-31 mV	75.79 nm (88.6%), 2.80 nm (8.9%)	1.59 nm
3MPA-GGS small	-23.6 mV	73.1 nm (94.4%), 2.39 nm (5.6%)	1.69 nm
3MPA-GGS big	-29.6 mV	75.06 nm (83.8%), 2.15 nm (8.7%), 5.73 nm (5.4%)	1.26 nm

The internalization of primary, small, and large 3MPA-GGS by MDA-MB-231 cells was quantitatively detected by absorbance measurement. Since small NPs have absorbance at 525 nm and large ones at 525 and 740 nm, the absorbance measurement was done at these two wavelengths. Standard curves of NPs were prepared by known concentration and absorbance. Then, the absorbance of the cells incubated with NPs was measured. Small particles internalized around 4 times more than the primary 3MPA-GGS solution at 290 µg Au/mL concentration (Figure 5.2A). Larger nanoparticles, on the other hand, have the least uptake; only half of the primary GGS internalization was measured for a large portion of GGS (Figure 5.2A).

MDA-MB-231 cells were exposed to a 0.5 Gy X-ray dose after 24 hours of incubation with nanoparticles at concentrations ranging from 50 to 300 µg Au/mL. Control groups exposed to X-ray irradiation had no loss in viability below 80%. Cell viability decreased to 66% with primary 3MPA-GGS at 300 µg Au/mL (Figure 5.2B). With large 3MPA-GGS, viability was reduced to 48%. The small portion of GGS did not affect the cell viability significantly, keeping the viability at 90%. These results indicate that although small particles have very high cellular uptake, large particles affect

radiosensitization more. 0.5 Gy, single-dose X-ray treatment with large-anisotropic 3MPA-GGS can reduce cell viability to IC50 levels.

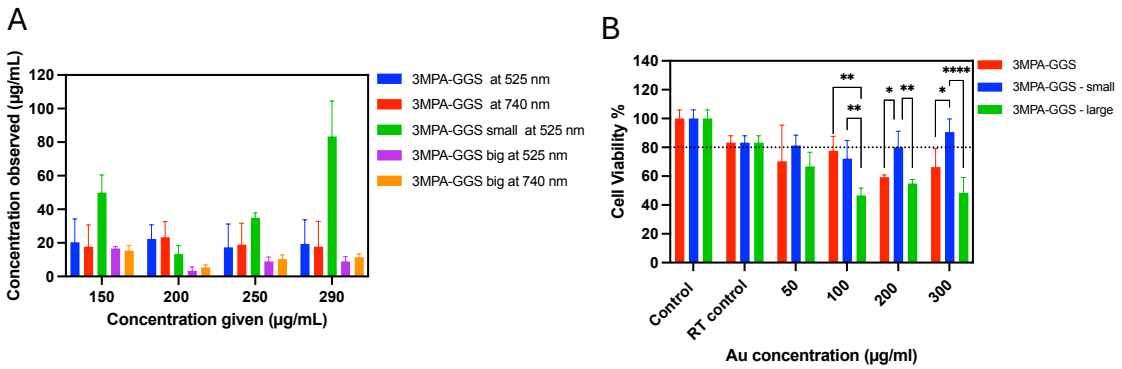

Figure 5.2 A) Cellular uptake of the MDA-MB-231 cells treated with separated GGS after 24 h incubation. B) Dose-dependent viability of MDA-MB-231 cells treated with NPs exposed to 0.5 Gy irradiation. (0.0332 (*), 0.0021 (**), 0.002 (***), <0.001 (****)).

The heating potential of a large portion of 3MPA-GGS was investigated under continuous fiber-coupled laser diode laser irradiation at 808 nm using 215 mW power. Nanoparticle solutions of 50, 100, and 200 µg Au/mL concentrations were irradiated for 30 minutes, and the temperature increase was followed using a thermocouple. 200 µg Au/mL concentrations increased the solution temperature by 17.5 °C (Figure 5.3A). Significant temperature increases in the NP solutions show the strong PTT potential of GGS. Compared to the heating potential of the primary 3MPA-GGS solution discussed in Chapter 3 (Figure 3.3), the ΔT between the primary and large particles solution is around 1 °C. Moreover, to demonstrate the photostability of NPs, three cycles of on/off irradiation experiments were performed (Figure 5.3B). NPs had the same ΔT after each heating and cooling cycle. This shows the photostability of GGS after multiple laser irradiations.

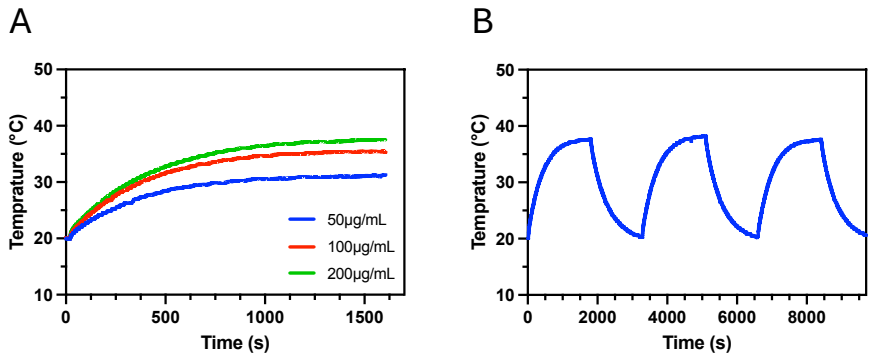

Figure 5.3 A) Conversion of light to heat by the large anisotropic 3MPA-GGS nanoparticle solutions at 50-200 µg/ Au/mL concentrations under 808 nm irradiation (215 mW). B) Time-dependent change in the temperature of 3MPA-GGS and FA-3MPA-GGS solutions after laser on/off cycles (200 µg/mL, 808nm, 215 mW).

In conclusion, a rough separation of 3MPA-GGS was achieved, and the size separation of small spherical and large anisotropic portions was confirmed by absorbance change and TEM images. The uptake experiments done on MDA-MB-231 cells show small nanoparticles internalized more than large ones. However, larger nanoparticles seem to be the source of radiosensitization. 0.5 Gy low-dose radiotherapy treatment showed that large GGS can reduce the MDA-MB-231 cell viability to IC50. Solution heating experiments with large NPs demonstrated the high heating potential and photostability at 808 nm laser irradiation. These findings showed that GGS may show different properties depending on the size, and further research is needed to obtain monodisperse GGS nanoparticles.

The author designed the research described in this spin-off section, and the experiments were performed by Ali Ekber Avşar.

*5.3 **Publications and Conferences***

5.3.1 Publications

- Demir, M., Çizmeciyan, M. N., Sipahioğlu, D., Khoshzaban, A., Ünlü, M. B., & Acar, H. Y. (2025). Portfolio of colloidally stable gold–gold sulfide nanoparticles and their use in broad-band photoacoustic imaging. Nanoscale, 17(3), 1371-1380.

- Demir, M., Akkoç, Y., Avşar, A. E., Sezen, D., Selek, U., Gözüaçık, D., & Acar, H. Y. Gold-Gold Sulfide Nanoparticles for X-ray-Activated ALA-Based Radiodynamic Therapy in Cancer Cells. (in preparation)
- Demir, M., Çizmeciyan, M.N., Acar, İ., Avşar, Ali E., Morova, Y., Sennaroğlu, A., Ünlü, M. B., & Acar, H. Y. Targeted Gold-Gold Sulfide Nanoparticles for Photoacoustic Imaging and Enhanced PTT/RT Combination Therapy. (in preparation)
- Demir, M., Genel, M. E., Çakıroğlu, I., Kasapoğlu, T., Ulukaya, E., Sennaroğlu, A., Acar, H. Y. & Onbaşlı, K. Targeted Dual-mode Phototherapy of Prostate Cancer with ALA-loaded SPIONs. (in preparation)

5.3.2 Conferences

- Demir, M., Çizmeciyan, M. N., Sipahioğlu, D., Ünlü, M. B., & Acar, H. Y. (2023). Development of Gold Chalcogenides for Photoacoustic Imaging. 19th Asian Chemical Congress. *Poster presentation.*
- Demir, M., Avşar, A. E., Sezen, D., Selek, U., & Acar, H. Y. (2023). 5-ALA Mediated PDT/Radiotherapy Combination for Breast Cancer Using Gold Chalcogenides. 20th Congress of European Society for Photobiology. *Poster presentation.*
- COST Short-term Scientific Mission, University of York, Department of Chemistry (2024). Antimicrobial photodynamic therapy (aPDT) with gold/gold sulfide.
- Demir, M., Çizmeciyan, M.N., Acar, İ., Avşar, Ali E., Ünlü, M. B., & Acar, H. Y. (2024). Gold sulfide nanoparticles for image-guided long wavelength photothermal-/radio- combination therapy using folate receptor targeting. Photodynamic Therapy and Photodiagnosis Update 2024. *Oral presentation.*

BIBLIOGRAPHY

1. Alba-Molina, D., J.J. Giner-Casares, and M. Cano, *Bioconjugated plasmonic nanoparticles for enhanced skin penetration.* Surface-modified Nanobiomaterials for Electrochemical and Biomedicine Applications, 2020: p. 219-235.
2. Chung, D., J. Kim, and J. Kim, *Evaluation of MTT and Trypan Blue assays for radiation-induced cell viability test in HepG2 cells.* International Journal of Radiation Research, 2015. **13**(4): p. 331.
3. Loeve, S., *About a definition of nano: how to articulate nano and technology.* HYLE–International Journal for Philosophy of Chemistry, 2010. **16**(1): p. 3-18.
4. Bellucci, S., *Nanoparticles and Nanodevices in Biological Applications: The INFN Lectures-Vol I*. Vol. 4. 2008: Springer Science & Business Media.
5. Byakodi, M., et al., *Emerging 0D, 1D, 2D, and 3D nanostructures for efficient point-of-care biosensing.* Biosensors and Bioelectronics: X, 2022. **12**: p. 100284.
6. Eker, F., et al., *A comprehensive review of nanoparticles: from classification to application and toxicity.* Molecules, 2024. **29**(15): p. 3482.
7. Abid, N., et al., *Synthesis of nanomaterials using various top-down and bottom-up approaches, influencing factors, advantages, and disadvantages: A review.* Advances in Colloid and Interface Science, 2022. **300**: p. 102597.
8. Biswas, A., et al., *Advances in top–down and bottom–up surface nanofabrication: Techniques, applications & future prospects.* Advances in colloid and interface science, 2012. **170**(1-2): p. 2-27.
9. Nabavifard, S., et al., *Application of dendrimer/gold nanoparticles in cancer therapy: a review.* Journal of Inorganic and Organometallic Polymers and Materials, 2020. **30**: p. 4231-4244.
10. Kunz, S., *Colloidal synthesis methods for the preparation of supported nanoparticles.* 2018.
11. Moore, T.L., et al., *Nanoparticle colloidal stability in cell culture media and impact on cellular interactions.* Chemical Society Reviews, 2015. **44**(17): p. 6287-6305.
12. Gregory, J., *Approximate expressions for retarded van der Waals interaction.* Journal of colloid and interface science, 1981. **83**(1): p. 138-145.
13. Matter, F., A.L. Luna, and M. Niederberger, *From colloidal dispersions to aerogels: How to master nanoparticle gelation.* Nano Today, 2020. **30**: p. 100827.
14. Freestone, I., et al., *The Lycurgus cup—a roman nanotechnology.* Gold bulletin, 2007. **40**: p. 270-277.
15. Louis, C. and O. Pluchery, *Gold nanoparticles for physics, chemistry and biology*. 2017: World Scientific.
16. Cobley, C.M., et al., *Gold nanostructures: a class of multifunctional materials for biomedical applications.* Chemical Society Reviews, 2011. **40**(1): p. 44-56.
17. Xia, K., et al., *Preparation of gold nanorods and their applications in photothermal therapy.* Journal of nanoscience and nanotechnology, 2015. **15**(1): p. 63-73.
18. Dreaden, E.C., et al., *The golden age: gold nanoparticles for biomedicine.* Chem Soc Rev, 2012. **41**(7): p. 2740-79.
19. Puddephatt, R., *The Chemistry of Gold. Elsevier Scientific, Amsterdam.* 1978.
20. Ghosh, P., et al., *Gold nanoparticles in delivery applications.* Advanced drug delivery reviews, 2008. **60**(11): p. 1307-1315.

21. Cho, E.C., et al., *A quantitative analysis of the fate of Au nanocages after uptake by U87-MG tumor cells under both in vitro and in vivo conditions.* Angewandte Chemie (International ed. in English), 2012. **52**(4): p. 1152.
22. Cho, E.C., Q. Zhang, and Y. Xia, *The effect of sedimentation and diffusion on cellular uptake of gold nanoparticles.* Nature nanotechnology, 2011. **6**(6): p. 385-391.
23. Yang, X., et al., *Gold nanomaterials at work in biomedicine.* Chemical reviews, 2015. **115**(19): p. 10410-10488.
24. Zeng, S., et al., *A review on functionalized gold nanoparticles for biosensing applications.* Plasmonics, 2011. **6**: p. 491-506.
25. Frangioni, J.V., *In vivo near-infrared fluorescence imaging.* Curr Opin Chem Biol, 2003. **7**(5): p. 626-34.
26. Shanmugam, V., S. Selvakumar, and C.-S. Yeh, *Near-infrared light-responsive nanomaterials in cancer therapeutics.* Chemical Society Reviews, 2014. **43**(17): p. 6254-6287.
27. Svaasand, L.O., C.J. Gomer, and E. Morinelli, *On the physical rationale of laser induced hyperthermia.* Lasers in Medical Science, 1990. **5**: p. 121-128.
28. Zhang, W., et al., *pH and near-infrared light dual-stimuli responsive drug delivery using DNA-conjugated gold nanorods for effective treatment of multidrug resistant cancer cells.* Journal of Controlled Release, 2016. **232**: p. 9-19.
29. Narang, J., et al., *Electrochemical impediometric detection of anti-HIV drug taking gold nanorods as a sensing interface.* Biosensors and Bioelectronics, 2015. **66**: p. 332-337.
30. Her, S., D.A. Jaffray, and C. Allen, *Gold nanoparticles for applications in cancer radiotherapy: Mechanisms and recent advancements.* Advanced drug delivery reviews, 2017. **109**: p. 84-101.
31. Lusic, H. and M.W. Grinstaff, *X-ray-computed tomography contrast agents.* Chemical reviews, 2013. **113**(3): p. 1641-1666.
32. Wang, Y., et al., *Evaluating the pharmacokinetics and in vivo cancer targeting capability of Au nanocages by positron emission tomography imaging.* Acs Nano, 2012. **6**(7): p. 5880-5888.
33. Jackson, P.A., et al., *Potential dependent superiority of gold nanoparticles in comparison to iodinated contrast agents.* European journal of radiology, 2010. **75**(1): p. 104-109.
34. Hainfeld, J.F., D.N. Slatkin, and H.M. Smilowitz, *The use of gold nanoparticles to enhance radiotherapy in mice.* Physics in Medicine & Biology, 2004. **49**(18): p. N309.
35. Liu, Y., et al., *Metal-based nanoenhancers for future radiotherapy: radiosensitizing and synergistic effects on tumor cells.* Theranostics, 2018. **8**(7): p. 1824.
36. Chen, Y., et al., *Gold nanoparticles as radiosensitizers in cancer radiotherapy.* International Journal of Nanomedicine, 2020. **15**: p. 9407.
37. Butterworth, K.T., et al., *Radiosensitization by gold nanoparticles: effective at megavoltage energies and potential role of oxidative stress.* Translational Cancer Research, 2013. **2**(4).
38. Misawa, M. and J. Takahashi, *Generation of reactive oxygen species induced by gold nanoparticles under x-ray and UV Irradiations.* Nanomedicine: Nanotechnology, Biology and Medicine, 2011. **7**(5): p. 604-614.

39. Pawlik, T.M. and K. Keyomarsi, *Role of cell cycle in mediating sensitivity to radiotherapy.* International Journal of Radiation Oncology* Biology* Physics, 2004. **59**(4): p. 928-942.
40. Kastan, M.B. and J. Bartek, *Cell-cycle checkpoints and cancer.* Nature, 2004. **432**(7015): p. 316-323.
41. Roa, W., et al., *Gold nanoparticle sensitize radiotherapy of prostate cancer cells by regulation of the cell cycle.* Nanotechnology, 2009. **20**(37): p. 375101.
42. Geng, F., et al., *Thio-glucose bound gold nanoparticles enhance radio-cytotoxic targeting of ovarian cancer.* Nanotechnology, 2011. **22**(28): p. 285101.
43. Wang, C., et al., *Enhancement of radiation effect and increase of apoptosis in lung cancer cells by thio-glucose-bound gold nanoparticles at megavoltage radiation energies.* Journal of nanoparticle research, 2013. **15**: p. 1-12.
44. Cui, L., et al., *Hypoxia and cellular localization influence the radiosensitizing effect of gold nanoparticles (AuNPs) in breast cancer cells.* Radiation research, 2014. **182**(5): p. 475-488.
45. Pan, Y., et al., *Gold nanoparticles of diameter 1.4 nm trigger necrosis by oxidative stress and mitochondrial damage.* small, 2009. **5**(18): p. 2067-2076.
46. Choudhury, A., A. Cuddihy, and R.G. Bristow. *Radiation and new molecular agents part I: targeting ATM-ATR checkpoints, DNA repair, and the proteasome*. in *Seminars in radiation oncology*. 2006. Elsevier.
47. Chithrani, D.B., et al., *Gold nanoparticles as radiation sensitizers in cancer therapy.* Radiation research, 2010. **173**(6): p. 719-728.
48. Banáth, J.P. and P.L. Olive, *Expression of phosphorylated histone H2AX as a surrogate of cell killing by drugs that create DNA double-strand breaks.* Cancer research, 2003. **63**(15): p. 4347-4350.
49. Chen, N., et al., *BSA capped Au nanoparticle as an efficient sensitizer for glioblastoma tumor radiation therapy.* RSC Advances, 2015. **5**(51): p. 40514-40520.
50. Jain, S., et al., *Cell-specific radiosensitization by gold nanoparticles at megavoltage radiation energies.* International Journal of Radiation Oncology* Biology* Physics, 2011. **79**(2): p. 531-539.
51. Azzam, E.I., et al., *Oxidative metabolism modulates signal transduction and micronucleus formation in bystander cells from α-particle-irradiated normal human fibroblast cultures.* Cancer research, 2002. **62**(19): p. 5436-5442.
52. Azzam, E.I., S.M. De Toledo, and J.B. Little, *Oxidative metabolism, gap junctions and the ionizing radiation-induced bystander effect.* Oncogene, 2003. **22**(45): p. 7050-7057.
53. Zhang, A. and L. Gao, *The refined application and evolution of nanotechnology in enhancing radiosensitivity during radiotherapy: transitioning from gold nanoparticles to multifunctional nanomaterials.* International Journal of Nanomedicine, 2023: p. 6233-6256.
54. Zheng, Q., et al., *The role and mechanisms of nanoparticles to enhance radiosensitivity in hepatocellular cell.* Biomedicine & Pharmacotherapy, 2013. **67**(7): p. 569-575.
55. Parzych, K.R. and D.J. Klionsky, *An overview of autophagy: morphology, mechanism, and regulation.* Antioxidants & redox signaling, 2014. **20**(3): p. 460-473.
56. Levy, J.M.M., C.G. Towers, and A. Thorburn, *Targeting autophagy in cancer.* Nature Reviews Cancer, 2017. **17**(9): p. 528-542.

57. Ma, X., et al., *Gold nanoparticles induce autophagosome accumulation through size-dependent nanoparticle uptake and lysosome impairment.* ACS nano, 2011. **5**(11): p. 8629-8639.
58. Joshi, P., et al., *The anticancer activity of chloroquine-gold nanoparticles against MCF-7 breast cancer cells.* Colloids and Surfaces B: Biointerfaces, 2012. **95**: p. 195-200.
59. Ding, F., et al., *Overendocytosis of gold nanoparticles increases autophagy and apoptosis in hypoxic human renal proximal tubular cells.* International journal of nanomedicine, 2014: p. 4317-4330.
60. Luo, C.-l., et al., *The effect of quercetin nanoparticle on cervical cancer progression by inducing apoptosis, autophagy and anti-proliferation via JAK2 suppression.* Biomedicine & pharmacotherapy, 2016. **82**: p. 595-605.
61. Mosmann, T., *Rapid colorimetric assay for cellular growth and survival: application to proliferation and cytotoxicity assays.* Journal of immunological methods, 1983. **65**(1-2): p. 55-63.
62. Jauregui, H.O., et al., *Trypan blue dye uptake and lactate dehydrogenase in adult rat hepatocytes—freshly isolated cells, cell suspensions, and primary monolayer cultures.* In vitro, 1981. **17**(12): p. 1100-1110.
63. Zhu, H., et al., *Recent progress in the development of near-infrared organic photothermal and photodynamic nanotherapeutics.* Biomaterials science, 2018. **6**(4): p. 746-765.
64. Abadeer, N.S. and C.J. Murphy, *Recent progress in cancer thermal therapy using gold nanoparticles.* Nanomaterials and Neoplasms, 2021: p. 143-217.
65. Liu, Y.J., et al., *Photothermal therapy and photoacoustic imaging via nanotheranostics in fighting cancer.* Chemical Society Reviews, 2019. **48**(7): p. 2053-2108.
66. Li, J., et al., *Nanoparticles-based phototherapy systems for cancer treatment: Current status and clinical potential.* Bioactive Materials, 2023. **23**: p. 471-507.
67. Li, X., et al., *Clinical development and potential of photothermal and photodynamic therapies for cancer.* Nature reviews Clinical oncology, 2020. **17**(11): p. 657-674.
68. Mendes, R., et al., *Photothermal enhancement of chemotherapy in breast cancer by visible irradiation of Gold Nanoparticles.* Scientific Reports, 2017. **7**(1): p. 10872.
69. Zhao, Y., et al., *880 nm NIR-triggered organic small molecular-based nanoparticles for photothermal therapy of tumor.* Nanomaterials, 2021. **11**(3): p. 773.
70. Kim, M., J.H. Lee, and J.M. Nam, *Plasmonic photothermal nanoparticles for biomedical applications.* Advanced Science, 2019. **6**(17): p. 1900471.
71. Huang, X., et al., *Plasmonic photothermal therapy (PPTT) using gold nanoparticles.* Lasers in medical science, 2008. **23**: p. 217-228.
72. Sun, Y., et al., *Temperature-sensitive gold nanoparticle-coated pluronic-PLL nanoparticles for drug delivery and chemo-photothermal therapy.* Theranostics, 2017. **7**(18): p. 4424.
73. Ferro-Flores, G., et al., *Theranostic radiopharmaceuticals based on gold nanoparticles labeled with 177Lu and conjugated to peptides.* Current radiopharmaceuticals, 2015. **8**(2): p. 150-159.
74. Castano, A.P., T.N. Demidova, and M.R. Hamblin, *Mechanisms in photodynamic therapy: part one—photosensitizers, photochemistry and cellular localization.* Photodiagnosis and photodynamic therapy, 2004. **1**(4): p. 279-293.

75. Gasco, M.R., *Method for producing solid lipid microspheres having a narrow size distribution*. 1993, Google Patents.
76. Qidwai, A., et al., *Nanostructured lipid carrier in photodynamic therapy for the treatment of basal-cell carcinoma.* Drug delivery, 2016. **23**(4): p. 1476-1485.
77. Kim, D.H., et al., *Gemcitabine-loaded DSPE-PEG-PheoA liposome as a photomediated immune modulator for cholangiocarcinoma treatment.* Biomaterials, 2018. **183**: p. 139-150.
78. Eltahan, A.S., et al., *NVP-BEZ235/Chlorin-e6 co-loaded nanoparticles ablate breast cancer by biochemical and photodynamic synergistic effects.* Nano Research, 2018. **11**: p. 4846-4858.
79. Heo, N.S., et al., *Visible-light-driven dynamic cancer therapy and imaging using graphitic carbon nitride nanoparticles.* Materials Science and Engineering: C, 2018. **90**: p. 531-538.
80. Wieder, M.E., et al., *Intracellular photodynamic therapy with photosensitizer-nanoparticle conjugates: cancer therapy using a 'Trojan horse'.* Photochemical & photobiological sciences, 2006. **5**: p. 727-734.
81. Shen, Z., et al., *Strategies to improve photodynamic therapy efficacy by relieving the tumor hypoxia environment.* NPG Asia Materials, 2021. **13**(1): p. 39.
82. Larue, L., et al., *Using X-rays in photodynamic therapy: an overview.* Photochemical & Photobiological Sciences, 2018. **17**(11): p. 1612-1650.
83. Schaffer, M., et al., *Application of Photofrin II as a specific radiosensitising agent in patients with bladder cancer—a report of two cases.* Photochemical & Photobiological Sciences, 2002. **1**: p. 686-689.
84. Nakamura, T., et al., *A new limb salvage surgery in cases of high-grade soft tissue sarcoma using photodynamic surgery, followed by photo-and radiodynamic therapy with acridine orange.* Journal of surgical oncology, 2008. **97**(6): p. 523-528.
85. Bistolfi, F., *Red radioluminescence and radiochemiluminescence: premises for a photodynamic tumour therapy with X-rays and haematoporphyrin derivatives. A working hypothesis.* Panminerva medica, 2000. **42**(1): p. 69-75.
86. Kamkaew, A., et al., *Scintillating nanoparticles as energy mediators for enhanced photodynamic therapy.* ACS nano, 2016. **10**(4): p. 3918-3935.
87. Ni, K., et al., *Nanoscale metal-organic frameworks for mitochondria-targeted radiotherapy-radiodynamic therapy.* Nature communications, 2018. **9**(1): p. 4321.
88. Guo, N., et al., *Reprogramming of neutrophils as non-canonical antigen presenting cells by radiotherapy–radiodynamic therapy to facilitate immune-mediated tumor regression.* ACS nano, 2021. **15**(11): p. 17515-17527.
89. Zhong, X., et al., *NaCeF4: Gd, Tb scintillator as an X-ray responsive photosensitizer for multimodal imaging-guided synchronous radio/radiodynamic therapy.* Nano letters, 2019. **19**(11): p. 8234-8244.
90. Lu, K., et al., *Low-dose X-ray radiotherapy–radiodynamic therapy via nanoscale metal–organic frameworks enhances checkpoint blockade immunotherapy.* Nature biomedical engineering, 2018. **2**(8): p. 600-610.
91. Ni, K., et al., *Nanoscale metal-organic frameworks enhance radiotherapy to potentiate checkpoint blockade immunotherapy.* Nature communications, 2018. **9**(1): p. 2351.
92. Ni, K., et al., *Nanoscale metal–organic framework co-delivers TLR-7 agonists and anti-CD47 antibodies to modulate macrophages and orchestrate cancer*

immunotherapy. Journal of the American Chemical Society, 2020. **142**(29): p. 12579-12584.
93. Lan, G., et al., *Nanoscale metal–organic layers for deeply penetrating X-ray-induced photodynamic therapy.* Angewandte Chemie, 2017. **129**(40): p. 12270-12274.
94. Zhu, S., et al., *Low-dose X-ray radiodynamic therapy solely based on gold nanoclusters for efficient treatment of deep hypoxic solid tumors combined with enhanced antitumor immune response.* Theranostics, 2023. **13**(3): p. 1042.
95. Peng, Q., et al., *5-Aminolevulinic acid-based photodynamic therapy: principles and experimental research.* Photochemistry and photobiology, 1997. **65**(2): p. 235-251.
96. Zhao, B. and Y.-Y. He, *Recent advances in the prevention and treatment of skin cancer using photodynamic therapy.* Expert review of anticancer therapy, 2010. **10**(11): p. 1797-1809.
97. Ishizuka, M., et al., *Novel development of 5-aminolevurinic acid (ALA) in cancer diagnoses and therapy.* International immunopharmacology, 2011. **11**(3): p. 358-365.
98. Takahashi, J., M. Misawa, and H. Iwahashi, *Combined treatment with X-ray irradiation and 5-aminolevulinic acid elicits better transcriptomic response of cell cycle-related factors than X-ray irradiation alone.* International Journal of Radiation Biology, 2016. **92**(12): p. 774-789.
99. Takahashi, J., et al., *In vivo study of the efficacy and safety of 5-aminolevulinic radiodynamic therapy for glioblastoma fractionated radiotherapy.* International journal of molecular sciences, 2021. **22**(18): p. 9762.
100. Yang, D.-M., et al., *Therapeutic effects of in-vivo radiodynamic therapy (RDT) for lung cancer treatment: a combination of 15MV photons and 5-aminolevulinic acid (5-ALA).* Biomedical physics & engineering express, 2022. **8**(6): p. 065031.
101. Pepper, N.B., et al., *ALA-RDT in GBM: protocol of the phase I/II dose escalation trial of radiodynamic therapy with 5-Aminolevulinic acid in patients with recurrent glioblastoma.* Radiation Oncology, 2024. **19**(1): p. 11.
102. Takahashi, J., et al., *Verification of radiodynamic therapy by medical linear accelerator using a mouse melanoma tumor model.* Scientific reports, 2018. **8**(1): p. 2728.
103. Wang, L.V. and H.-i. Wu, *Biomedical optics: principles and imaging*. 2007: John Wiley & Sons.
104. Grinvald, A., et al., *Functional architecture of cortex revealed by optical imaging of intrinsic signals.* Nature, 1986. **324**(6095): p. 361-364.
105. Repacholi, M.H. and D.A. Benwell, *Essentials of medical ultrasound: A practical introduction to the principles, techniques, and biomedical applications*. 2012: Springer Science & Business Media.
106. Wang, L.V., *Multiscale photoacoustic microscopy and computed tomography.* Nature photonics, 2009. **3**(9): p. 503-509.
107. Wang, X., et al., *Noninvasive laser-induced photoacoustic tomography for structural and functional in vivo imaging of the brain.* Nature biotechnology, 2003. **21**(7): p. 803-806.
108. Lee, S., D. Lee, and C. Kim, *Photoacoustic imaging with carbon nanomaterials.* Carbon nanomaterials for bioimaging, bioanalysis, and therapy, 2019: p. 139-166.
109. Li, P.-C., et al., *Photoacoustic imaging of multiple targets using gold nanorods.* IEEE transactions on ultrasonics, ferroelectrics, and frequency control, 2007. **54**(8): p. 1642-1647.

110. Lyu, Y., J.C. Li, and K. Pu, *Second Near-Infrared Absorbing Agents for Photoacoustic Imaging and Photothermal Therapy.* Small Methods, 2019. **3**(11).
111. Klaue, K., Y. Garmshausen, and S. Hecht, *Taking Photochromism beyond Visible: Direct One-Photon NIR Photoswitches Operating in the Biological Window.* Angewandte Chemie International Edition, 2018. **57**(5): p. 1414-1417.
112. Laufer, J., E. Zhang, and P. Beard, *Evaluation of absorbing chromophores used in tissue phantoms for quantitative photoacoustic spectroscopy and imaging.* IEEE journal of selected topics in quantum electronics, 2010. **16**(3): p. 600-607.
113. Link, S. and M.A. El-Sayed, *Spectral properties and relaxation dynamics of surface plasmon electronic oscillations in gold and silver nanodots and nanorods*. 1999, ACS Publications. p. 8410-8426.
114. Jain, P.K., et al., *Calculated absorption and scattering properties of gold nanoparticles of different size, shape, and composition: applications in biological imaging and biomedicine.* The journal of physical chemistry B, 2006. **110**(14): p. 7238-7248.
115. Lee, K.-S. and M.A. El-Sayed, *Dependence of the enhanced optical scattering efficiency relative to that of absorption for gold metal nanorods on aspect ratio, size, end-cap shape, and medium refractive index.* The Journal of Physical Chemistry B, 2005. **109**(43): p. 20331-20338.
116. Demir, M., et al., *Portfolio of colloidally stable gold–gold sulfide nanoparticles and their use in broad-band photoacoustic imaging.* Nanoscale, 2025.
117. Day, E.S., et al., *Antibody-conjugated gold-gold sulfide nanoparticles as multifunctional agents for imaging and therapy of breast cancer.* International journal of nanomedicine, 2010. **5**: p. 445.
118. Gobin, A.M., et al., *Near-infrared-resonant gold/gold sulfide nanoparticles as a photothermal cancer therapeutic agent.* Small, 2010. **6**(6): p. 745-752.
119. Huang, X.-L., et al., *In vivo toxic studies and biodistribution of near infrared sensitive Au–Au 2 S nanoparticles as potential drug delivery carriers.* Journal of Materials Science: Materials in Medicine, 2008. **19**: p. 2581-2588.
120. Debela, D.T., et al., *New approaches and procedures for cancer treatment: Current perspectives.* SAGE open medicine, 2021. **9**: p. 20503121211034366.
121. Lucky, S.S., K.C. Soo, and Y. Zhang, *Nanoparticles in photodynamic therapy.* Chemical reviews, 2015. **115**(4): p. 1990-2042.
122. Chen, J., et al., *Advances in nanomaterials for photodynamic therapy applications: Status and challenges.* Biomaterials, 2020. **237**: p. 119827.
123. Bechet, D., et al., *Nanoparticles as vehicles for delivery of photodynamic therapy agents.* Trends in biotechnology, 2008. **26**(11): p. 612-621.
124. McFarland, S.A., et al., *Metal-based photosensitizers for photodynamic therapy: the future of multimodal oncology?* Current opinion in chemical biology, 2020. **56**: p. 23-27.
125. Tavakkoli Yaraki, M., B. Liu, and Y.N. Tan, *Emerging strategies in enhancing singlet oxygen generation of nano-photosensitizers toward advanced phototherapy.* Nano-Micro Letters, 2022. **14**(1): p. 123.
126. Abrahamse, H. and M.R. Hamblin, *New photosensitizers for photodynamic therapy.* Biochemical Journal, 2016. **473**(4): p. 347-364.
127. Cui, L., et al., *Radiosensitization by gold nanoparticles: Will they ever make it to the clinic?* Radiotherapy and Oncology, 2017. **124**(3): p. 344-356.
128. Li, J., et al., *Mitochondria-Targeted Nanosystem Enhances Radio–Radiodynamic–Chemodynamic Therapy on Triple Negative Breast Cancer.* ACS Applied Materials & Interfaces, 2023. **15**(18): p. 21941-21952.

129. Shen, S., et al., *Renal-clearable ultrasmall coordination polymer nanodots for chelator-free 64Cu-labeling and imaging-guided enhanced radiotherapy of cancer.* ACS nano, 2017. **11**(9): p. 9103-9111.
130. Chen, X., et al., *X-ray-activated nanosystems for theranostic applications.* Chemical Society Reviews, 2019. **48**(11): p. 3073-3101.
131. Mushtaq, A., et al., *The wonders of X-PDT: an advance route to cancer theranostics.* Journal of Nanobiotechnology, 2024. **22**(1): p. 655.
132. Harada, Y., et al., *5-Aminolevulinic acid-induced protoporphyrin IX fluorescence imaging for tumor detection: Recent advances and challenges.* International journal of molecular sciences, 2022. **23**(12): p. 6478.
133. Malik, Z., *Fundamentals of 5-aminolevulinic acid photodynamic therapy and diagnosis: An overview. Transl Biophoton 2020; 2: e201900022*.
134. Hashemkhani, M., et al., *Cetuximab-Ag 2 S quantum dots for fluorescence imaging and highly effective combination of ALA-based photodynamic/chemo-therapy of colorectal cancer cells.* Nanoscale, 2021. **13**(35): p. 14879-14899.
135. Hashemkhani, M., et al., *ALA/Ag2S/MnO2 Hybrid Nanoparticles for Near-Infrared Image-Guided Long-Wavelength Phototherapy of Breast Cancer.* ACS Biomaterials Science & Engineering, 2023. **9**(7): p. 4126-4137.
136. Onbasli, K., et al., *Aqueous colloidal nanoplatelets for imaging and improved ALA-based photodynamic therapy of prostate cancer cells.* Chemical Communications, 2023. **59**(70): p. 10512-10515.
137. Takahashi, J. and M. Misawa, *Characterization of reactive oxygen species generated by protoporphyrin IX under X-ray irradiation.* Radiation Physics and Chemistry, 2009. **78**(11): p. 889-898.
138. Xiao, Q.Z.G., et al., *Investigation of the Mechanisms of Radio-Dynamic Therapy.* Mathews Journal of Cancer Science, 2020. **5**(1): p. 1-9.
139. Miyake, M., et al., *Dual benefit of supplementary oral 5-aminolevulinic acid to pelvic radiotherapy in a syngenic prostate cancer model.* The Prostate, 2019. **79**(4): p. 340-351.
140. Hasegawa, T., et al., *DNA strand break properties of protoporphyrin IX by X-ray irradiation against melanoma.* International journal of molecular sciences, 2020. **21**(7): p. 2302.
141. Yang, D., et al., *Tumor Regression with 5-Aminolevulinic Acid (5-ALA)-Mediated Radiodynamic Therapy (RDT) Using Different Megavoltage Energies.* International Journal of Radiation Oncology, Biology, Physics, 2023. **117**(2): p. e270.
142. Gong, L., et al., *Application of radiosensitizers in cancer radiotherapy.* International journal of nanomedicine, 2021: p. 1083-1102.
143. Karapetyan, L., et al., *Radiation dose, schedule, and novel systemic targets for radio-immunotherapy combinations.* JNCI: Journal of the National Cancer Institute, 2023. **115**(11): p. 1278-1293.
144. Luo, D., et al., *Targeted gold nanocluster-enhanced radiotherapy of prostate cancer.* Small, 2019. **15**(34): p. 1900968.
145. Wang, Z., et al., *Novel strategies for tumor radiosensitization mediated by multifunctional gold-based nanomaterials.* Biomaterials Science, 2023. **11**(4): p. 1116-1136.
146. Zhu, S., Z. Gu, and Y. Zhao, *Harnessing tumor microenvironment for nanoparticle-mediated radiotherapy.* Advanced Therapeutics, 2018. **1**(5): p. 1800050.

147. Elahi, N., M. Kamali, and M.H. Baghersad, *Recent biomedical applications of gold nanoparticles: A review.* Talanta, 2018. **184**: p. 537-556.
148. Chen, Y., et al., *Albumin-modified gold nanoparticles as novel radiosensitizers for enhancing lung cancer radiotherapy.* International Journal of Nanomedicine, 2023: p. 1949-1964.
149. Yogo, K., et al., *Effect of gold nanoparticle radiosensitization on plasmid DNA damage induced by high-dose-rate brachytherapy.* International Journal of Nanomedicine, 2021: p. 359-370.
150. Fraga, S., et al., *Influence of the surface coating on the cytotoxicity, genotoxicity and uptake of gold nanoparticles in human HepG2 cells.* Journal of Applied Toxicology, 2013. **33**(10): p. 1111-1119.
151. Özçelik, S. and G. Pratx, *Nuclear-targeted gold nanoparticles enhance cancer cell radiosensitization.* Nanotechnology, 2020. **31**(41): p. 415102.
152. Durand, M., et al., *Radiosensitization with gadolinium chelate-coated gold nanoparticles prevents aggressiveness and invasiveness in glioblastoma.* International Journal of Nanomedicine, 2023: p. 243-261.
153. Rahman, W.N., et al., *Enhancement of radiation effects by gold nanoparticles for superficial radiation therapy*, in *Nanomedicine in Cancer*. 2017, Jenny Stanford Publishing. p. 737-752.
154. Liu, Y., et al., *The dependence of radiation enhancement effect on the concentration of gold nanoparticles exposed to low-and high-LET radiations.* Physica Medica, 2015. **31**(3): p. 210-218.
155. Wang, C., et al., *Thioglucose-bound gold nanoparticles increase the radiosensitivity of a triple-negative breast cancer cell line (MDA-MB-231).* Breast cancer, 2015. **22**: p. 413-420.
156. Khoshgard, K., et al., *Radiosensitization effect of folate-conjugated gold nanoparticles on HeLa cancer cells under orthovoltage superficial radiotherapy techniques.* Physics in Medicine & Biology, 2014. **59**(9): p. 2249.
157. Tai, W., Z. Chen, and K. Cheng, *Expression profile and functional activity of peptide transporters in prostate cancer cells.* Molecular pharmaceutics, 2013. **10**(2): p. 477-487.
158. Ebrahimi, S., et al., *Enhancing 5-ALA-PDT efficacy against resistant tumor cells: Strategies and advances.* Life Sciences, 2024: p. 122808.
159. Demirbag-Sarikaya, S., et al., *A novel ATG5 interaction with Ku70 potentiates DNA repair upon genotoxic stress.* Scientific Reports, 2022. **12**(1): p. 8134.
160. Akkoc, Y., et al., *Tumor-derived CTF1 (cardiotrophin 1) is a critical mediator of stroma-assisted and autophagy-dependent breast cancer cell migration, invasion and metastasis.* Autophagy, 2023. **19**(1): p. 306-323.
161. Ma, X., Q. Qu, and Y. Zhao, *Targeted delivery of 5-aminolevulinic acid by multifunctional hollow mesoporous silica nanoparticles for photodynamic skin cancer therapy.* ACS applied materials & interfaces, 2015. **7**(20): p. 10671-10676.
162. Pignatelli, P., et al., *Reactive oxygen species produced by 5-aminolevulinic acid photodynamic therapy in the treatment of cancer.* International Journal of Molecular Sciences, 2023. **24**(10): p. 8964.
163. Donaubauer, A.-J., et al., *Low dose radiation therapy, particularly with 0.5 Gy, improves pain in degenerative joint disease of the fingers: results of a retrospective analysis.* International Journal of Molecular Sciences, 2020. **21**(16): p. 5854.

164. Cerrato, M., et al., *Efficacy of low-dose radiotherapy (2 Gy× 2) in the treatment of marginal zone and mucosa-associated lymphoid tissue lymphomas.* The British Journal of Radiology, 2021. **94**(1123): p. 20210012.
165. Yamamoto, K., et al., *Well-defined poly(methyl methacrylate) grafted to polyethylene with reverse atom transfer radical polymerization initiated by peroxides.* Polymer, 2003. **44**(25): p. 7661-7669.
166. Han, J., et al., *Combining doxorubicin-conjugated polymeric nanoparticles and 5-aminolevulinic acid for enhancing radiotherapy against lung cancer.* Bioconjugate Chemistry, 2022. **33**(4): p. 654-665.
167. Simbulan-Rosenthal, C.M., et al., *Transient poly (ADP-ribosyl) ation of nuclear proteins and role of poly (ADP-ribose) polymerase in the early stages of apoptosis.* Journal of biological chemistry, 1998. **273**(22): p. 13703-13712.
168. Kinner, A., et al., *γ-H2AX in recognition and signaling of DNA double-strand breaks in the context of chromatin.* Nucleic acids research, 2008. **36**(17): p. 5678-5694.
169. Galluzzi, L., et al., *Molecular mechanisms of cell death: recommendations of the Nomenclature Committee on Cell Death 2018.* Cell Death & Differentiation, 2018. **25**(3): p. 486-541.
170. Levine, B., *Autophagy and cancer.* Nature, 2007. **446**(7137): p. 745-747.
171. Klionsky, D.J., et al., *Guidelines for the use and interpretation of assays for monitoring autophagy.* autophagy, 2016. **12**(392): p. 1-222.
172. Johansen, T. and T. Lamark, *Selective autophagy mediated by autophagic adapter proteins.* autophagy, 2011. **7**(3): p. 279-296.
173. Tiwari, P.M., et al., *Functionalized Gold Nanoparticles and Their Biomedical Applications.* Nanomaterials (Basel), 2011. **1**(1): p. 31-63.
174. Nejati, K., et al., *Biomedical applications of functionalized gold nanoparticles: a review.* Journal of Cluster Science, 2021: p. 1-16.
175. Ghosh, S.K. and T. Pal, *Interparticle coupling effect on the surface plasmon resonance of gold nanoparticles: from theory to applications.* Chemical reviews, 2007. **107**(11): p. 4797-4862.
176. Riley, R.S. and E.S. Day, *Gold nanoparticle-mediated photothermal therapy: applications and opportunities for multimodal cancer treatment.* Wiley Interdisciplinary Reviews: Nanomedicine and Nanobiotechnology, 2017. **9**(4): p. e1449.
177. Zhang, Y., et al., *Enhanced radiosensitization by gold nanoparticles with acid-triggered aggregation in cancer radiotherapy.* Advanced Science, 2019. **6**(8): p. 1801806.
178. Ghorbani, F., N. Attaran-Kakhki, and A. Sazgarnia, *The synergistic effect of photodynamic therapy and photothermal therapy in the presence of gold-gold sulfide nanoshells conjugated Indocyanine green on HeLa cells.* Photodiagnosis Photodyn Ther, 2017. **17**: p. 48-55.
179. Li, Y., et al., *Infrared light-absorbing gold/gold sulfide nanoparticles induce cell death in esophageal adenocarcinoma.* Int J Nanomedicine, 2013. **8**: p. 2153-61.
180. Doughty, A.C., et al., *Nanomaterial applications in photothermal therapy for cancer.* Materials, 2019. **12**(5): p. 779.
181. Norouzi, H., K. Khoshgard, and F. Akbarzadeh, *In vitro outlook of gold nanoparticles in photo-thermal therapy: a literature review.* Lasers in medical science, 2018. **33**: p. 917-926.

182. Yang, W., et al., *Gold nanoparticle based photothermal therapy: Development and application for effective cancer treatment.* Sustainable Materials and Technologies, 2019. **22**: p. e00109.
183. Arnold, H., *Basic Clinical Radiobiology*. 2009, CRC Books Boca Raton, FL.
184. Cheng, N.N., et al., *Chemical enhancement by nanomaterials under X-ray irradiation.* Journal of the American Chemical Society, 2012. **134**(4): p. 1950-1953.
185. Sancey, L., et al., *The use of theranostic gadolinium-based nanoprobes to improve radiotherapy efficacy.* The British journal of radiology, 2014. **87**(1041): p. 20140134.
186. Ward, J.F., *DNA damage produced by ionizing radiation in mammalian cells: identities, mechanisms of formation, and reparability.* Progress in nucleic acid research and molecular biology, 1988. **35**: p. 95-125.
187. Neelamraju, P.M., et al., *Potential applications for photoacoustic imaging using functional nanoparticles: A comprehensive overview.* Heliyon, 2024.
188. Jiang, S., J. Lin, and P. Huang, *Nanomaterials for NIR-II Photoacoustic Imaging.* Advanced Healthcare Materials, 2023. **12**(16): p. 2202208.
189. Demir, M., et al., *Portfolio of colloidally stable gold–gold sulfide nanoparticles and their use in broad-band photoacoustic imaging.* Nanoscale, 2025. **17**(3): p. 1371-1380.
190. Sennaroglu, A., et al., *Determination of the wavelength-dependent photothermal conversion efficiency of photosensitizers for photothermal therapy: application to Ag2S-glutathione quantum dots.* The Journal of Physical Chemistry B, 2021. **125**(42): p. 11650-11659.
191. Nambara, K., et al., *Reverse Size Dependences of the Cellular Uptake of Triangular and Spherical Gold Nanoparticles.* Langmuir, 2016. **32**(47): p. 12559-12567.
192. Aioub, M., S.R. Panikkanvalappil, and M.A. El-Sayed, *Platinum-coated gold nanorods: efficient reactive oxygen scavengers that prevent oxidative damage toward healthy, untreated cells during plasmonic photothermal therapy.* ACS nano, 2017. **11**(1): p. 579-586.
193. Belhadj Slimen, I., et al., *Reactive oxygen species, heat stress and oxidative-induced mitochondrial damage. A review.* International journal of hyperthermia, 2014. **30**(7): p. 513-523.
194. Fedyaeva, A., et al., *Heat shock induces production of reactive oxygen species and increases inner mitochondrial membrane potential in winter wheat cells.* Biochemistry (Moscow), 2014. **79**: p. 1202-1210.
195. Minai, L., D. Yeheskely-Hayon, and D. Yelin, *High levels of reactive oxygen species in gold nanoparticle-targeted cancer cells following femtosecond pulse irradiation.* Scientific reports, 2013. **3**(1): p. 2146.
196. Chan, F.K.-M., K. Moriwaki, and M.J. De Rosa, *Detection of necrosis by release of lactate dehydrogenase activity.* Immune Homeostasis: Methods and Protocols, 2013: p. 65-70.
197. Wang, L., et al., *Prostate cancer incidence and mortality: global status and temporal trends in 89 countries from 2000 to 2019.* Frontiers in Public Health, 2022. **10**: p. 811044.
198. Rawla, P., *Epidemiology of prostate cancer.* World journal of oncology, 2019. **10**(2): p. 63.
199. Sun, Z., et al., *Mini Review On: The Roles of DNA Nanomaterials in Phototherapy.* International Journal of Nanomedicine, 2025: p. 2021-2041.

200. Gupta, N. and R. Malviya, *Understanding and advancement in gold nanoparticle targeted photothermal therapy of cancer.* Biochimica et Biophysica Acta (BBA)-Reviews on Cancer, 2021. **1875**(2): p. 188532.
201. Zhao, Y., et al., *Recent advances in combination of copper chalcogenide-based photothermal and reactive oxygen species-related therapies.* ACS Biomaterials Science & Engineering, 2020. **6**(9): p. 4799-4815.
202. Naief, M.F., et al., *A review of the role of carbon nanotubes for cancer treatment based on photothermal and photodynamic therapy techniques.* Journal of Organometallic Chemistry, 2023: p. 122819.
203. Vangijzegem, T., et al., *Superparamagnetic iron oxide nanoparticles (SPION): from fundamentals to state-of-the-art innovative applications for cancer therapy.* Pharmaceutics, 2023. **15**(1): p. 236.
204. Palzer, J., et al., *Iron oxide nanoparticle-based hyperthermia as a treatment option in various gastrointestinal malignancies.* Nanomaterials, 2021. **11**(11): p. 3013.
205. Robertson, C.A., D.H. Evans, and H. Abrahamse, *Photodynamic therapy (PDT): a short review on cellular mechanisms and cancer research applications for PDT.* Journal of Photochemistry and Photobiology B: Biology, 2009. **96**(1): p. 1-8.
206. Casas, A., *Clinical uses of 5-aminolaevulinic acid in photodynamic treatment and photodetection of cancer: A review.* Cancer Letters, 2020. **490**: p. 165-173.
207. Shinoda, Y., et al., *Systematic review and meta-analysis of in vitro anti-human cancer experiments investigating the use of 5-aminolevulinic acid (5-ALA) for photodynamic therapy.* Pharmaceuticals, 2021. **14**(3): p. 229.
208. Xiang, J., et al., *PEPT2-mediated transport of 5-aminolevulinic acid and carnosine in astrocytes.* Brain research, 2006. **1122**(1): p. 18-23.
209. Hagiya, Y., et al., *Expression levels of PEPT1 and ABCG2 play key roles in 5-aminolevulinic acid (ALA)-induced tumor-specific protoporphyrin IX (PpIX) accumulation in bladder cancer.* Photodiagnosis and photodynamic therapy, 2013. **10**(3): p. 288-295.
210. Zhang, C., et al., *Advances in 5-aminoketovaleric acid (5-ALA) nanoparticle delivery system based on cancer photodynamic therapy.* Journal of Drug Delivery Science and Technology, 2022. **78**: p. 103933.
211. Fotinos, N., et al., *5-aminolevulinic acid derivatives in photomedicine: characteristics, application and perspectives.* Photochemistry and photobiology, 2006. **82**(4): p. 994-1015.
212. Bilici, K., et al., *Investigation of the factors affecting the photothermal therapy potential of small iron oxide nanoparticles over the 730–840 nm spectral region.* Photochemical & Photobiological Sciences, 2018. **17**: p. 1787-1793.
213. Scabini, M., et al., *In vivo imaging of early stage apoptosis by measuring real-time caspase-3/7 activation.* Apoptosis, 2011. **16**: p. 198-207.
214. Kupcho, K., et al., *A real-time, bioluminescent annexin V assay for the assessment of apoptosis.* Apoptosis, 2019. **24**: p. 184-197.
215. Gottlieb, E., et al., *Mitochondrial membrane potential regulates matrix configuration and cytochrome c release during apoptosis.* Cell Death & Differentiation, 2003. **10**(6): p. 709-717.
216. Ly, J.D., D.R. Grubb, and A. Lawen, *The mitochondrial membrane potential (Δψ m) in apoptosis; an update.* Apoptosis, 2003. **8**: p. 115-128.